

UNIVERSITY OF CALIFORNIA

Los Angeles

A New Tool for Cold Ion-Molecule Chemistry

A dissertation submitted in partial satisfaction
of the requirements for the degree
Doctor of Philosophy in Physics

by

Gary Chen

2019

© Copyright by

Gary Chen

2019

ABSTRACT OF THE DISSERTATION

A New Tool for Cold Ion-Molecule Chemistry

by

Gary Chen

Doctor of Philosophy in Physics

University of California, Los Angeles, 2019

Professor Wes Campbell, Chair

The dissertation of Gary Chen is approved.

Eric Hudson

Paul Hamilton

James Larkin

Wes Campbell, Committee Chair

University of California, Los Angeles

2019

CONTENTS

List of Figures	viii
Preface	xvii
Curriculum Vitae	xviii
1 Introduction	1
1.1 Interstellar Chemistry	2
1.2 Apparatus Overview	2
2 Chemical Rate Constants	4
2.1 Adiabatic Capture Theory	5
2.1.1 Generalized Rate Constant Derivation	6
2.1.2 Average Dipole Orientation (ADO)	8
3 The Cryogenic Buffer Gas Beam (CBGB)	16
3.1 Design	18
3.1.1 Heat Load and Thermal Conductivity	21
3.1.2 Gas Fill Lines	24
3.2 Beam Density and Extraction	27
3.2.1 Direct Beam Measurement and Parameterization	31
3.2.2 Beam Density at Ion Trap	35
3.3 Beam Velocity	37
3.4 Beam Shuttering	41

4 Trapping and Cooling Ions	45
4.1 Ion Trapping	45
4.2 Vacuum Requirements	48
4.3 ${}^9\text{Be}^+$ Laser Cooling	50
4.4 Imaging System	54
4.5 Determining Excited State Population	56
4.6 Time of Flight Mass Spectrometer (TOF-MS)	60
4.6.1 TOF Signal Integration	63
4.7 Dual Species Loading	64
5 Optical Control of Reactions between Water and Laser-Cooled Be^+ Ions	67
5.1 Prologue	67
5.2 Introduction	67
5.3 Experimental	68
5.4 Results and Discussion	72
5.5 Conclusion	75
6 Isotope-selective chemistry in the $\text{Be}^+({}^2\text{S}_{1/2}) + \text{HOD} \rightarrow \text{BeOD}^+/\text{BeOH}^+$ + H/D reaction	76
6.1 Prologue	76
6.2 Introduction	76
6.3 Experimental	78
6.4 Results and Discussion	79
6.4.1 Conclusion	82
7 Low Temperature $\text{C}^+ + \text{H}_2\text{O}$	83

7.1	Introduction	83
7.2	Experimental	85
7.2.1	Secondary Reactions	85
7.2.2	Internal Relaxation	87
7.2.3	Determination of Branching Ratio	89
7.3	Conclusion	97
8	Conclusion and Future Outlook	99
A	Parker Pulse Valve	100
B	Pressure Calibration	102
C	Chemical Rate Equations	105
C.1	$\text{Be}^+ + \text{H}_2\text{O}$ All Thermochemically Allows Channels	105
C.2	$\text{Be}^+ + \text{H}_2\text{O} + \text{H}_2$	106
C.3	$\text{Be}^+ + \text{H}_2\text{O}/\text{HOD}/\text{D}_2\text{O}$	107
C.4	$\text{C}^+ + \text{H}_2\text{O}$	108
References	109

LIST OF FIGURES

1.1 Diagram of the experimental apparatus combining a CBGB, stem region, differential pumping cross, and ion trap chamber.	3
2.1 An arbitrary effective potential of an monopole-induced-dipole interaction. The maximum of the potential at r_0 creates a centrifugal barrier. Only particles with $E_{\text{col}} > V_{\text{eff}}$ surmount the barrier and collide.	6
2.2 A monopole and a dipole of length $2l$ separated by distance r where the dipole is oriented with angle θ with respect to the internuclear axis. The circumference that the dipole traces at a given angle θ is shown by the dotted circle.	8
2.3 Numerical solutions for equation 2.23 as a function of maximum angle K . As K increases the value of $\bar{\theta}$ decreases but never fully reaches 0 where there would be full dipole-locking.	11
2.4 Numerical solutions to equation 2.24 as a function of the ratio of rotational energy and the monopole-dipole term. As the energy ratio increases, the more $\bar{\theta}_2$ tends towards $\pi/2$	12
2.5 Dipole locking constant C parameterized by the dipole moment μ_D and polarizability α . Figure taken from "Ion-polar molecule collisions: the effect of ion size on ion-polar molecule rate constants; the parameterization of the average-dipole-orientation theory" by Su et al.[47]	14
2.6 A comparison between ADO and Langevin rate constants for $\text{C}^+ + \text{H}_2\text{O}$. A large discrepancy is shown at low temperatures where the ADO rate may be and order of magnitude larger than that of the Langevin model.	15
3.1 Schematic of target species entrainment within a buffer gas beam cell. Introduced target species particles are sympathetically cooled by the buffer gas through elastic collisions where they then may find the exit aperture and produce a beam.	17

3.2	Cross sectional view of CBGB in solidworks. Components include copper sheath for PTR, aluminum radiation shield with chevron baffles, copper shield and experimental cell, and skimmer mounted in stem chamber. The baffles allow for gas to flow into the cold region of the beam apparatus, while preventing 300 K black body radiation from hitting the inner shield and cell.	20
3.3	Cross sectional view of CBGB with side walls removed from the outer vacuum chamber, 40 K aluminum radiation shield, and inner 4 K cryopumping shield exposing the inner experimental cell. A skimmer is mounted in the stem region.	21
3.4	The water fill line, sealed by an ultratorr fitting and heated by nichrome wire. A shut off valve and vernier valve are used to regulate the flow of water into the buffer gas cell.	26
3.5	A kapton film serves as the back wall of the buffer gas cell with a hole punctured for the insertion of the water fill line. The kapton surface seals the back of the cell for a stronger forward beam, while limiting the heat load from a room temperature fill line, and resisting ice formation allowing for continuous and consistent operation with water for over 10 hours.	27
3.6	Theoretically derived buffer gas beam properties of interest given the physical dimensions of our cell in particular: $d_{aperture} = 9 \text{ mm}$. A) γ extraction ratio, dotted red line indicates $\gamma = 1$ where hydrodynamic entrainment begins. B) Number density of buffer gas species within the experimental cell, given an enclosed back wall. The density of target species introduced should stay under 1% of the buffer gas density for other properties to hold. C) Number of collisions a target species particle would expect before extraction out of the cell, the dotted red line indicates 100 collisions before extraction, when rotational degrees of freedom are characteristically thermalized.	31

3.7 Fitted linear behavior of H ₂ O entrained in a Ne buffer gas beam 30 cm from cell aperture. The onset of hydrodynamic entrainment seems to occur around 20 SCCM up through 60/65 SCCM where the H ₂ O extracted into the beam has a clear linear form of $(9.2 \times 10^8 \text{ cm}^{-3}/\text{SCCM})f - 2 \times 10^{10} \text{ cm}^{-3}$	32
3.8 Projected beam densities with a Ne flow rate of 30 SCCM with various distances of interest within the chamber. Beam densities shown are without throttling of the H ₂ O flow valve.	34
3.9 Projected beam densities at the trap center over various nominal Ne flow rates and smallest skimmer aperture size. Beam densities shown are without throttling of the H ₂ O flow valve.	35
3.10 Laser cooled Be ⁺ with P-state fraction $\approx 20\%$, and C ⁺ simultaneously react with H ₂ O introduced from the CBGB, as well as CO introduced from a leak valve. a) A TOF trace of the charged species in the trap after being exposed to H ₂ O from the CBGB for 20 s. b) Integrated TOF traces of relevant species at various delay times.	36
3.11 a) Fitted TOF traces for Be ⁺ + H ₂ O reaction network, experimentally derived H ₂ O beam density is found to be $\rho_{\text{H}_2\text{O}} = (5.4 \pm 0.6) \times 10^6 \text{ 1/cc}$. b) Isolated and fitted C ⁺ + H ₂ O reaction network.	37
3.12 Diagram of entrained neutral Yb interrogation where H ₂ O and Yb are entrained in a buffer gas of neon. The 399 nm laser is scanned over 3 GHz, recording the Yb isotope transitions both transverse, and at a 57.3° angle, to the beam.	40
3.13 Angled longitudinal scan of Yb fluorescence collected by PMT at ≈ 24 cm from cell aperture offset relative to the measured ¹⁷⁴ Yb frequency from a transverse scan. A fit of Gaussians on the observed Yb isotopic transitions is shown with fixed detunings, while shared widths and individual heights are kept free fitting parameters. Fits yield a forward velocity of ≈ 150 m/s and broadened width of 20 K.	41

3.14 Ratios of water and neon from the beam when the Uniblitz shutter is opened and closed. Detection is done via RGA placed 30 cm from the cell aperture.	43
3.15 Fluorescence decays of loaded Be^+ ions exposed to a cold water beam with an inline shutter either opened, in green ($\tau = 7.23 \times 10^{-3}\text{s}$) or closed, in blue ($\tau = 6.37 \times 10^{-2}\text{s}$)	43
3.16 Fluorescence decays of loaded Be^+ ions exposed to a cold water beam with an inline shutter opened, in green ($\tau = 5.37 \times 10^{-2}\text{s}$) or closed, in red ($\tau = 7.59 \times 10^{-3}\text{s}$)	44
4.1 The ion trap inside of the experimental vacuum chamber. An Einzel lens and imaging objective are seen on the vertical axis.	47
4.2 Stability diagram of the experimental ion trap with parameters defined in table 4.1. The trap is set up to be stable for ions of interest, including high mass reaction products, from Be^+ , and C^+ at $m/z = 9$, 12 to CO_2H^+ at $m/z = 45$. . .	48
4.3 Differential pumping region in between the stem and ion trap chambers with gate valves on either end. Blank copper CF gaskets with apertures of 4 mm and 10 mm are placed towards the stem and ion chamber respectively to limit conductance of background gasses while allowing the cryogenic beam through. An Agilent Twistorr 84 FS turbo pump keeps the region at pressures around 10^{-10} Torr and a leak valve allows for controlled introduction of secondary gasses.	50
4.4 Electronic structure of ${}^9\text{Be}^+$ showing the main cooling and repump frequencies (blue) and red detuned recooling beams (orange). The fundamental light from the laser is blue detuned from the ${}^2\text{S}_{1/2}(F=2) \rightarrow {}^2\text{P}_{3/2}$ transition by 400 MHz (middle dashed line), where an AOM driven at 400 MHz brings it back to resonance. Another AOM driven at 400 MHz is double passed to address the ${}^2\text{S}_{1/2}(F=1) \rightarrow {}^2\text{P}_{3/2}$ repump transition. Both beams are then fed through an AOM driven at 200 MHz to produce redetuned recapture beams to cool particularly hot Be^+ ions poorly addressed by the main cooling beams.	52

4.5	Diagram showing the AOM set up to produce the cooling beams, as well as recapture beams shown in Figure 4.4.	53
4.6	The Andor iXon3 camera, enclosed imaging pathway, and objective lens are all mounted onto a 3 axis translation stage. The Sill objective lens is mounted at the end of the imaging tubes, inserted into the reentrant flange. An angled mirror directs the light at a 90° angle up and through a 313 nm bandpass filter placed in front of the camera sensor.	55
4.7	Laser cooled Coulomb crystal of Be ⁺ ions in the LQT imaged with the reentrant imaging system. Dark BeH ⁺ ions are sympathetically cooled in the middle of the top row as well as the third position from the right.	56
4.8	A set of ion images taken at various 313 nm powers run thorough a maximum filter algorithm that identifies local maxima, representing individual ions (circled in red). gaps in the ion chain are due to reactions with background H ₂ producing BeH ⁺ , which occupy crystal sites without fluorescing.	58
4.9	Individual ions identified from images in figure 4.8. Integrated pixel values with subtracted background counts shown for each image, a set's averaged value is shown in brackets.	59
4.10	P-state fraction curve fitted to incident laser power at a fixed detuning of $\delta = \Gamma/2$. Total fluorescence value is normalized by fitted efficiency parameter a to yield ρ_{pp}	60
4.11	Voltages of ion trap rods during ejection into the TOF taken from an oscilloscope. TOF facing front (1 and 3) and back (2 and 4) trap rod pairs shift from the trapping RF operation to HV values after a positive zero voltage crossing. The front pair reaches a nominal 1000 V, while the back pair reaches 1400 V, creating an accelerating potential ΔV , ejecting the trapped ions.	61
4.12	Diagram of the TOF ejection where the ions in the trap are radially accelerated out of the trap with potential ΔV . An Einzel lens ion focusing element focuses the ions onto the MCP at the back of the field free region of length D	62

4.13 Diagram of the single laser, dual ablation set up. The 1064 nm/532 nm YAG pulse is split into two paths via polarizing beam splitter (PBS), and recombined such that they proceed through the same focusing element into the chamber to hit two different targets. Path a) is used for the ablation of graphite to produce C ⁺ , while path b) is independently focused and positioned to ablate beryllium metal to produce Be ⁺ . The ratio of power in each path is adjusted via the half waveplate directly in front of the laser.	65
4.14 TOF trace of simultaneous Be ⁺ and C ⁺ ablation loading averaged over 10 shots. A soft A-ramp is applied after loading, ejecting any unintentionally loaded Cn ⁺ clusters. The C ⁺ peak is narrowed from sympathetic cooling with the laser cooled Be ⁺ ions.	66
5.1 TOF signal (averaged over 10 trials) at reaction time $t = 0$ and 70 s with (A) $P_P = 7\%$ (A) and (B) $P_P = 26\%$. A clear $m/z = 19$ peak emerges when more Be ⁺ ions are excited to $^2P_{3/2}$ state. The BeOH ⁺ / H ₃ O ⁺ ratio for this case ($P_P = 26\%$) is measured to be $\eta(0.26) = 0.039 \pm 0.006$ by integrating both peaks in B when $t = 70$ s.	70
5.2 (A) Typical fluorescence decay measurement. The inset images are a subset of the original ion fluorescence images recorded by the camera. The red curve is an exponential fit (with a free offset) to the data, which gives the total reaction rate. (B) Total reaction rate coefficient as a function of Be ⁺ ($^2P_{3/2}$) state population can be used to separate the contributions from the ground and excited states of Be ⁺	71
5.3 The temporal evolution of Be ⁺ in the trap as a function of reaction time as well as the solutions of differential equations fitted to the kinetics data with $P_P = 26\%$. 71	71

5.4 Energetics of both the ground- and excited-state reaction pathways for the $\text{Be}^+ + \text{H}_2\text{O}$ reaction. Whereas reaction 5.1 proceeds on a single adiabatic PES, the reactions involving excited Be^+ depend on nonadiabatic transitions between different PESs (yellow circles). The submerged well on the ground-state reaction pathway prevents 46% of the trajectories to reflect back to the entrance channel. (Taken from [54])	74
6.1 (A) A typical TOF signal (5 sampe average) at reaction time $t = 0$ s and 60 s with $P_{\text{P}} \approx 2\%$. (B) The temporal evolution of Be^+ , BeOH^+ , and BeOD^+ in the trap as a function of reaction time, as well as the solutions of differential equations fitte to the kinetics data with $P_{\text{P}} \approx 2\%$. (C) The RGA signal (8 traces average) gives relative initial H_2O , HOD, D ₂ O sample ratio, which is $\rho_1 : \rho_2 : \rho_3 = (1.00 \pm 0.02) : (2.45 \pm 0.05) : (1.58 \pm 0.02)$. (D) The product fraction for BeOD^+ production (η) of reactions (6.8 and 6.9) as a function of $\text{Be}^+(^2\text{P}_{3/2})$ state population. The S-state branching ratio is found to be $\eta_s = 0.56 \pm 0.03$, in agreement with the following calculated combined value with different initial H fractions.	80
6.2 (left) Averaged (8 traces) RGA analog scan showing peaks at each isotopologue m/z . Points around the peak of each isotopologue were averaged for a more accurate partial pressure. (right) The branching ratio η of the reaction $\text{Be}^+ + \text{HOD}$ into $\text{BeOD}^+ + \text{H}$ (with a Be^+ P-state fraction of $P_{\text{P}} \approx 2\%$) as a function of initial H fraction in an HOD, H ₂ O, D ₂ O mixture. Shared fitting the branching ratio η with a constant value fit is shown with a weighted average of $\eta = 0.58 \pm 0.14$.	81
7.1 Time evolution of C^+ and H_2O introduced via CBGB as well as subsequent reaction products. a) TOF traces without flooding of CO where fitted rate constants are found to be $k_{7.1} + k_{7.2} = (7.7 \pm 0.6) \times 10^{-9} \text{ cm}^3/\text{s}$, and $k_{7.6} = (1.7 \pm 0.2) \times 10^{-8} \text{ cm}^3/\text{s}$. b) TOF traces with flooding of CO where fitted rate constants are found to be $k_{7.1} + k_{7.2} = (7.9 \pm 0.6) \times 10^{-9} \text{ cm}^3/\text{s}$, and $k_{7.9} = (1.7 \pm 0.2) \times 10^{-8} \text{ cm}^3/\text{s}$.	87
7.2 Average of 10 TOF traces showing reaction products	88

7.3	TOF trace of laser-cooled Be^+ reacting with $\approx 1 \times 10^{-8}$ Torr CO_2 introduced via leak valve for 50 seconds.	90
7.4	Integrated ion signal of individual TOF traces normalized by Be^+ fluorescence at various CO_2 exposure times.	91
7.5	TOF trace of laser-cooled Be^+ and C^+ reacting with $\approx 1 \times 10^{-8}$ Torr CO_2 introduced via leak valve for 40 seconds.	92
7.6	Integrated ion signal of individual TOF traces normalized by total ion signal excluding Be^+ at various CO_2 exposure times.	92
7.7	C^+ and Be^+ loaded into the trap is reacted with H_2O introduced from the beam. The gate valve is closed after 10 seconds and CO_2 is introduced via leak valve so that the HOC^+ is titrated into CO_2H^+	93
7.8	TOF trace of reaction products of Be^+ and C^+ after exposure to both water from the CBGB beam, and CO (10 s) before titration with $^{15}\text{N}_2$ (10 s). There is a distinct lack of N_2H^+ , indicating full conversion of $\text{HOC}^+ \longrightarrow \text{HCO}^+$	96
7.9	a) Average of 10 TOF traces of Be^+ and C^+ exposed to water from the CBGB (10 s), then exposed to $^{15}\text{N}_2$ from the leak valve (10 s) at a density of $1 \times 10^9 \text{ cc}^{-1}$. b) The fraction of the titrated isomers, $\eta \equiv {^{15}\text{N}_2\text{H}^+}/{(^{15}\text{N}_2\text{H}^+ + [\text{HCO}]^+)}$, as a function of $^{15}\text{N}_2$ density. Fitted parameters yield values $C = 0.58 \pm 0.01$, $k_{7.3} = ((6.6 \pm 1.0) \times 10^{-10}) \text{ cm}^3/\text{s}$	97
A.1	Parker Pulse Valve mounted inside the stem chamber aimed at the differential pumping region. The Beam Dynamics skimmer is mounted over the back face of the stem chamber to clean up the supersonic pulse.	101
B.1	Fitted curves for H_2 and H_2O detection between the ion gauge and RGA. The reported pressure between the ion gauge and RGA is nearly identical for H_2O with a slope of 1.1, but noticeably different for H_2 with a slope of 0.59.	103

B.2 (A) A typical fluorescence decay measurement of $\text{Be}^+ + \text{H}_2$. The inset images are a subset of the original ion fluorescence images recorded by the camera. The red curve is an exponential fit (with a free offset) to the data, which gives the total reaction rate. (B) A fit of $\text{Be}^+ + \text{H}_2$ fluorescence decay at various P state excitation fractions. A statistical rate coefficient for full excitation of $(1.2 \pm 0.3_{\text{state}}) \times 10^{-9}$ cm^3/s is in agreement with existing literature. 104

PREFACE

"~~War~~^{The PhD} is a series of catastrophes that results in a victory."^{thesis}

— *Georges Clemenceau*
Gary Chen

CURRICULUM VITAE

- 2009 – 2013 B.S. in Physics, University of Maryland (UMD), College Park, Maryland
- 2013 – Present Ph.D. student in Physics, University of California, Los Angeles (UCLA).

CHAPTER 1

Introduction

This thesis chronicles the experimental work done to realize an apparatus for cold ion-molecule chemistry of species of astrochemical interest, and attempts to understand chemistry in general along the way. The overarching goal of my research has been the understanding of the $\text{HOC}^+:\text{HCO}^+$ branching ratio from the $\text{C}^+ + \text{H}_2\text{O}$ reaction at low temperatures described in Chapter 7.

On our path to understanding of the $\text{C}^+ + \text{H}_2\text{O}$ reaction network, we first examine the reactions of Be^+ with H_2O and HOD . Beryllium cation chemistry is not well understood. We find that promoting the Be^+ from the ground ${}^2\text{S}_{1/2}$ ground state to the ${}^2\text{P}_{3/2}$ excited state opens up new reaction pathways when reacting with H_2O . Although nominally exothermic, $\text{Be}^+({}^2\text{S}_{1/2}) + \text{H}_2\text{O}$ does not proceed as predicted with capture theory. Simulations performed by Hua Guo's group show that a submerged barrier causes dynamics to suppress the rate constant, which is eliminated when promoted to the excited state. Furthermore, we explore bond-selective chemistry by replacing H_2O with HOD to find that despite the large role dynamics played in the rate constant, the H and D bond breaking is consistent with statistical theory.

Learning from the previous experiments, we investigate the $\text{C}^+ + \text{H}_2\text{O}$ reaction and product branching ratios at cryogenic temperatures. Due to the fact that the isomer products have the same charge to mass ratio, a secondary reaction is needed to separate the signals. Great lengths were taken to experimentally verify the secondary reactions that occur while the reaction products are still exposed to the beam, as well as ensure there aren't any long lived internally excited states that would skew the observed branching ratio. Our results

show a deviation from the previously determined ratio found at a reaction temperature of 300 K, in line with the theory provided by Hua Guo.

1.1 Interstellar Chemistry

Chemistry in space

1.2 Apparatus Overview

Cold reactions at collision temperatures are achieved by building an apparatus combining a cryogenic buffer gas beam (CBGB), linear quadrupole ion trap, and time-of-flight mass spectrometer (TOF-MS) seen in Figure 1.1. This apparatus allows us to observe reactions occurring between nearly arbitrary combinations of ions and molecules with collision temperatures ranging from 100 K to 10 K.

The CBGB produces a cold, slow beam by thermalizing the chosen buffer gas (Ne) to thermalize with the walls of a cell cooled by a pulse tube refrigerator (PTR). The buffer gas can then escape from an aperture, creating a beam. Any target species of interest (H_2O) can be introduced into the cell via fill line, ablation, etc. such that collisions with the buffer gas cause sympathetically cooling. At various flow regimes, the target species can also be entrained and brought into the beam, enhancing the signal.

The ion trap uses RF fields to dynamically trap charged particles. The inclusion of laser cooling further localizes the ions in space while also lowering the temperature to the mK regime. In the case where the ion of interest is not easily addressed optically (C^+), we co-trap it with a species that we can laser cool (Be^+). The ions are coupled via the Coulomb interaction and the "dark" ion of interest is sympathetically cooled by the fluorescing ion. These two techniques allow us to produce cold molecules and ions in a species agnostic fashion, whereby the combination of the two allows us to reach collision temperatures around 10 K. As these reactions are occurring, the large trap depth ensure that subsequent charged

reaction products are not lost.

To identify what has been produced, the trap rods are switched such that the ions are ejected radially with a uniform field into a drift tube. The ejected ions separate temporally due to differences in their charge to mass ratio (m/z) and are detected on a microchannel plate detector (MCP) yielding distinctly separated peaks. This allows us to identify what was in the trap after reactions with the ions and neutrals at various exposure times.

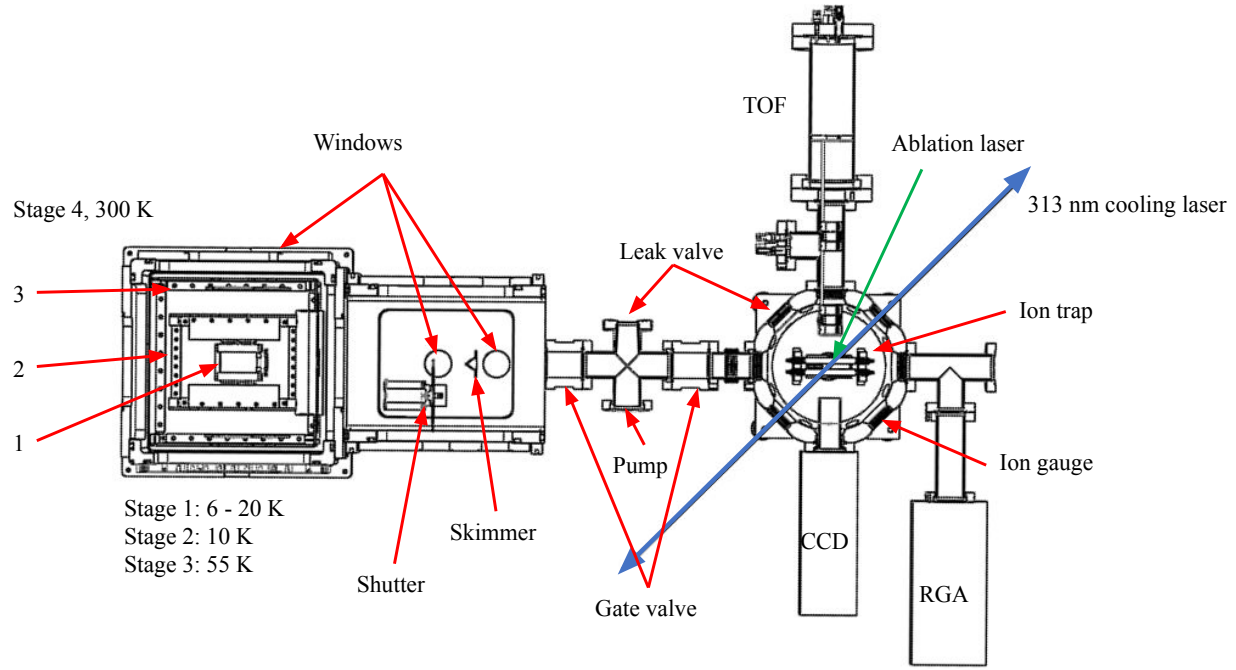


Figure 1.1: Diagram of the experimental apparatus combining a CBGB, stem region, differential pumping cross, and ion trap chamber.

CHAPTER 2

Chemical Rate Constants

When observing chemical reaction rates, it's imperative to find the appropriate model to describe the behavior of the disappearance and appearance of the reactants and products. General models can be found for reactions depending on the unique reactants and their associated stoichiometric coefficients. For example, a typical bimolecular chemical reaction can be written as



where $[A]$ and $[B]$ are the concentrations of the reactants and the lower case values are the respective stoichiometric coefficients. The rate r for this chemical reaction occurring can be represented by the rates of each reactant's disappearance, scaled by their stoichiometric coefficient

$$r = -\frac{1}{a} \frac{d[A]}{dt} = -\frac{1}{b} \frac{d[B]}{dt}. \quad (2.2)$$

In general, a differential equation can be written as

$$r = -k[A]^a[B]^b \quad (2.3)$$

where k is called the rate constant and the "order" of the reaction is the summation of the stoichiometric coefficients $a + b$. If we look at the simplest example where $a = 1$ and $b = 0$, we have a first-order reaction with the differential form and solution:

$$\begin{aligned} \frac{d[A]}{dt} &= -k[A]^a \\ [A] &= [A]_0 e^{-kt} \end{aligned} \quad (2.4)$$

where the subscript 0 denotes the initial concentration of the reactant. We find that the rate constant k has units s^{-1} . If we consider a bimolecular reaction of two different species

where we let $a = b = 1$, the differential form and solution are written as

$$\begin{aligned}\frac{d[A]}{dt} &= -k[A][B] \\ \frac{[A]}{[B]} &= \frac{[A]_0}{[B]_0} e^{([A]_0 - [B]_0)kt}.\end{aligned}\tag{2.5}$$

To measure k , both reactants need to be simultaneously measured, which can add errors and increase the complexity of the experiment. To circumvent this, flooding one reactant such that its total number can be considered constant throughout the reaction process while the scarcer one is depleted can simplify equation 2.5. Letting $[A]$ and $[B]$ be the concentrations of the scarce and flooded reactants respectively, we approximate $[B]_0 \gg [A]_0$ and $[B]_0 \approx [B]$, leading to

$$[A] = [A]_0 e^{-k[B]_0 t}.\tag{2.6}$$

Here, the rate constant k has units of cm^3/s . We can readily see that equation 2.6 is identical in form to equation 2.4. Thus, a reaction of the second-order can then be represented as one of the first-order in what is known as a pseudo-first-order reaction. The reactions discussed in this thesis are exclusively of the pseudo-first-order.

2.1 Adiabatic Capture Theory

Under the understanding that the reactions of interest for this work follow a pseudo-first-order model, a theoretical framework is needed to compare our findings. To figure out the characteristic rate constant k of a reaction, we want to model the interaction between the reactants, whether it be neutral-neutral, to ion-dipole. To do this, we consider adiabatic capture theory, a study of the long range potentials between particles. A caveat is that the adiabatic capture theory is long ranged, only finding the rate at which a collision will occur, not necessarily when a reaction will happen. The probability of a reaction occurring requires modeling of short range interactions within the reaction complex, but understanding capture theory will yield the maximally allowed rate of reactions, if all collisions lead to a reaction.

2.1.1 Generalized Rate Constant Derivation

A general method of calculating the rate constant of two particles with a given potential, finding the collisional cross section, which is then averaged over a velocity distribution to find the rate constant.[57] The interaction potential of two reactants is generally defined as

$$V(r) = \sum_n -\frac{C_n}{r^n} \quad (2.7)$$

where C_n is the interaction coefficient of order n . We may write the effective potential in the center of mass frame as

$$V_{\text{eff}} = \frac{l^2}{2\mu_R r^2} + V(r) \quad (2.8)$$

where $\mu_R = m_1 m_2 / (m_1 + m_2)$ is the reduced mass of the two particles. The competition between the repulsive and attractive terms creates a barrier as seen in Figure 2.1.

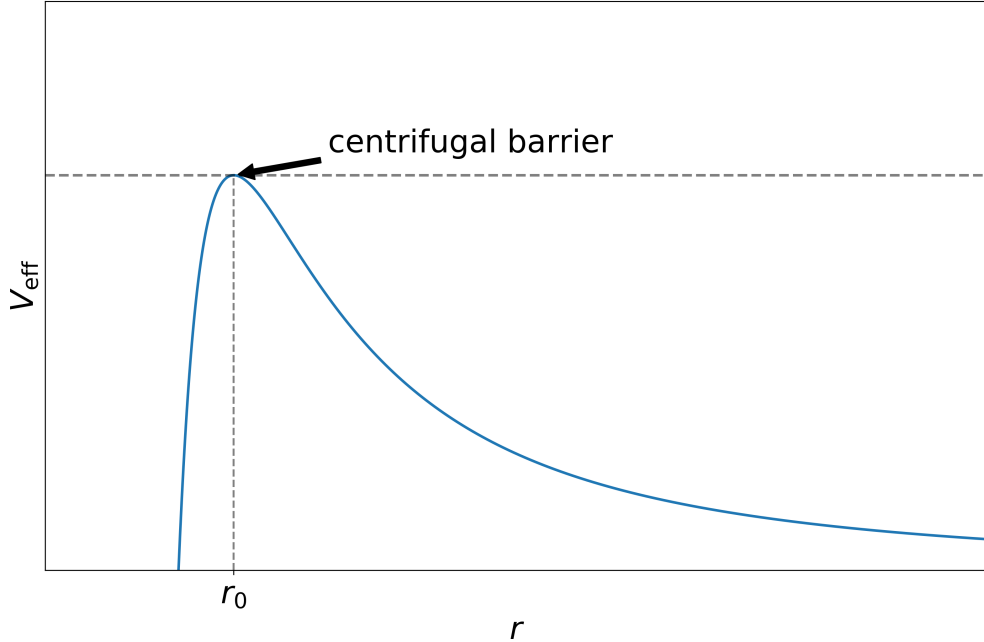


Figure 2.1: An arbitrary effective potential of an monopole-induced-dipole interaction. The maximum of the potential at r_0 creates a centrifugal barrier. Only particles with $E_{\text{col}} > V_{\text{eff}}$ surmount the barrier and collide.

To find the condition for a collision to occur, we first find the position r_0 corresponding

to the maximum of the effective potential, which is the value of the centrifugal barrier.

$$\begin{aligned}\frac{\partial V_{\text{eff}}}{\partial r}\Big|_{r_0} &= 0 \\ \therefore r_0 &= \left(\frac{n\mu_R C_n}{l^2}\right)^{1/n-2}\end{aligned}$$

Substituting r_0 back into equation 2.8, we find the maximal value of the effective potential:

$$V_{\text{eff}}(r_0) = \left(\frac{l^2}{\mu_R}\right)^{\frac{n}{n-2}} \frac{n-2}{2n} (nC_n)^{-\frac{2}{n-2}} \quad (2.9)$$

This then defines the energy necessary for a collision, for if E_{col} exceeds $V_{\text{eff}}(r_0)$, the reactants will be able to surmount the centrifugal barrier and collide. For the condition where $V_{\text{eff}}(r_0) = E_{\text{col}} = \frac{1}{2}\mu_R v^2$, we define the maximum value for the angular momentum l and the impact parameter b .

$$\begin{aligned}l_{\max} &= (\mu_R n)^{1/2} (C_n)^{1/n} \left(\frac{2E_{\text{col}}}{n-2}\right)^{\frac{n-2}{2n}} \\ b_{\max} &= \frac{l_{\max}}{\mu_R v}\end{aligned}$$

We can then define a collision cross section dependent on the collision energy:

$$\begin{aligned}\sigma(E_{\text{col}}) &= \pi b_{\max}^2 \\ &= \frac{\pi}{2} n \left(\frac{2}{n-2}\right)^{\frac{n-2}{2}} \left(\frac{C_n}{E_{\text{col}}}\right)^{\frac{2}{n}}\end{aligned}$$

Integrating the collision cross section with a Maxwell Boltzmann distribution yields a generalized rate constant as a function of temperature and n .

$$k(T) = \int_0^\infty v f(v) \sigma(v) dv \quad (2.10)$$

$$= \sqrt{\frac{2\pi}{\mu_R}} n \left(\frac{2}{n-2}\right)^{\frac{n-2}{2}} C_n^{2/n} (k_B T)^{\frac{n-4}{2n}} \Gamma\left(2 - \frac{2}{n}\right) \quad (2.11)$$

For instance, the monopole-induced-dipole potential of order $n = 4$ has the form and rate constant

$$V_L = -\frac{\alpha q^2}{2r^4} \quad (2.12)$$

$$k(T) = 2\pi q \sqrt{\frac{\alpha}{\mu_R}} \quad (2.13)$$

where α is the polarizability of the neutral reactant, and q is the monopole charge. The corresponding $k(T)$ in equation 2.13 is known as the Langevin rate constant, which is famously temperature independent.

2.1.2 Average Dipole Orientation (ADO)

Unlike the general derivation for adiabatic capture theory outlined in the previous section. We now want to calculate the rate constant for an interaction with more than just an r dependence. The monopole-dipole interaction term is not radially symmetric because the dipole may be oriented at an angle θ with respect to the inter-nuclear axis as shown in Figure 2.2. The potential can be written as

$$V_D(r, \theta) = -\frac{q\mu_D}{r^2} \cos(\theta). \quad (2.14)$$

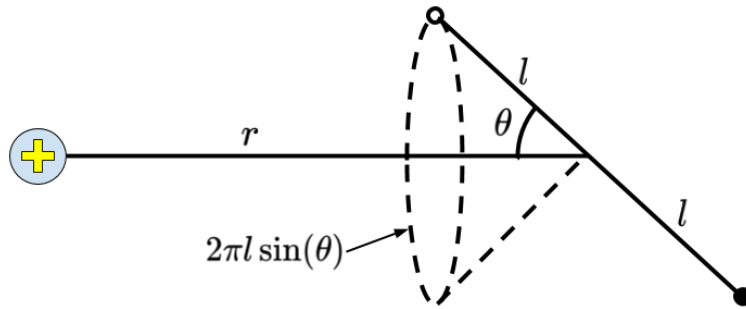


Figure 2.2: A monopole and a dipole of length $2l$ separated by distance r where the dipole is oriented with angle θ with respect to the internuclear axis. The circumference that the dipole traces at a given angle θ is shown by the dotted circle.

The method outlined in section 2.1.1 finds the rate constant by dealing with a two body problem only needing to consider the r degree of freedom. The inclusion of the angle θ in the potential in equation 2.14 complicates this. We could assume that the dipole "locks" onto the monopole and always has an angle $\theta = 0$, but that has been shown to not agree

with experimental results.[47] Instead, it is more appropriate to determine an averaged θ as a function of r . The derivation for the average dipole orientation theory (ADO) pioneered and expanded on by Su and Bowers is used (this process can also be extrapolated to include quadrupole interactions[48]).[46, 47] Considering a monopole and dipole, the interaction potential will include both potential terms 2.12 and 2.14

$$V(r) = -\frac{\alpha q^2}{2r^4} - \frac{q\mu_D}{r^2} \cos(\bar{\theta}(r)) \quad (2.15)$$

where $\bar{\theta}(r)$ is the averaged orientation of the dipole angle as a function of internuclear distance r . This is given by a weighted average

$$\bar{\theta} = \frac{\int \theta P(\theta) d\theta}{\int P(\theta) d\theta} \quad (2.16)$$

where $P(\theta)$ is the probability of finding the dipole oriented with angle θ . It may seem daunting to find the form of $P(\theta)$, but since it is in both numerator and denominator of equation 2.16, only the dependence on θ is needed. In particular, two proportionalities with respect to θ arise.

1. If the dipole is spinning with some angularly dependent angular velocity, $\dot{\theta}(\theta)$, the dipole spends less time in certain orientations. Thus, the probability of finding the dipole in a given orientation is inversely proportional to its angular velocity.

$$P(\theta) \propto 1/\dot{\theta} \quad (2.17)$$

2. At any given angle θ the dipole may trace out a circle with circumference $C = 2\pi l \sin(\theta)$, seen in Figure 2.2. This circumference out is akin to the allowed "phase space" for each angle θ , thus angles with greater "phase space" are more likely to be observed.

$$P(\theta) \propto \sin(\theta) \quad (2.18)$$

Combining the proportionalities of equations 2.17 and 2.18 yields

$$P(\theta) \propto \frac{\sin(\theta)}{\dot{\theta}}. \quad (2.19)$$

We can relate the angular velocity to the angular kinetic energy and the total rotational energy in the system.

$$KE_{rot} = \frac{1}{2}I\dot{\theta}^2$$

$$E_{tot} = KE_{rot} + V_D \quad (2.20)$$

Redefining equation 2.19 with equation 2.20, we find the form

$$P(\theta) \propto \frac{\sin(\theta)}{\sqrt{E_{rot} - V_D}}. \quad (2.21)$$

Combining equations 2.21 and 2.16 yields a fuller form of the averaged dipole angle.

$$\bar{\theta} = \frac{\int \frac{\theta \sin(\theta) d\theta}{\sqrt{E_{rot} + q\mu_D/r^2 \cos(\theta)}}}{\int \frac{\sin(\theta) d\theta}{\sqrt{E_{rot} + q\mu_D/r^2 \cos(\theta)}}} \quad (2.22)$$

We may be tempted to simply integrate over all angles θ , but there are two situations that split the solution into two separate calculations.

1. $E_{rot} = E_1 < \frac{q\mu_D}{r^2}$: There is not enough rotational energy to overcome the dipole locking and is constrained to a maximal angle K . The behavior is oscillatory around the dipole-locking condition, but never fully averages to 0, as shown in Figure 1.

$$E_1 = -\frac{q\mu_D}{r^2} \cos(K)$$

When substituted into equation 2.22, we find:

$$\bar{\theta}_1(r) = \frac{\int_0^K \frac{\theta \sin(\theta) d\theta}{\sqrt{\cos(\theta) - \cos(K)}}}{\int_0^K \frac{\sin(\theta) d\theta}{\sqrt{\cos(\theta) - \cos(K)}}} \quad (2.23)$$

After integration by infinite series,

$$\bar{\theta}_1 = \frac{2\sqrt{2}A}{\sqrt{1 - \cos(K)}}$$

where $A \equiv \int_0^{\pi/2} \frac{a^2 \cos(\phi)^2 d\phi}{\sqrt{1 - a^2 \sin(\phi)^2}}$

$$a \equiv \sin\left(\frac{K}{2}\right).$$

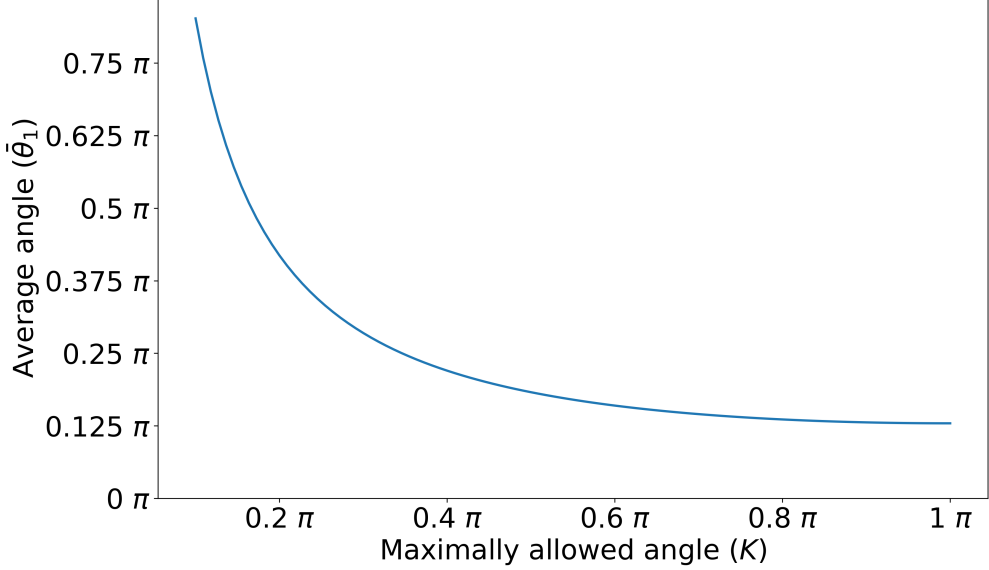


Figure 2.3: Numerical solutions for equation 2.23 as a function of maximum angle K . As K increases the value of $\bar{\theta}$ decreases but never fully reaches 0 where there would be full dipole-locking.

2. $E_{rot} = E_2 > \frac{q\mu_D}{r^2}$: The rotational energy is enough to overcome the dipole locking and θ can swing around in a complete circle. We no longer have bounds on the angles the dipole is allowed over, but the behavior is still dependent on the strength of the internal energy and monopole-dipole interaction.

$$\bar{\theta}_2(r) = \frac{\int_0^\pi \frac{\theta \sin(\theta)d\theta}{\sqrt{E_2 + q\mu_D/r^2 \cos(\theta)}}}{\int_0^\pi \frac{\sin(\theta)d\theta}{\sqrt{E_2 + q\mu_D/r^2 \cos(\theta)}}} \quad (2.24)$$

To gain some intuition on the behavior of $\bar{\theta}_2$, we can rewrite equation 2.24 in the limit that $E_2 \gg \frac{q\mu_D}{r^2}$.

$$\bar{\theta}_2 = \frac{\int_0^\pi \theta \sin(\theta)d\theta}{\int_0^\pi \sin(\theta)d\theta} = \frac{\pi}{2}$$

We see that when the rotational energy is much larger than the interaction potential, we reduce the angular proportionality $P(\theta)$ to just the second proportionality case in equation 2.18. Since the angles are weighted by their respective "phase space", $\theta = \pi/2$ becomes the dominant orientation. This is verified in the plotted numerical solutions to equation 2.24 in Figure 2.4

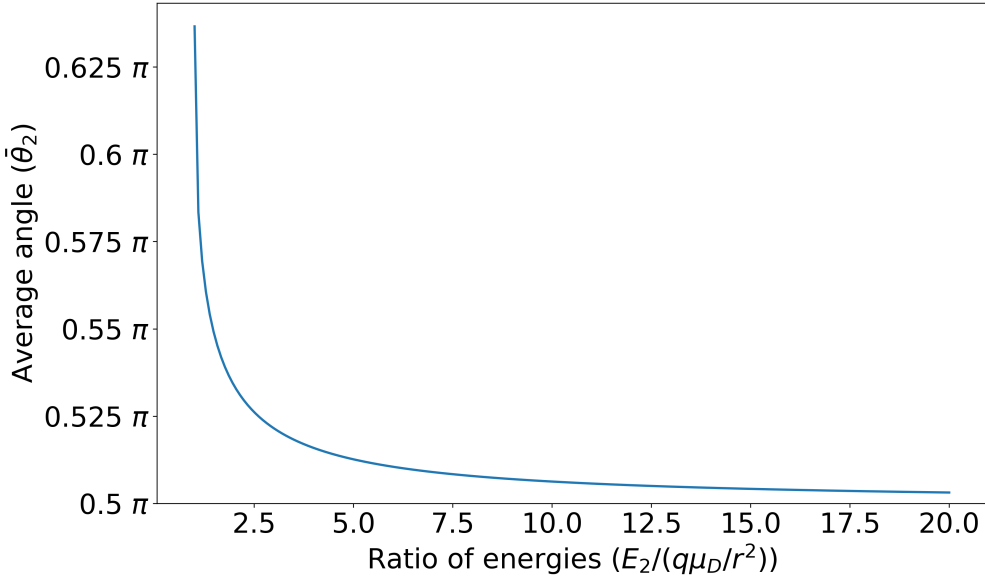


Figure 2.4: Numerical solutions to equation 2.24 as a function of the ratio of rotational energy and the monopole-dipole term. As the energy ratio increases, the more $\bar{\theta}_2$ tends towards $\pi/2$.

Let's say we have the forms for $\bar{\theta}_1(r)$ and $\bar{\theta}_2(r)$, we want to write down the full form of $\bar{\theta}(r)$. We can combine the two weighted by the probability of each as a function of internal energy.

$$\bar{\theta}(r) = \bar{\theta}_1(r)F_1(r) + \bar{\theta}_2(r)F_2(r) \quad (2.25)$$

Where the weightings $F_i(r)$ are related to the Boltzmann distribution of internal states given by

$$P(\epsilon)d\epsilon = \frac{1}{k_B T}e^{-\frac{\epsilon}{k_B T}}d\epsilon.$$

For diatomics, the energies of rotational states is defined as

$$\epsilon = B_e J(J+1)$$

where the rotational constant is $B_e = \hbar^2/(2\mu_R r^2)$, μ_R is the reduced mass of the molecule, and r is the inter-nuclear separation.

To find the rate constant, the same process described in the general adiabatic capture theory derivation can be applied to the interaction potential in equation 2.15). The centrifugal barrier is

$$V_{\text{eff}}(r_0) = \frac{l^2}{2\mu_R r_0^2} - \frac{q^2\alpha}{2r_0^4} - \frac{q\mu_D}{r_0^2} \cos(\bar{\theta}(r_0)).$$

Solving for the situation where $E_{\text{col}} = V_{\text{eff}}$, we find the maximum allowed angular momentum to be

$$l_{\max} = \sqrt{2\mu_D \left(E_{\text{col}} + q\mu_D \cos(\bar{\theta}(r_o)) + \frac{q^2\alpha}{2r_0^2} \right)}$$

where the impact parameter is again defined as $b = l/(\mu_R v)$. In terms of the averaged angle, we can then find an averaged collision cross section of the form

$$\langle \sigma \rangle = \frac{2\mu_R^2}{v^2} \sqrt{E_{\text{col}} + q\mu_D \cos(\bar{\theta}(r_o)) + \frac{q^2\alpha}{2r_0^2}}.$$

We now have all the components necessary to find the rate constant by integrating over a translational velocity distribution

$$k(T) \int_0^\infty v f(v) \langle \sigma(v) \rangle dv.$$

A parameterized form is given in Su et al. where the form is similar to that of just a Langevin term, but now with a dipole interaction term added onto it,[47]

$$k_{ADO} = \frac{2\pi e}{\sqrt{\mu}} \left(\sqrt{\alpha} + C\mu_D \sqrt{\frac{2}{\pi k_B T}} \right) \quad (2.26)$$

where C is the dipole locking constant shown in Figure 2.1.2.[47][49] We can see that the ADO approximation yields a $\sqrt{1/T}$ dependence on the rate constant in contrast to the Langevin treatment. A comparison of the two rate models for $\text{C}^+ + \text{H}_2\text{O}$ is shown in Figure ?? where the difference between the two is seen clearly down at low temperatures.

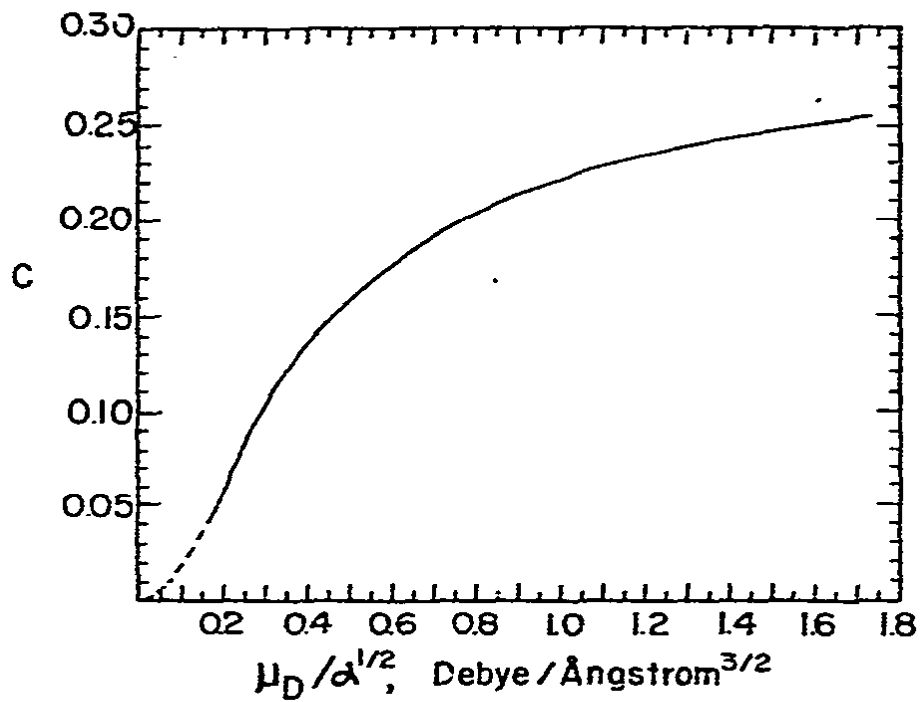


Figure 2.5: Dipole locking constant C parameterized by the dipole moment μ_D and polarizability α . Figure taken from "Ion-polar molecule collisions: the effect of ion size on ion-polar molecule rate constants; the parameterization of the average-dipole-orientation theory" by Su et al.[47]

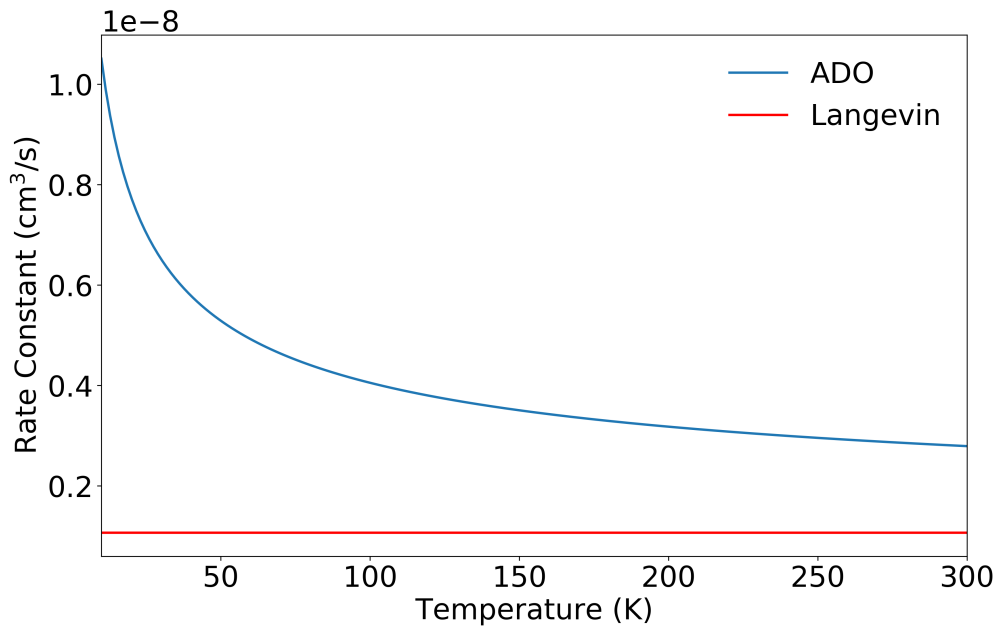


Figure 2.6: A comparison between ADO and Langevin rate constants for $\text{C}^+ + \text{H}_2\text{O}$. A large discrepancy is shown at low temperatures where the ADO rate may be and order of magnitude larger than that of the Langevin model.

CHAPTER 3

The Cryogenic Buffer Gas Beam (CBGB)

To reach reaction temperatures around 10 K from a beam of molecules with trapped ions, a cryogenic buffer gas beam (CBGB) of neon with entrained water is employed. Numerous other methods of creating cold beams of molecules exist, from Zeeman decelerators [31], to Stark decelerators. CBGB's in particular have the benefit of being species agnostic, where the resultant beam properties are not dependent on the target species at hand, rather, the buffer gas species.

By holding a cell filled with a noble gas above its vapor pressure, a volume of gas can be held at cryogenic temperatures. Other species of molecules or atoms may be introduced into the buffer gas cell via ablation, fill line, etc. The target species particles are then sympathetically cooled via collisions with the cold buffer gas. An aperture at one end of the cell allows for the extraction of the buffer gas and entrained target species into a ballistic beam. Holding the buffer gas cell temperature to above 17 K for neon, and 4 K for helium, in high vacuum allows us to accumulate an appreciable stagnation number density within the cell to produce a beam of entrained target particles.

Add
ci-
ta-
tions
for
de-
cel-
er-
a-
tors

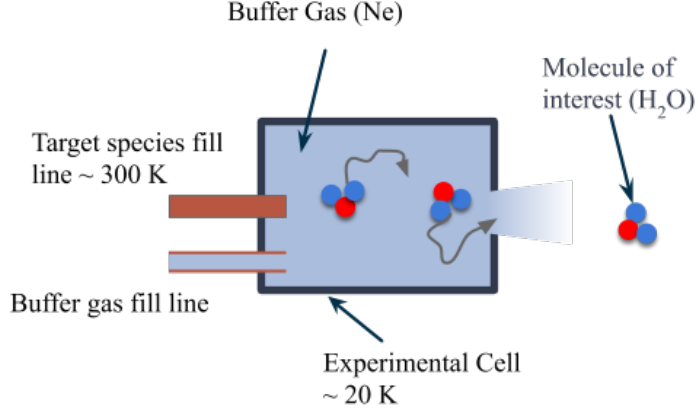


Figure 3.1: Schematic of target species entrainment within a buffer gas beam cell. Introduced target species particles are sympathetically cooled by the buffer gas through elastic collisions where they then may find the exit aperture and produce a beam.

The properties of interest are a function of the flow regime of the beam, which is determined by the choice of gas, its flow rate, and the dimensions of the cell it is held in. It's convenient to use the Reynolds number at the aperture to characterize the flow regime, which can be written as:

$$Re \approx \frac{2d_{aperture}}{\lambda} \approx \frac{8\sqrt{2}\dot{N}\sigma}{d_{aperture}\bar{v}} \quad (3.1)$$

Where $d_{aperture}$ is the diameter of the aperture and λ is the mean free path of the buffer gas particles.[21] When the Reynolds number is low, $Re < 1$, we find that there are on average > 1 collisions at the aperture, meaning the particles escape with little to no interactions with other particles and is called the effusive regime. At high Reynolds numbers, $Re > 100$, in the supersonic regime, there are many collisions and forward velocity boosting as well as internal velocity distribution narrowing occurs. In between, we find the intermediate regime, where we observe the onset of hydrodynamic entrainment of target species with mild forward velocity boosting. In all cases, the gasses inside the cell at thermal equilibrium follow the

Maxwell-Boltzmann distribution.

$$f(v) = \left(\frac{m}{2\pi kT}\right)^{3/2} 4\pi v^2 e^{-\frac{mv^2}{2kT}} \quad (3.2)$$

Where the mean velocity is:

$$\bar{v} = \sqrt{\frac{8k_B T}{\pi m}} \quad (3.3)$$

The goal for our beam is three fold, to produce a slow, dense, and localized beam of our target species that can make it down into the ion trap region. The velocity and density of the target species are both related to the flow regime of the buffer gas, and to reach our goal, it's ideal for us to aim for a beam that operates within the intermediate regime, between effusive and supersonic. Producing a localized beam ensures that we are introducing the minimal unwanted gas load into the ion trap chamber, and that we may quickly and reliably shutter the beam to start and stop the chemical reactions. In the following sections, we will discuss the design of the apparatus and characterization of the beam density, extraction, forward velocity, and shuttering.

3.1 Design

The CBGB apparatus design has various stages, a room temperature 300 K outer aluminum vacuum chamber, onto which a Pulse Tube Refrigerator (PTR) is mounted, an aluminum radiation shield mounted to the 40 K PTR cooling stage, and an inner copper cryopumping shield and experimental cell connected to the 4 K PTR cooling stage. Connected to the vertical vacuum chamber, a "stem" region protrudes out from the beam side as seen in figures figs. 3.2 and 3.3 where a large Agilent Varian-V 551 turbo pump evacuates the entire volume. The beam comes out of the experimental cell and shield, through a set of apertures, into the stem region where skimmers and shutters are mounted to manipulate the beam.

A Cryomech PT415 PTR with a remote head option was attached to the top plate of the vacuum chamber with a large bellows mount to isolate the chamber from the mechanical vibrations caused by the PTR motor head. The chamber was pumped down to normal operating pressures, where then 4 retaining screws were tightened to just above the bel-

low's compressed height. This maintains mechanical decoupling between the outer vacuum chamber and the PTR while running.

We want to minimize the mechanically coupling onto the PTR due to the fragility of the pulse tube walls; small amounts of force applied onto a mechanically connected component would risk torquing the walls to break. Thus, all components inside the CBGB are mechanically connected to the top plate of the vacuum chamber via 8-32 stainless steel (SS316) threaded rods. Thermal connections are made with copper braids welded onto L-shaped brackets that mount between platforms secured to the PTR cooling stages, and the shields.

Not only are all the inner shields connected to the top plate, but so are the feedthroughs including gas fill lines. This ensures that any and all connections made into the CBGB are not disturbed when opening the outer vacuum chamber to expose the inner components.

The design of the shields themselves is informed by the choice of buffer gas species. Commonly used buffer gas species are helium and neon, while helium provides a slower beam, it is more technically challenging to implement. The main technical difference comes from the cryopumping requirements; where neon only needs surfaces to be held at 17 K to continually cryopump, helium requires (coconut) activated charcoal held at 4 K or lower. Aside from the difficulty of getting surfaces to 4 K these volumes of charcoal can become saturated and require purging, limiting one's operating time (few hours). On the other hand, neon ice formed on the 17 K surface will act as a cryopump for more neon gas, allowing for many hours of continuous operation with no appreciable build up of background gas. Our experiment uses neon as a buffer gas for its technical simplicity, the lower achievable temperature with the helium does not yield dramatic gains in the final reaction temperature.

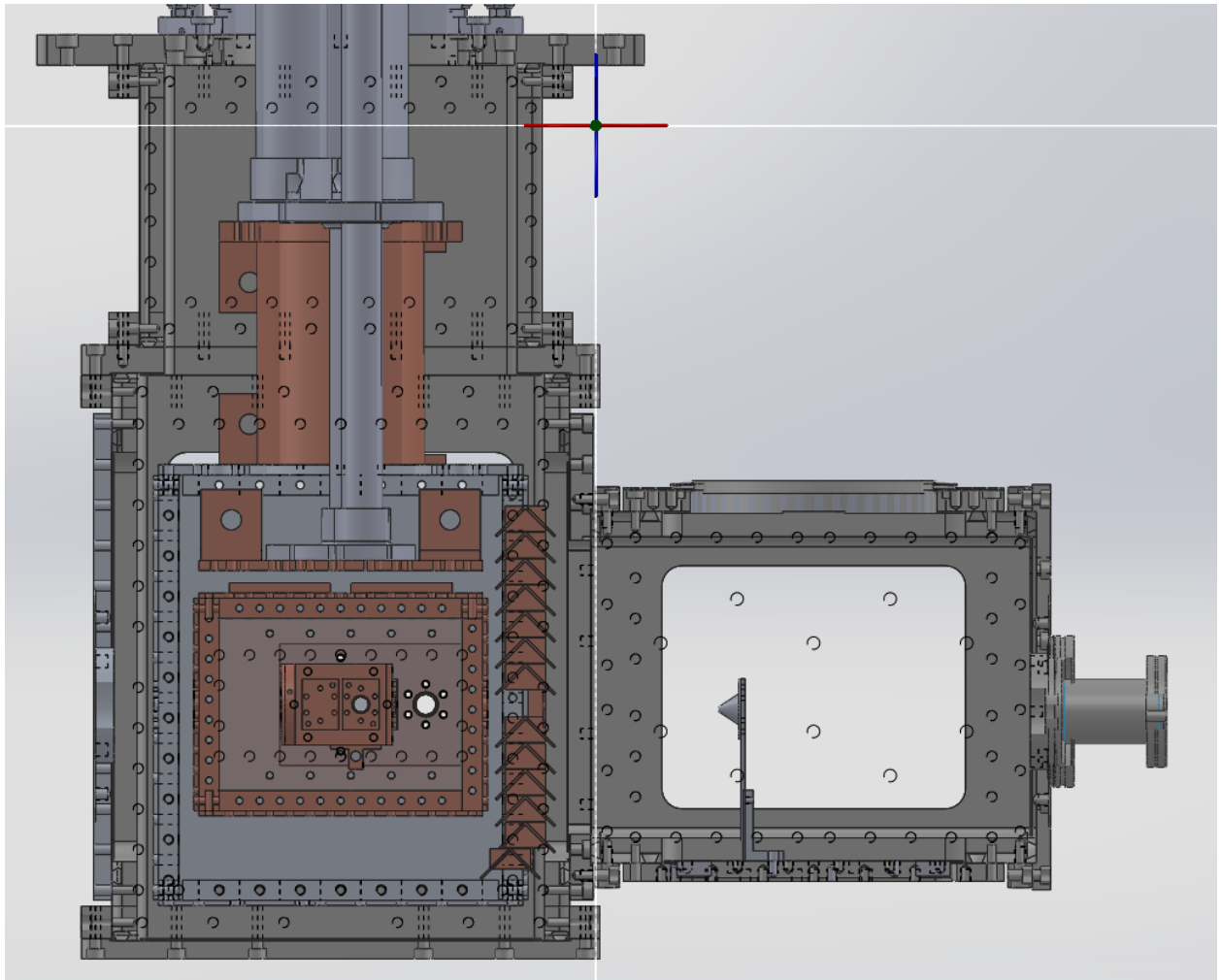


Figure 3.2: Cross sectional view of CBGB in solidworks. Components include copper sheath for PTR, aluminum radiation shield with chevron baffles, copper shield and experimental cell, and skimmer mounted in stem chamber. The baffles allow for gas to flow into the cold region of the beam apparatus, while preventing 300 K black body radiation from hitting the inner shield and cell.

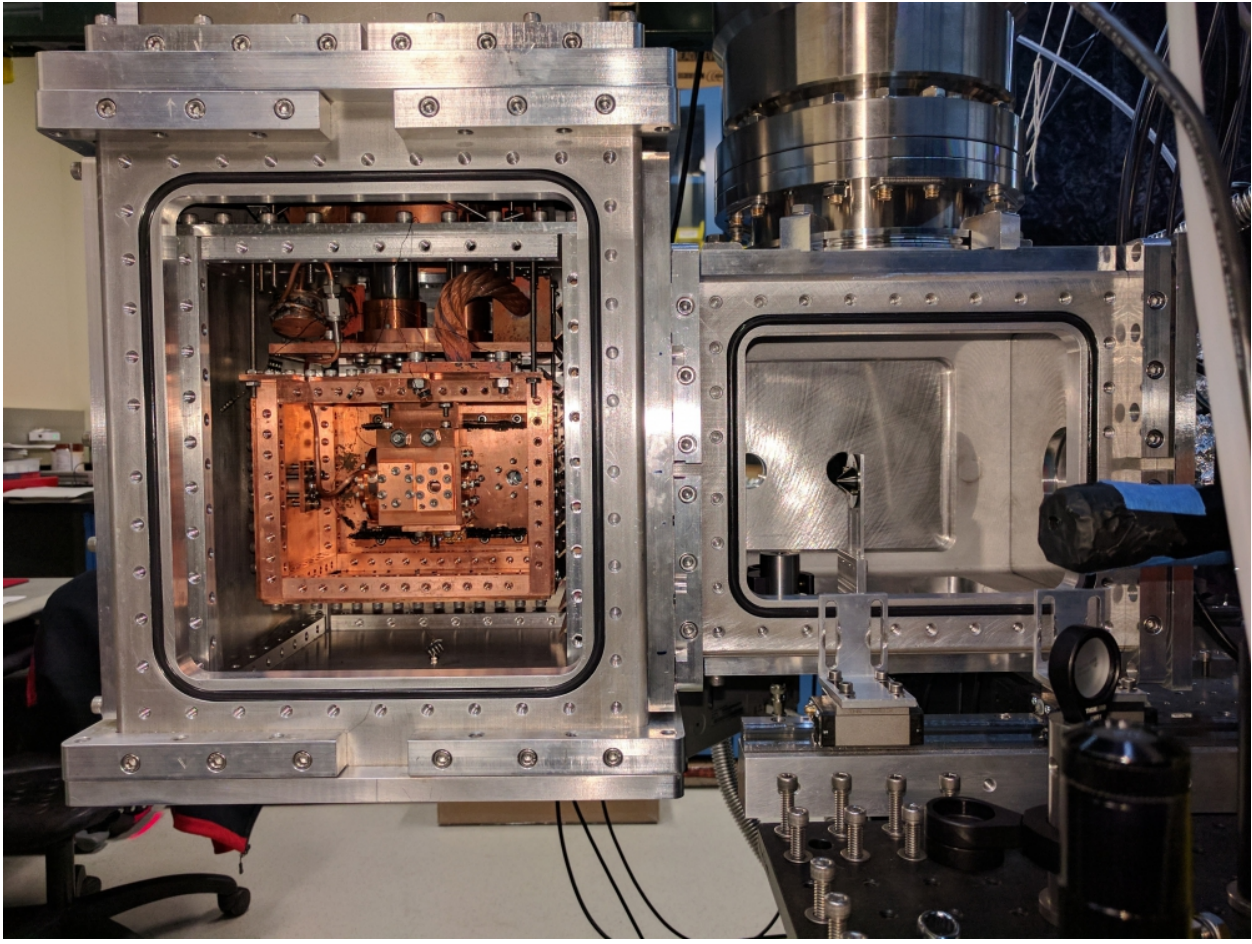


Figure 3.3: Cross sectional view of CBGB with side walls removed from the outer vacuum chamber, 40 K aluminum radiation shield, and inner 4 K cryopumping shield exposing the inner experimental cell. A skimmer is mounted in the stem region.

3.1.1 Heat Load and Thermal Conductivity

To produce a beam of cold particles, various components need to be held within specific temperature ranges to ensure proper operation. Considering neon as the buffer gas species of choice, we maintain the experimental cell at 20 K to prevent the neon from freezing to the walls and maintain a high stagnation density that allows for tuning of the flow regime. Conversely, we need the cryopumping shield surrounding the experimental cell to maintain

a temperature < 17 K so that the neon that escapes the cell is readily captured, as the turbo connected to the stem chamber cannot keep up with the gas load. A lack of proper cryopumping results in high densities in the chamber, which scatters the beam.

The PTR 40 K cooling stage has 40 W of cooling power, while the lowest 4 K stage has only 4 W. The low cooling power of the lowest stage means that extra care is needed to minimize the heat transfer to the stage from the higher temperature regions including black body radiation and conducted heat from high temperature surfaces.

Material choices used in the CBGB are dictated by their thermal conductivity down to the temperature ranges of interest. At room temperature, thermal conductivity (k) of a material is dominated by transfer of energy via phonons through the material. In this regime, different alloys and purities of a material do not greatly affect the conductivity. But once we enter cryogenic temperatures, the conductivity is dominated by electron motion through the material, meaning that purer samples have fewer imperfections to scatter off of, yielding higher conductivities.

Al 6061 was chosen for the radiation shield for its thermal conductivity ($k_{Al6061}(T = 40$ K) = 70 W/(m K)[?]), ease of machining, as well as lightweight properties. The thermal mass of the aluminum shield coupled with its relatively lower thermal conductivity (compared to Cu 10100) means the cool down of this region limits the cool down process to 6 hr until at workable temperatures. The face of the aluminum shield on the outgoing beam side was fitted with a set of stacked chevron baffles as seen in Figure 3.2. The baffle design blocks stray light from entering the radiation shield, while enabling gas to pass from the enclosed shields into the stem region, preventing high density regions from forming and scattering the beam. Conversely, the baffles allow for gas within the stem region to reenter the cryogenic shields and facilitate cryopumping of stray particles.

The copper region contains the experimental cell, enclosed by a copper shield that acts as a cryopumping surface at the appropriate temperatures. At cryogenic temperatures, it's convenient to characterize the conductivity of a copper with the residual resistance ratio ($RRR = \frac{R(T=295 \text{ K})}{R(T=4 \text{ K})}$), where $R(T)$ is the measured resistance at temperature T , which can

be related to the thermal conductivity with the Wiedemann-Franz Law.[?] Cu 10100, or oxygen free copper ($RRR = 2000$), was chosen for these components for its high thermal conductivity from 300 K to 4 K, $k_{Cu10100}(4 \text{ K}) = 10^4 \text{ W}/(\text{m K})$ compared to Cu 11000 ($RRR = 100$), $k_{Cu11000}(4 \text{ K}) = 600 \text{ W}/(\text{m K}).[?]$.

Because it is heat sunk into the same cooling stage as the experimental cell, the copper shield does not act as a radiation shield for it does not redirect the heat load away from the experimental cell's cooling surfaces. For the experimental cell to hold an appreciable vapor pressure while the thermally linked shield acts as a cryopumping surfaces, the two components will need to held at different temperatures. The experimental cell is held at a higher temperature than that of the cryopumping shield with a resistive heater, which is monitored and controlled with a temperature sensor diode (DT-670) and a Lakeshore controller (Model 325). A SS316 ($k_{SS316}(T = 40 \text{ K}) \approx 7 \text{ W}/(\text{m K})$) stand off is used to create a poor thermal bridge between the two regions, allowing for a constant thermal gradient.

The main heat loads onto the system are those from the black body radiation, as well as the stainless steel rods supporting the shields from the top mounting plate. The temperature over the system may be determined by solving the heat/diffusion equation given proper boundary conditions. We use Fourier's Law to approximate the conductive heat loads through individual pieces

$$\dot{Q} = \frac{A}{l}k\Delta T \quad (3.4)$$

Where \dot{Q} is the rate of heat transfer, A is the cross sectional area of the component in question, l is the length of the component, and k is the thermal conductivity of the material. In general, we should be using the integral form where we have a temperature dependent thermal conductivity, $k(T)$, but approximate it to be constant. The main conductive heat loads come from the SS316 rods that mechanically anchor the shield components to the top chamber plate. On the 4 K cryopumping shield, there are 4 such rods, in total, contributing $\approx 60 \text{ mW}$ of power to the 4 K cooling stage.

Aside from the conductive heat load, black body radiation is the main source of heat load onto the cold regions. We describe the power radiated from a source with the Stefan-

Boltzmann law:

$$\dot{Q} = A\epsilon\sigma T^4 \quad (3.5)$$

Where A is the area of the emitting object, ϵ is the emissivity of the surface, and σ is the Stefan-Boltzmann constant. To find the power incident between two surfaces (1, 2) though, we find the form to be:

$$\dot{Q} = \sigma A(T_1^4 - T_2^4) \frac{\epsilon_1 \epsilon_2}{\epsilon_1 + \epsilon_2 - \epsilon_1 \epsilon_2} \quad (3.6)$$
cite
book

In order to characterize the beam inside the CBGB, fused silica windows were mounted onto every shield to allow for optical access. These may pose a problem, as this line of sight allows for radiation coming from room temperature sources to heat up the inner components. The peak wavelength of a black body source at a temperature T is described by Wien's displacement law:

$$\lambda_{max} \approx \frac{2900}{T} \mu\text{m} \quad (3.7)$$

One can see the peak wavelength from a room temperature source is around $93 \mu\text{m}$, which is readily blocked by our fused silica windows. In total, the maximal approximate incident black body power onto the 4 K region, including a 20% fudge factor, is on the order of 200 mW.

3.1.2 Gas Fill Lines

To have a functioning beam, we need to introduce both the buffer gas as well as the target species gas from room temperature without over burdening the cooling stage, or local freezing in the fill lines. The buffer gas fill line is made of thin walled SS316, minimizing the thermal connection between the room temperature mounting and the cold experimental cell. It is thermally anchored to the 40K cooling stage and then brazed onto a plate that mounts to the experimental cell. To avoid local freezing of the buffer gas, the tubing must avoid cryopumping shield as contact. Prior to operating the beam, the non-SS316 tubing outside of the chamber should be disconnected and buffer gas run to flush out any atmospheric gasses that could have migrated into the tubing. Since the tube goes down to cryogenic

temperatures, any trace gasses will freeze and accumulate in the tubing and block the gas flow.

More care must be taken for the design of the water fill line, as it cannot make contact with any mildly cooled metal surface for fear of local freezing. The mating of the fill line to the experimental cell must also prevent excessive heat loads onto the cell while still enclosing the back side to preserve beam flux. With the design help of David Patterson, we utilize a thick walled 1/8" copper tube, with the tip bent at 90°, that enters from the bottom of the CBGB (Figure 3.4), through the shields, into the back of the experimental cell. On the outside, the copper tube enters the CBGB through an Ultratorr fitting welded to an slotted plate that bolts to the bottom of the chamber in a recessed pocket. The combination of an Ultratorr fitting with the sliding plate allows for easy adjustment of the height and insertion depth of the bent end. By slathering the o-ring in the recessed pocket with silicon vacuum grease, the tubing can be adjusted in situ, but the CBGB should be gated off from the rest of the experiment as there is a high risk of letting in atmosphere.

Inside the CBGB, leaving the back of the cell open with a hole eliminated conductive heat transfer between the fill line and the cell, but did not allow for a reliable beam. Ice readily formed on the nearby copper surfaces and slowly closed the back opening, decreasing the effective $A_{aperture}$ of the cell as a function of time, thus changing the flow properties. The back was replaced with a 0.001" film of kapton with a cross cut into the middle for the fill line as seen in figure 3.5. The poor thermal conductivity of kapton (0.5 W/(m K)) ensures minimal conductive heat load to the cell, prevents ice from forming, while also closing the back of the cell. With the kapton, the beam may be run continuously with water entrained in the neon buffer gas for over 10 hours without any change in beam properties. Collisions with buffer gas particles within the cell transferring heat between the fill line and cell walls added < 0.05W of heat load. Solving the integral form of Fourier's Law in cylindrical coordinates results in equation 3.8. With the kapton back, the heat load due to the room temperature water fill line is only 19 mW.

$$\dot{Q} = \frac{2\pi k l (T_1 - T_2)}{\ln(r_2 - r_1)} \quad (3.8)$$



Figure 3.4: The water fill line, sealed by an ultratorr fitting and heated by nichrome wire. A shut off valve and vernier valve are used to regulate the flow of water into the buffer gas cell.

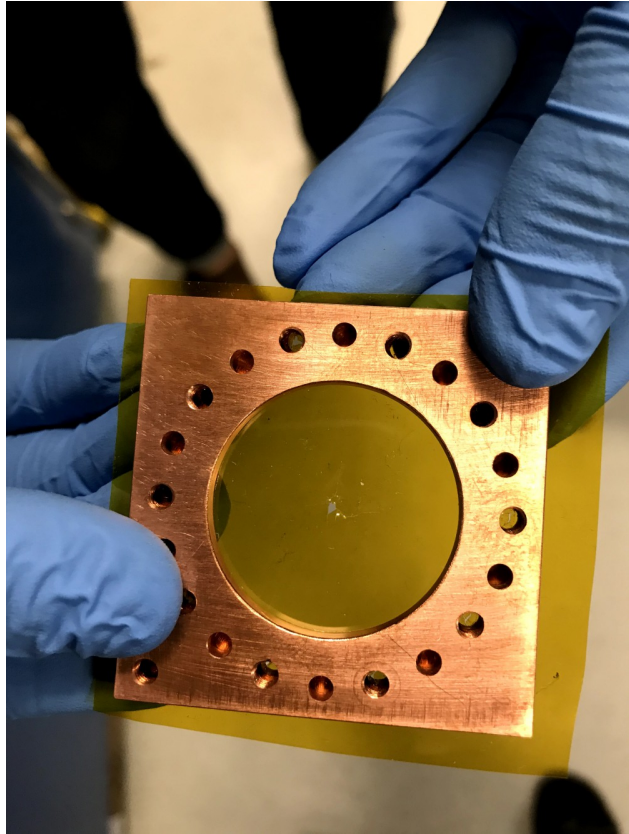


Figure 3.5: A kapton film serves as the back wall of the buffer gas cell with a hole punctured for the insertion of the water fill line. The kapton surface seals the back of the cell for a stronger forward beam, while limiting the heat load from a room temperature fill line, and resisting ice formation allowing for continuous and consistent operation with water for over 10 hours.

3.2 Beam Density and Extraction

We need to have a fairly dense beam of our target species to reach the ion trap center in order to get a reasonable signal to noise of the cold molecule reaction as opposed to the warm background reactions. A dense beam coupled with good cryopumping ensures that the signals seen are primarily, if not solely due to the introduction of the cold beam.

The downstream properties of a beam all start with the buffer gas stagnation density within the experimental cell. The stagnation density is the steady state buffer gas density

that is determined by the physical dimensions of the cell, including the aperture, and the gas throughput, or number flow rate going in. Experimentally, it's preferable to use volumetric flow rates when operating the apparatus, so for calculations, that needs to translate to number flow rate using the ideal gas law:

$$\dot{N} = \frac{Pf}{k_B T}$$

where P is pressure and f is the volumetric flow rate, this translates to about 4×10^{17} particles/s⁻¹ for 1 SCCM of gas flow. By solving for the number density in the flow out of an aperture with molecular flow, we find that the stagnation density within the cell can be shown as:

$$C_{ap} = A \frac{\bar{v}}{4}$$

$$n_b = \frac{4\dot{N}}{A_{aperture}\bar{v}} \quad (3.9)$$

In general, buffer gas beams operate with stagnation densities around $10^{15} - 10^{17}$ cm⁻³. Outside of the cell, we can describe the density of the beam as a function of distance. [33]

$$n(z) = \frac{n_0}{2} \left(1 - \frac{z}{\sqrt{z^2 + a^2}} \right) \quad (3.10)$$

Where z is the distance from the aperture into the vacuum side, n_0 is the initial number density, a is the radius of the aperture. In the far-field, this goes to:

$$n(z) = \frac{n_0 a^2}{4 z^2}$$

But there is something that we must consider, that is that we aren't seeing the full aperture while at all locations, we are actually seeing an appended area due to the inclusion of apertures and skimmers in the way. While only n_0 is only dependent on the aperture size of the cell, $n(z)$ will have a set value defined by the smallest aperture in the beam path. For us, although our cell aperture is ≈ 9 mm in diameter, we have multiple apertures and skimmers in the way, the smallest of which is a skimmer from Beam Dynamics with a diameter of 2 mm.

Sympathetic cooling occurs through collisions between the hot target species being introduced and the cryogenic buffer gas particles. We may consider each hard sphere collision to

transfer heat from the hot target species (T_s) to the cold buffer gas at constant temperature (T_b).

$$\Delta T_s = -\frac{T_s - T_b}{k}$$

Where $k \equiv \frac{(m_b + m_s)^2}{2m_b m_s}$. For the N^{th} collision, we can write the change in temperature:

$$T_s(N) - T_s(N-1) = -\frac{T_s(N-1) - T_b}{k}$$

For large values of N , where the change in temperature becomes small, we can turn the discrete equations into a differential form.

$$\frac{dT_s(N)}{dN} = -\frac{T_s(N) - T_b}{k}$$

Which we can solve with the condition that $T_s(0) = T_0$

$$\begin{aligned} \frac{T_s(N)}{T_b} &= \left(\frac{T_0}{T_b} - 1 \right) e^{-\frac{N}{k}} + 1 \\ &\approx \frac{T_0}{T_b} e^{-\frac{N}{k}} + 1 \end{aligned}$$

Assuming an ablation loading process in which $T_0 = 1 \times 10^4$ K, we find that it still only takes ≈ 12 collisions to thermalize the target species within a factor of 2 of the buffer gas temperature. In general ≈ 100 collisions are needed to relax rotational states to the same range. Vibrational degrees of freedom may take upwards of 10^4 collisions to fully thermalize if the elastic collision energy is much lower than the internal vibrational level.

By finding the mean free path, we can consider the characteristic length the particles travel to be thermalized with the buffer gas, this is then compared to the characteristic length of the cell to determine the effectiveness of the cooling.

$$\lambda = \frac{A_{\text{aperture}} \bar{v}}{4f\sigma \sqrt{m_s/m_b}}$$

If a species is introduced into the buffer gas cell that has a lower vapor pressure than that is allowed at the current temperature, it will be lost when it comes in contact with the cell walls. The rate of this loss can be described as the characteristic time of diffusion of a particle in the buffer gas to the physical dimensions of the cell set the diffusion time constant:

$$\tau_{\text{diff}} = \frac{16}{9\pi} \frac{A_{\text{cell}} n_{0,b} \sigma}{\bar{v}} \quad (3.11)$$

where σ represents the collisional cross section for the buffer gas with the target species. On the other hand, we have the characteristic pump out time given by the conductance of a cell aperture:

$$\tau_{pump} = \frac{4V_{cell}}{\bar{v}A_{aperture}} \quad (3.12)$$

By combining equations eqs. (3.11) and (3.12), we can get a dimensionless ratio, γ that characterizes the extraction fraction out of the cell.

$$\gamma = \frac{\tau_{diff}}{\tau_{pump}} = \frac{\sigma f}{L_{cell}\bar{v}} \quad (3.13)$$

Notice that the γ factor does not depend on aperture size, this is generally true, but increasing the aperture size will lower your number density within the cell, which then influences the characteristic length scale of thermalization. Larger apertures thus run the risk of not allowing your particles to fully thermalize in rotational/vibrational states. But decreasing the aperture size can make alignment as well as controlling the number density more difficult, as finer control over the flow rate is necessary for equivalent flow regimes.

Using equations eqs. (3.13) and (3.9), knowing the physical dimensions of the experimental cell, we find that we may derive theoretical characteristics of the buffer gas beam. During normal operation, our main control over the buffer gas beam is the manipulation of the Ne flow rate, so as a function of buffer gas flow rate (f), we may see how key properties are affected.

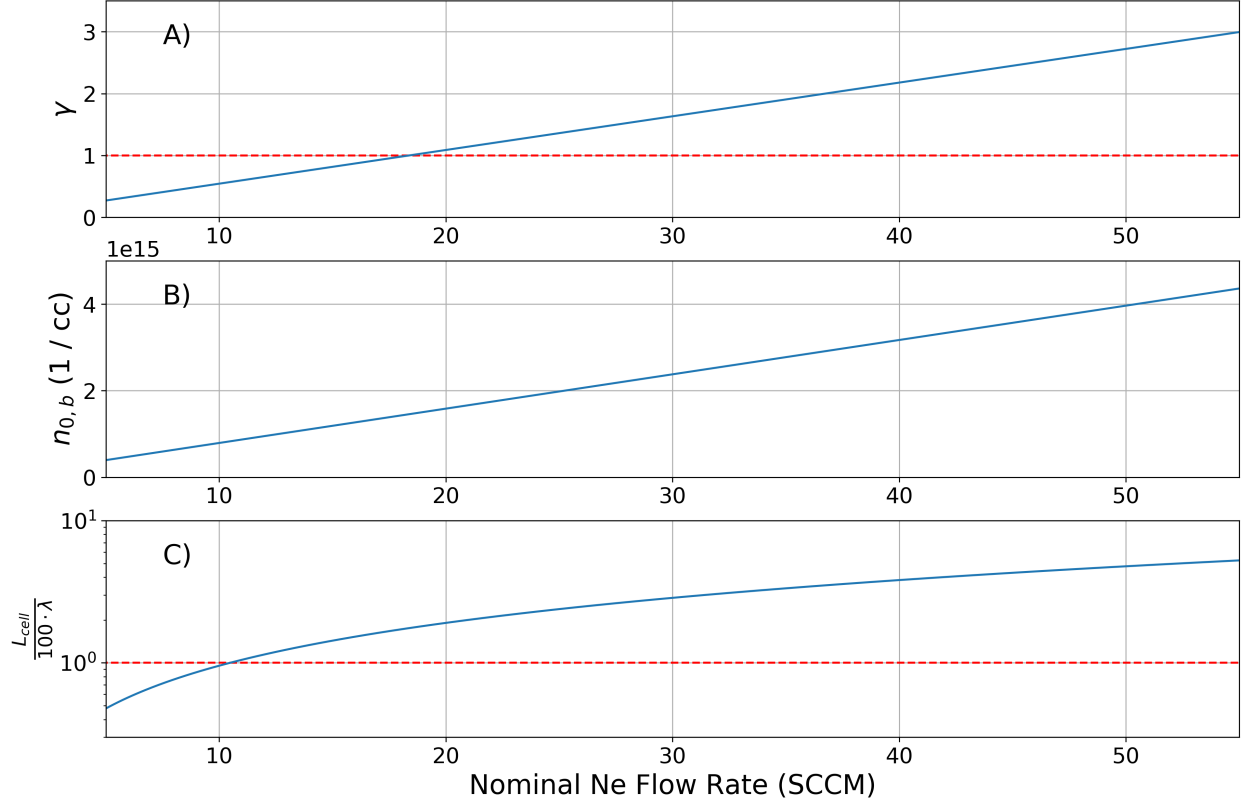


Figure 3.6: Theoretically derived buffer gas beam properties of interest given the physical dimensions of our cell in particular: $d_{aperture} = 9$ mm. A) γ extraction ratio, dotted red line indicates $\gamma = 1$ where hydrodynamic entrainment begins. B) Number density of buffer gas species within the experimental cell, given an enclosed back wall. The density of target species introduced should stay under 1% of the buffer gas density for other properties to hold. C) Number of collisions a target species particle would expect before extraction out of the cell, the dotted red line indicates 100 collisions before extraction, when rotational degrees of freedom are characteristically thermalized.

3.2.1 Direct Beam Measurement and Parameterization

Although we can make statements about the properties of the buffer gas itself in the beam, we are most interested in the properties of the target species introduced into the cell. In

particular, understanding the extraction ratio γ , as well as the velocity, gives us a good handle on the target species characteristics.

To observe the extraction of the target species from the cell, a residual gas analyzer (RGA) is used to determine the density of the beam in the ballistic regime upstream from the ion trap. To ensure the highest possible signal, the Swagelok vernier flow valve used to regulate water vapor flow into the cell is fully opened. During normal operation of the beam in conjunction with the ion trap, the valve is set to a much smaller opening to ensure the properties of the beam are dominated by the buffer gas species, as well as to control the reaction rates.

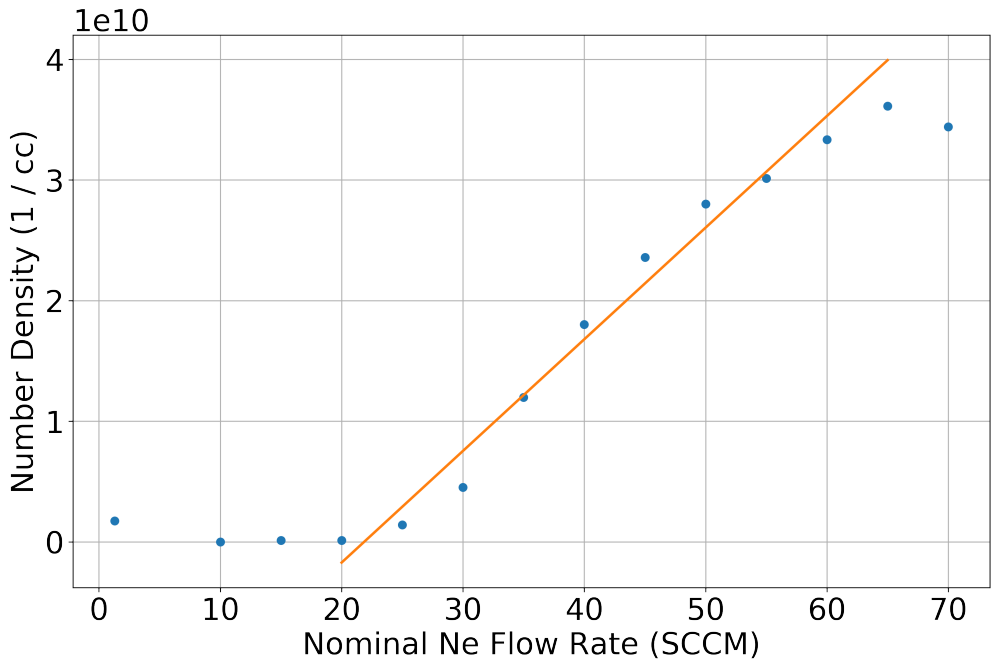


Figure 3.7: Fitted linear behavior of H_2O entrained in a Ne buffer gas beam 30 cm from cell aperture. The onset of hydrodynamic entrainment seems to occur around 20 SCCM up through 60/65 SCCM where the H_2O extracted into the beam has a clear linear form of $(9.2 \times 10^8 \text{ cm}^{-3}/\text{SCCM})f - 2 \times 10^{10} \text{ cm}^{-3}$.

We find that theoretical calculations and experimental results agree that the onset of hydrodynamic entrainment occurs at a buffer gas flow rate of ≈ 20 SCCM. We can combine

the results here with equations 3.3, 3.9, and 3.10 to map out beam densities subject to all other possible parameters we may want to adjust, over our entire experimental apparatus. We start by scaling a combination of equations 3.9 and 3.10 by α , a buffer gas to target species density scaling factor.

$$n(z) = \alpha \frac{f}{A_{aperture} \bar{v}} \left(1 - \frac{z}{\sqrt{z^2 + a^2}} \right)$$

But this only holds true for the region in which the number density is linearly dependent to the buffer gas flow rate, not over all possible ranges; we've seen that the target species only behaves linearly in the hydrodynamic regime. This means that we should be equating the function of $n(z)$ with the linear fit performed on the data for the parameters the data was taken at.

$$mf + b = \alpha \frac{f}{A_{aperture,0} \bar{v}_0} \left(1 - \frac{z_0}{\sqrt{z_0^2 + a_0^2}} \right)$$

Where $z_0 = 30$ cm, being the distance of the RGA from the cell aperture, and $z = 0 = 2$ mm, for the smallest aperture seen during the experimental run. We also define the experimental scaling factors:

$$\begin{aligned} \alpha &= \frac{m}{\beta} + \frac{b}{\beta f} \\ \beta &= \frac{1}{A_{aperture,0} \bar{v}_0} \left(1 - \frac{z_0}{\sqrt{z_0^2 + a_0^2}} \right) \end{aligned}$$

Thus, we obtain a form that includes experimentally derived scaling factors that allows us to project the target species density over the length of the system.

$$n(z) = \frac{mf + b}{A_{aperture} \bar{v} \beta} \left(1 - \frac{z}{\sqrt{z^2 + a^2}} \right) \quad (3.14)$$

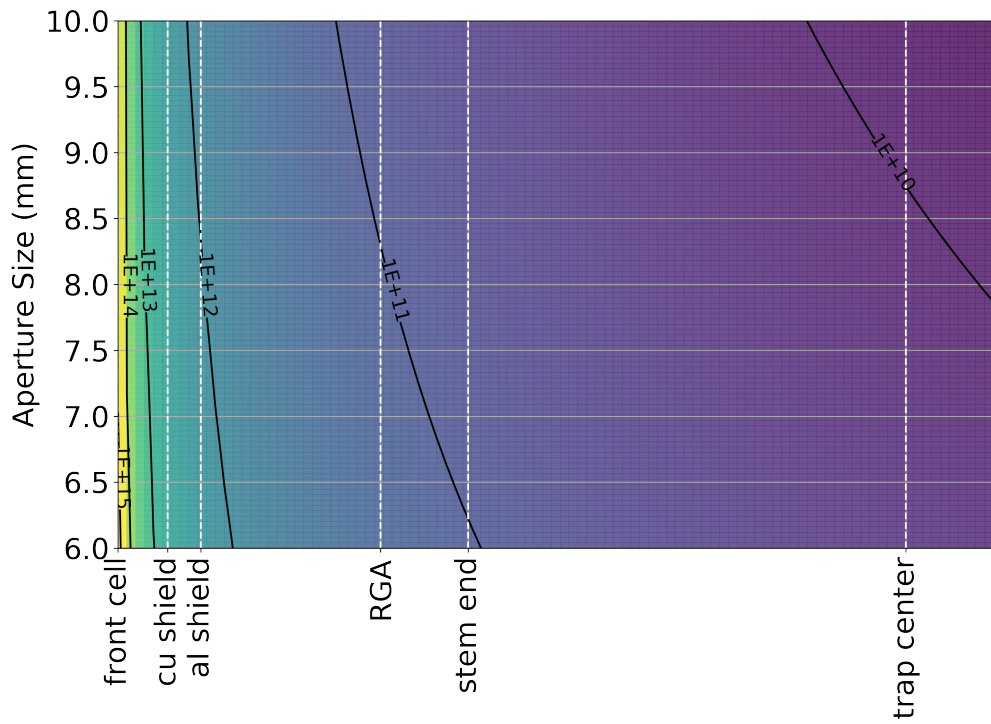


Figure 3.8: Projected beam densities with a Ne flow rate of 30 SCCM with various distances of interest within the chamber. Beam densities shown are without throttling of the H₂O flow valve.

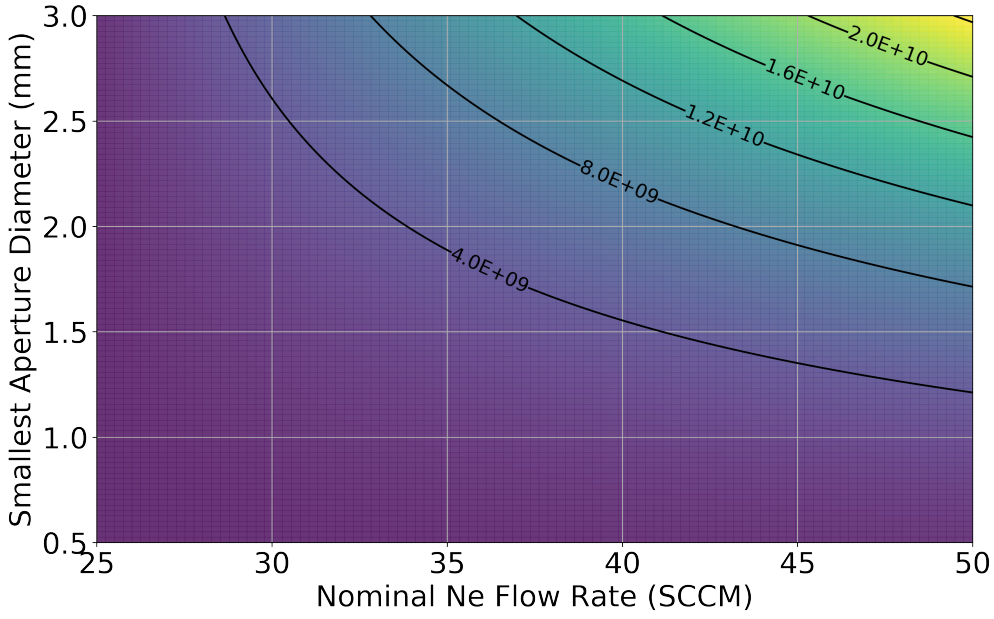


Figure 3.9: Projected beam densities at the trap center over various nominal Ne flow rates and smallest skimmer aperture size. Beam densities shown are without throttling of the H₂O flow valve.

One should not forget the mass dependence in the thermal velocity equation, which leads us to conclude that the choice of the species is a statement of the dominant species in the beam. If we choose to calculate the thermal velocity of the target species found in the beam due to the theoretical thermal velocity of the buffer gas, that indicates that the beam properties are still dominated by the buffer gas species. At target species/buffer gas ratios greater than 1/100, we may start to see the effects of the target species on not only the beam density, but also forward velocity.

3.2.2 Beam Density at Ion Trap

Determining the water density in the beam at the ion trap is more difficult than in the CBGB and stem region. During normal operation of the CBGB, neither the RGA, nor the ion gauge in the trap chamber, which are off the beam axis and in a nipple, are able to detect a change in the background water pressure. With the characterization of the Be⁺ +

H_2O reaction pathways, we were able to validate both experimentally and theoretically, the rate constant and that it follows the ADO model (Section 5). By extending the rate of the $\text{Be}^+ + \text{H}_2\text{O}$ reaction complex to whatever reaction temperature is achieved by the CBGB entrained water (equation 5.10), we may monitor either the fluorescence decay, or the time evolution of the time of flight mass spectrometer (TOF-MS discussed in Section 4.6) peaks to extrapolate a H_2O density. Furthermore, if the peaks of the reaction products of Be^+ and other trapped ions do not overlap, we may determine the beam density for each set of time resolved TOF traces individually.

When probing the reactions of $\text{C}^+ + \text{H}_2\text{O}$ discussed in Section 7, the reaction reaction products of $[\text{HCO}]^+$ and H_3O^+ have $m/z = 29$ and 19, respectively, without conflict with Be^+ or BeOH^+ ($m/z = 26$), the main reaction product of $\text{Be}^+ + \text{H}_2\text{O}$ as seen in Figure 3.10.

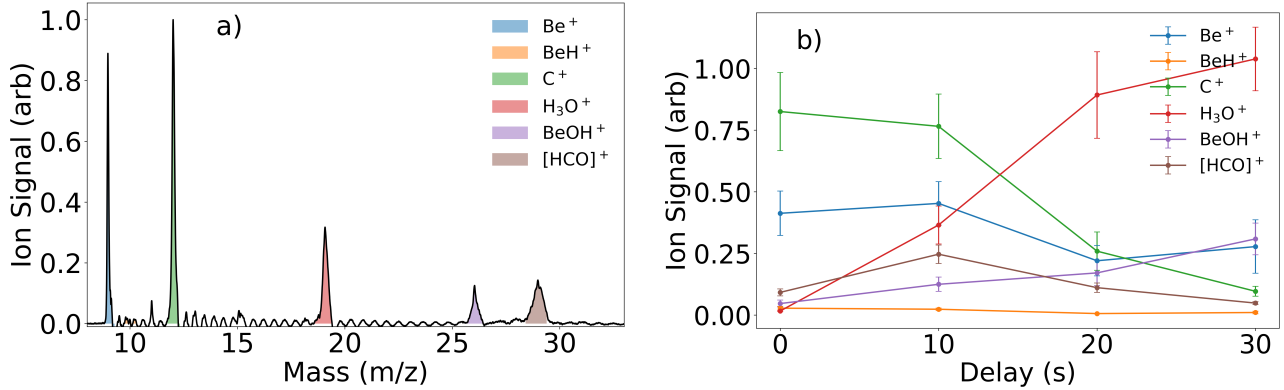


Figure 3.10: Laser cooled Be^+ with P-state fraction $\approx 20\%$, and C^+ simultaneously react with H_2O introduced from the CBGB, as well as CO introduced from a leak valve. a) A TOF trace of the charged species in the trap after being exposed to H_2O from the CBGB for 20 s. b) Integrated TOF traces of relevant species at various delay times.

By isolating only the integrated peaks for the $\text{Be}^+ + \text{H}_2\text{O}$ network of interest, we may use equation 5.10 and differential equations in Section C.2 to find the density of the H_2O beam. We set $\rho_{\text{H}_2} = 0$ and adjust $k_{5.2}$ for the contribution due to reaction 5.3 in the analysis seen in Figure 3.11a). The derived density can then be used to find rate constants for another fitted reaction network, as seen in Figure 3.11b), discussed in further detail in Section 7.

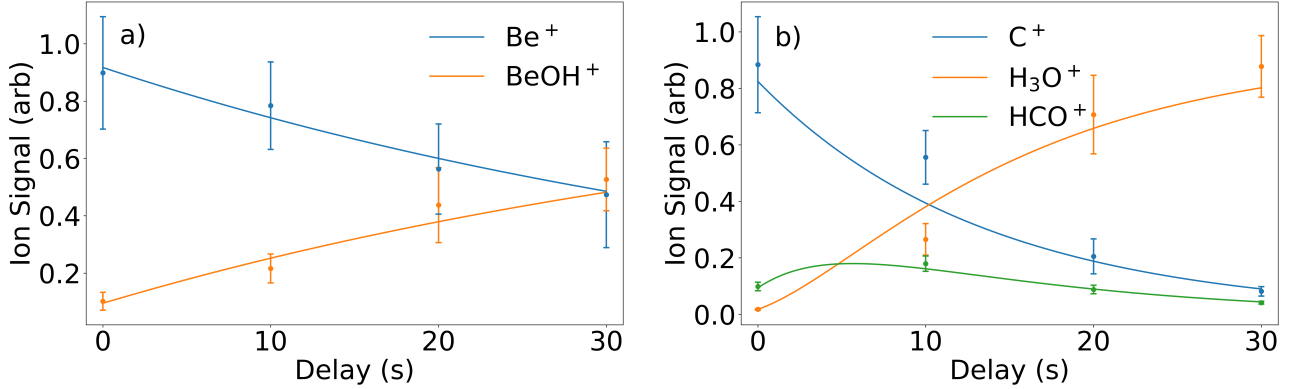


Figure 3.11: a) Fitted TOF traces for $\text{Be}^+ + \text{H}_2\text{O}$ reaction network, experimentally derived H_2O beam density is found to be $\rho_{\text{H}_2\text{O}} = (5.4 \pm 0.6) \times 10^6 \text{ 1/cc}$. b) Isolated and fitted $\text{C}^+ + \text{H}_2\text{O}$ reaction network.

The isolation of reaction networks does not simply reduce the complexity of the shared fitting functions, it is a necessary process. The ablation loading process does not produce the same amount of ions from shot-to-shot, in particular, when considering dual-species loading of Be^+ and C^+ , the ratios will invariably change. The normalization of individual reaction networks is discussed in further detail in Section 4.7.

3.3 Beam Velocity

Over the various flow regimes; effusive, intermediate, and supersonic, the forward velocity and distributions change drastically from 150 m/s up to 800 m/s. We first consider the edge cases of the effusive and supersonic regimes. In the effusive regime, we make the assumption that the particles in the cell are non-interacting. We may rewrite the equation 3.2 as a function of the mean velocity \bar{v} into a simpler form.

$$f(v) = \frac{32}{\pi^2} \frac{v^2}{\bar{v}^3} e^{-4v^2/\pi\bar{v}^2} \quad (3.15)$$

To get the velocity distribution in the beam, we can calculate the distribution of particles incident on an aperture in the cell.

$$\begin{aligned} f_{beam}(v) &= \frac{v}{\bar{v}} f(v) \\ &= \frac{32}{\pi^2} \frac{v^3}{\bar{v}^4} e^{-4v^2/\pi\bar{v}^2} \end{aligned}$$

For low Reynold's numbers ($Re < 1$) the flow at the aperture is purely molecular, which means that there are few to no collisions. This allows us to continue to use the Maxwell-Boltzmann distribution to describe the forward velocity [22].

$$\bar{v}_{\parallel} = \int_0^{\infty} v f(v) dv \approx 1.2\bar{v} \quad (3.16)$$

The spread of the forward velocity of an effusive beam is the full width half max (FWHM) of the Maxwell-Boltzmann distribution: $\Delta\bar{v} \approx 1.5\bar{v}$. As the Reynolds number increases, one can reach the supersonic regime ($Re > 100$) where the forward velocity reaches $1.4\bar{v}$ and the distribution drastically narrows.[22, 33]

The intermediate regime in between the effusive and supersonic regimes is particularly difficult to model, for there are some collisions at the aperture unlike the effusive regime, causing some boosting and narrowing, but not enough to treat the behavior as fully fluid-like. The section 3.2 results show that we can produce a beam in this intermediate regime by demonstrating clear hydrodynamic entrainment.

To better understand the reaction temperatures we will be able to reach, we need a characterization of the beam's velocity, more specifically, the velocity of the target species entrained within the buffer gas. The ideal target species is one with a reliable loading method and can be directly detected in small amounts. Ytterbium metal is known to have good ablation properties and the produced neutral isotopes have well known spectra. By ablating ytterbium foil inside of the experimental cell while the neon gas is being introduced, the ytterbium is cooled by the buffer gas and carried out of the cell. As long as the target species number density is a trace amount in comparison to the bulk buffer gas number density ($\leq 0.1\%$), the flow characteristics are dominated by the buffer gas species [21]. Based upon

the results of our direct RGA measurements of the beam density, we know that the cell parameters used in the previous measurement land us in the intermediate flow regime due to the clear evidence of hydrodynamic entrainment.

To determine the velocity of the beam, we ablate an ytterbium target mounted inside the experimental cell where both neon and water are being introduced. The resulting beam is then illuminated with a 399 nm laser to excite the Yb. The laser is scanned over 3.5 GHz, encompassing all possible Yb isotope transitions. Two scans were taken, one with the 399 nm light perpendicular to the beam path (transverse), and the other where the laser is coming in with an angle of 57.3° shown in Figure 3.12. The resulting spectra are then fitted with summed Gaussian functions with predetermined isotopic shifts taken from literature, giving us the center (¹⁷⁴Yb) frequency, as well as the thermally broadened width of the lines. Between the transverse and angled scans, we find an offset in the spectrum caused by the doppler shift, seen in figure 3.13:

$$\Delta f = \frac{\Delta v}{v} f \cos(\theta) \quad (3.17)$$

Where f is the fundamental center frequency, Δf is the offset observed, v is the forward velocity of the excited ¹⁷⁴Yb, and θ is the angle of the beam with respect to the beam. Using equation 3.17, we find the forward velocity of the beam is around 150 m/s, within the expected range for a hydrodynamically entrained beam. The fitted shared widths give us a beam temperature of 20 K, which is exactly what the experimental cell was held to.

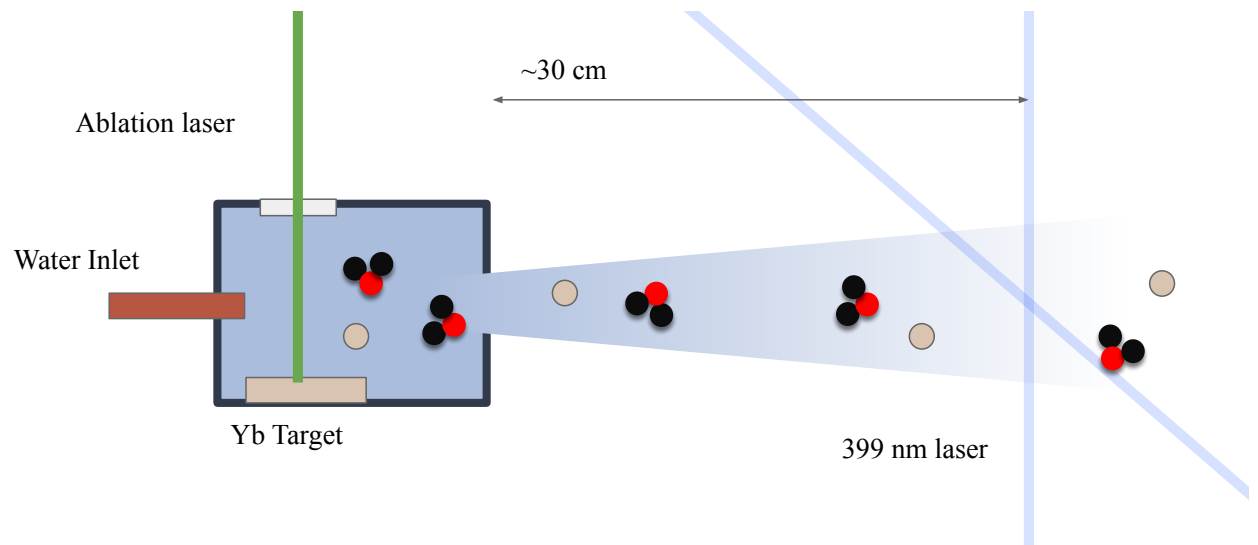


Figure 3.12: Diagram of entrained neutral Yb interrogation where H_2O and Yb are entrained in a buffer gas of neon. The 399 nm laser is scanned over 3 GHz, recording the Yb isotope transitions both transverse, and at a 57.3° angle, to the beam.

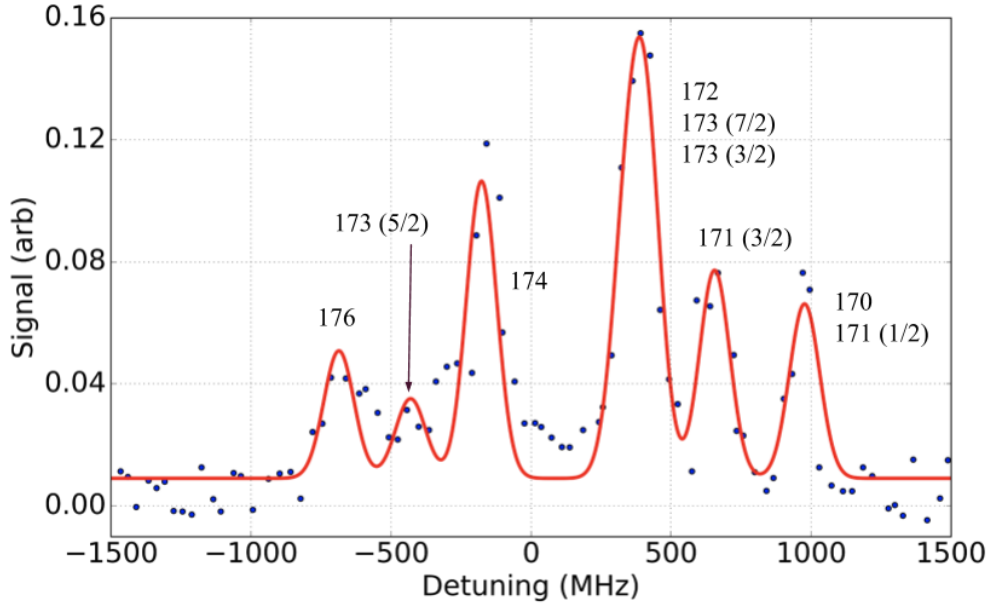


Figure 3.13: Angled longitudinal scan of Yb fluorescence collected by PMT at ≈ 24 cm from cell aperture offset relative to the measured ^{174}Yb frequency from a transverse scan. A fit of Gaussians on the observed Yb isotopic transitions is shown with fixed detunings, while shared widths and individual heights are kept free fitting parameters. Fits yield a forward velocity of ≈ 150 m/s and broadened width of 20 K.

We find that the Yb is entrained within the neon and sympathetically cooled to the cell's temperature. The water that is also introduced in the beam will also be at a similar temperature and forward velocity as long as the neon density is much larger than that of the water when the beam dynamics is dominated by the properties of the buffer gas species.

3.4 Beam Shuttering

With the RGA in the beam path, we were able to open and close a shutter in the beam path and see an extinction of the water signal, but a more accurate representation would be from the ions in the trap themselves. We know that the trapped Be^+ ions will react with H_2O to predominately produce BeOH^+ , which we see as a drop in the fluorescence. Figure 3.16

shows fits of the fluorescence decay as a beam from the CBGB is suddenly blocked by our shutter in the beam line. Comparing the fitted reaction rates, we find that they agree with the background rates found as shown in figure 3.15. This indicates to us that we indeed have a beam of cryogenic water coming from the CBGB, as seen by the sudden extinction of the $\text{Be}^+ + \text{H}_2\text{O}$ reaction.

To accurately control the reactions occurring in the ion trap, it is ideal to be able to quickly turn the beam on and off. Controlling the fill lines outside of the chamber is not ideal, as thin tubing was used, yielding very low conductances. The characteristic time of flow through a tube can be shown to be $\tau_{tube} = CV$, where C is the conductance and V is the volume of the tube in question. Turning on and off the flow outside of the chamber would give time constants in the range of seconds. To more deterministically control the beam flux, we insert a vacuum compatible Uniblitz VS35 35mm Optical Shutter in the beam line. The shutter does not create a seal within the chamber, background gasses may flow around and influence the beam.

Running the beam with the shutter in between the RGA and experimental cell, we find that there is a distinct difference in the H_2O signal when the shutter is open and closed. Using laser cooled Be^+ , we find the difference in the reaction rate both independently, as well as in situ, figs. 3.15 and 3.16.

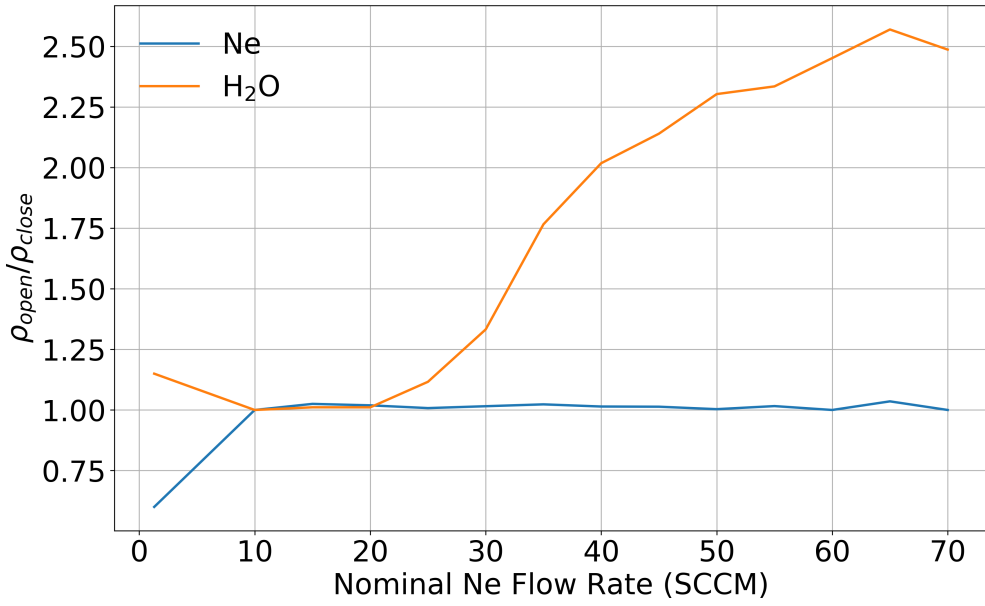


Figure 3.14: Ratios of water and neon from the beam when the Uniblitz shutter is opened and closed. Detection is done via RGA placed 30 cm from the cell aperture.

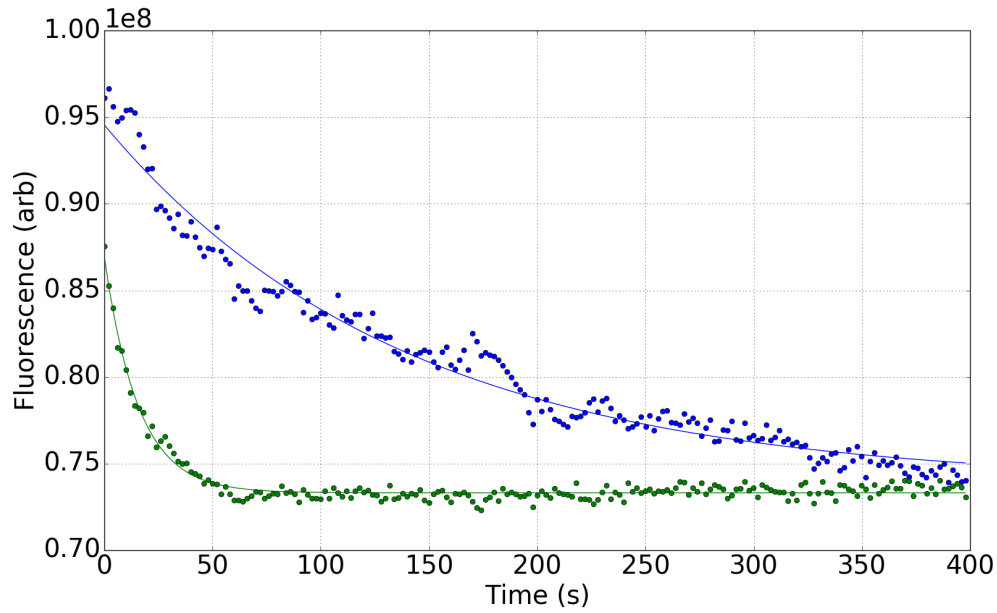


Figure 3.15: Fluorescence decays of loaded Be^+ ions exposed to a cold water beam with an inline shutter either opened, in green ($\tau = 7.23 \times 10^{-3}\text{s}$) or closed, in blue ($\tau = 6.37 \times 10^{-2}\text{s}$)

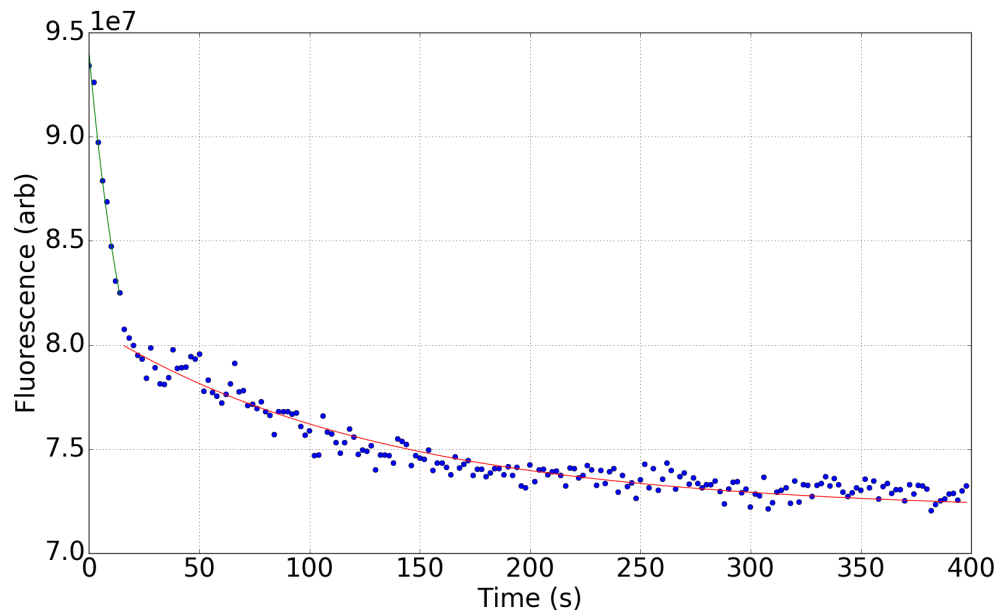


Figure 3.16: Fluorescence decays of loaded Be^+ ions exposed to a cold water beam with an inline shutter opened, in green ($\tau = 5.37 \times 10^{-2}\text{s}$) or closed, in red ($\tau = 7.59 \times 10^{-3}\text{s}$)

CHAPTER 4

Trapping and Cooling Ions

4.1 Ion Trapping

Use RF fields in a linear quadrupole ion trap (LQT) to trap charged particles spatially.[52]

Consider a 3 dimensional potential that could trap a particle, we may assume the form:

$$\Phi = \frac{\Phi}{r_0^2} \sum_{i=1}^3 \alpha_i r_i^2$$

Where r_0 is the distance to the potential surfaces and $r_{1,2,3}$ correspond to x , y , and z respectively. But by Laplace's equation, $\Delta\Phi = 0$, we don't get a confining potential as one of the terms α_i must be negative, leading to a saddle-like potential. To get around this, we may vary the potential in time to create a pseudo-potential that can confine a subset of ions:

$$\Phi_0(t) = V_{DC} + V_{rf} \cos(\Omega_{rf}t)$$

Solving for the equations of motion, we find:

$$\ddot{r}_i + \frac{2\alpha_i e}{mr_0^2} (V_{DC} + V_{AC} \cos(\Omega_{rf}t)) r_0 = 0 \quad (4.1)$$

To solve this, we make changes of variable:

$$a = \frac{8eV_{DC}}{mr_0^2\Omega_{rf}^2} \quad (4.2)$$

$$q = \frac{4eV_{DC}}{mr_0^2\Omega_{rf}^2} \quad (4.3)$$

$$\tau = \frac{1}{2}\Omega_{rf}t$$

To then find the characteristic Mathieu equation:

$$\frac{\partial^2 u}{\partial \tau^2} + (a - 2q \cos(2\tau))u = 0 \quad (4.4)$$

A diagram showing stable solutions to equation 4.4 with the experimental trap values is shown in figure 4.2. To provide full 3 dimensional trapping, DC end cap voltages of around 200 V are applied to contain the ions axially.

Considering our linear quadrupole trap, where we have radial symmetry, the conditions for the x and y orientations are the same, where $a_x = a_y = -\frac{1}{2}a_z$ as well as $q_x = q_y = -\frac{1}{2}q_z$. As long as we are in a regime where $a \ll q^2 \ll 1$, we can approximate the pseudo-potential as a harmonic oscillator where multiples of the secular frequency are the allowed modes.

$$\omega_i = \gamma_i \frac{\Omega_{rf}}{2} \quad (4.5)$$

Where $\gamma_i = \sqrt{a_i + \frac{q_i^2}{2}}$. Inside this harmonic potential, the ions may move around up until the point at which they would hit the trap rods. Keeping with the harmonic potential approximation, we can characterize the maximum energy an ion may have in the trap to be when the energy of the ion at the condition where it would be displaced far enough to hit a rod.

$$E_0 = \frac{m}{2e} \omega_{sec}^2 r_0^2 \quad (4.6)$$

Compiling the relevant trap parameters and using equations eqs. (4.5) and (4.6):

Parameter	Value
r_0	6.85 mm
Ω_{rf}	$(2\pi)3$ MHz
V_{DC}	2 V
V_{rf}	200 V
ω_{sec}	83 kHz
$E_0(m/z = 9)$	7 eV

Table 4.1: Experimental trap parameters predominantly used in this thesis.

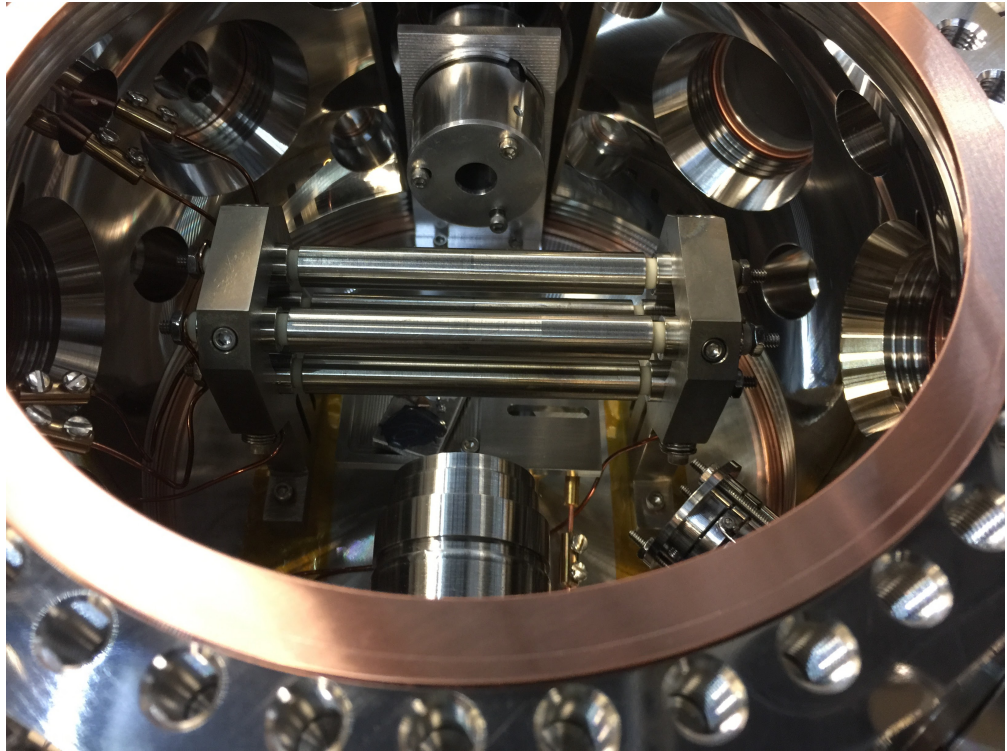


Figure 4.1: The ion trap inside of the experimental vacuum chamber. An Einzel lens and imaging objective are seen on the vertical axis.

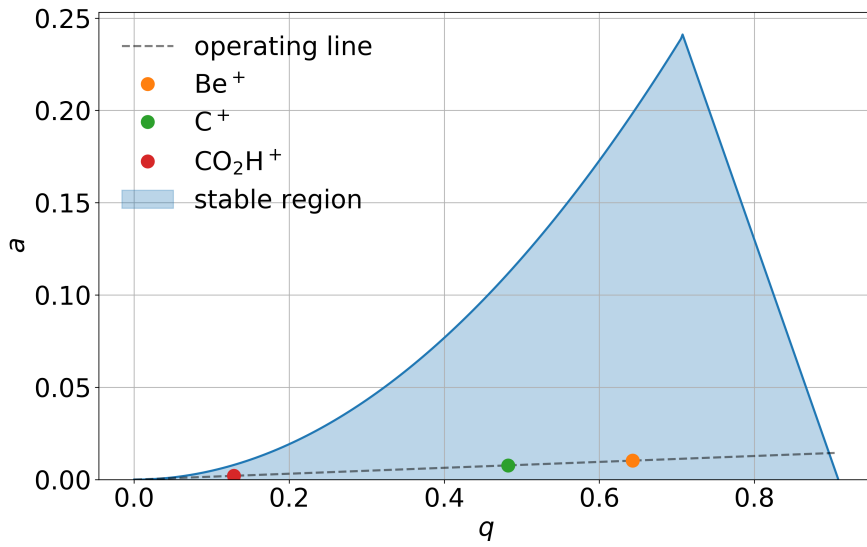


Figure 4.2: Stability diagram of the experimental ion trap with parameters defined in table 4.1. The trap is set up to be stable for ions of interest, including high mass reaction products, from Be^+ , and C^+ at $m/z = 9$, 12 to CO_2H^+ at $m/z = 45$.

4.2 Vacuum Requirements

To reliably laser cool and trap ions into crystals for long periods of time, it is ideal to have ultra-high vacuum (UHV) which is generally defined as having a pressure $< 10^{-9}$ Torr. Collisions with background gasses can be elastic, imparting energy to the ions, possibly enough to prevent a crystal from forming, or they can be inelastic, where a reaction may occur. In both instances, the rate at which these collisions occur is dependent on the density of the background gas in question, and the interaction potential.

For our experiment, we want to look at the reactions between our ions and H_2O introduced via the CBGB, meaning we need to limit the background H_2O content such that we may confidently say the reaction products are solely due to the cold water from the beam. Water is difficult to completely eliminate from a chamber because it sticks to the surfaces of walls when bouncing around, taking more time to reach a pump than other molecules or atoms.

We bake out chamber and all relevant components including the RGA nipple and TOF drift tube, while the turbo pump is constantly on.

We may verify the pressures within the chamber by looking at the reaction rate of:



Which has been observed to be $k_{4.7} = (1.3 \pm 0.4) \times 10^{-9}$, in good agreement with the Langevin rate $k_L = 1.6 \times 10^{-9}$.[35] By monitoring the rate of fluoresce decay with the imaging system scaled by the P-state fraction, we find the pressure in our chamber is of $\approx 10^{-10}$ torr of almost exclusively H_2 , verified separately with the ion gauge.

When introducing the beam into the trap chamber the CBGB is connected to the baked out trap chamber. Although the trap chamber has been baked and clear of background H_2O , we need to concern ourselves with the background H_2O leaking in from the CBGB. When the CBGB stem chamber and trap chamber were directly connected we found that the background pressure of water leaking in from the CBGB region reached values of 10^{-8} Torr as read in the trap chamber, although the PTR was on and the cold CBGB surfaces acted as cryopumps. Since the CBGB region is constantly being opened and closed, it is regularly exposed to atmosphere, where then the surfaces collect H_2O . Although the cold shields are effective in pumping the H_2O out, there is still too much unbaked surface area that a significant amount of H_2O leaked through to the trap chamber.

To get around this issue, we introduce a differential pumping region consisting of a CF 2.75" cross with gate valves on either end, pumped by an Agilent 84FS turbo pump, and a leak valve for further utility, seen in Figure 4.3. Inside of each gate valves, we added blank copper CF gaskets with centered apertures to reduce the conductance between the CBGB chamber and trap chamber while allowing the beam to pass through as unimpeded as possible. The aperture facing the CBGB is 4 mm in diameter, while the one facing the trap chamber is 10 mm in diameter. The CF cross is then baked to remove as much water content as possible. Subsequent tests observing reaction 4.7 while the cross is opened to the trap chamber show no observable difference in background pressure, while having all gate valves opened increased the background pressure to $\approx 2 \times 10^{-9}$ torr, with no discernible

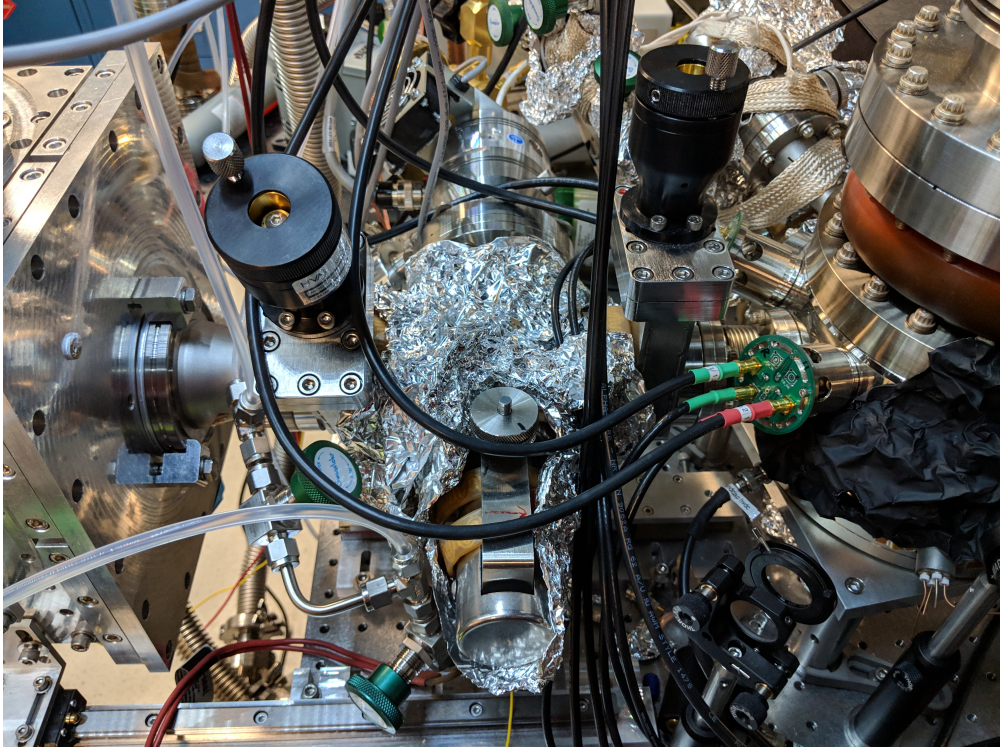


Figure 4.3: Differential pumping region in between the stem and ion trap chambers with gate valves on either end. Blank copper CF gaskets with apertures of 4 mm and 10 mm are placed towards the stem and ion chamber respectively to limit conductance of background gasses while allowing the cryogenic beam through. An Agilent Twistorr 84 FS turbo pump keeps the region at pressures around 10^{-10} Torr and a leak valve allows for controlled introduction of secondary gasses.

contribution from H₂O.

4.3 ⁹Be⁺ Laser Cooling

To reach the low reaction temperatures desired for our experiment, we need both a cold molecule source as well as a cold and controlled ion source. We may trap Be⁺ ions, but given the trap depth of 3 eV, the range of reaction temperatures is vast. Using laser cooling of translational modes of the ions on a closed transition allows us cool down the ion such that clouds and crystals form with temperatures not exceeding 500 mK.[51]

Our atom of choice is ${}^9\text{Be}$, which is the only stable isotope of beryllium with a nuclear spin of $I = 3/2$. Being an alkaline earth atom, ${}^9\text{Be}$ has two valence electrons, and by stripping one off, we are left with an ion with a structure very similar to those of alkali atoms. The states of interest for our work are the ${}^2\text{S}_{1/2}$ ground state and ${}^2\text{P}_{3/2}$ excited state. In the ground state, the hyperfine splitting between the lower $F = 2$ and $F = 1$ manifolds is 1.25 GHz [??](#). Defining the cooling transition on the ${}^2\text{P}_{3/2}$ state from the $F = 2$ ground manifold allows one to access a stretch transition between the ground $m_F = 2$ to excited $m'_F = 3$ states with magnetic fields on the order of 2×10^{-5} T.[??](#) In principle, this scheme does not require any repumping out of the S orbital $F = 1$ manifold. Our apparatus does not easily accommodate magnetic field coils necessary to resolve the hyperfine states, requiring repumping out of the $F = 1$ manifold. Acousto-optic modulators (AOMs) driven at 400 MHz are used to bridge the 1.25 GHz hyperfine splitting.

Addressing the ${}^2\text{S}_{1/2} \rightarrow {}^2\text{P}_{3/2}$ transition is done with a Toptica TA-FHG Pro tuned to 313 nm with a peak power of 400 mW. The fundamental laser light is blue-detuned by 400 MHz from the cooling transition, which is then passed through a 400 MHz AOM to bring it back on resonance. The unperturbed, transmitted light, is then double passed through another 400 MHz AOM to repump the population that has fallen into the ground $F = 1$ manifold. An additional AOM driven at 200 MHz creates red sidebands for both cooling and repump lights create our recapture beams. These aim to cool particularly hot Be^+ ions produced after ablation not well addressed by the main cooling lasers, that would otherwise be lost in A-ramping. The ${}^9\text{Be}^+$ cooling diagram and AOM set up is shown in Figures [4.4](#) and [4.5](#). A feature of this laser set up is since the frequencies we utilize are all produced by the AOM's, we can quickly shut on and off the cooling lasers at will.

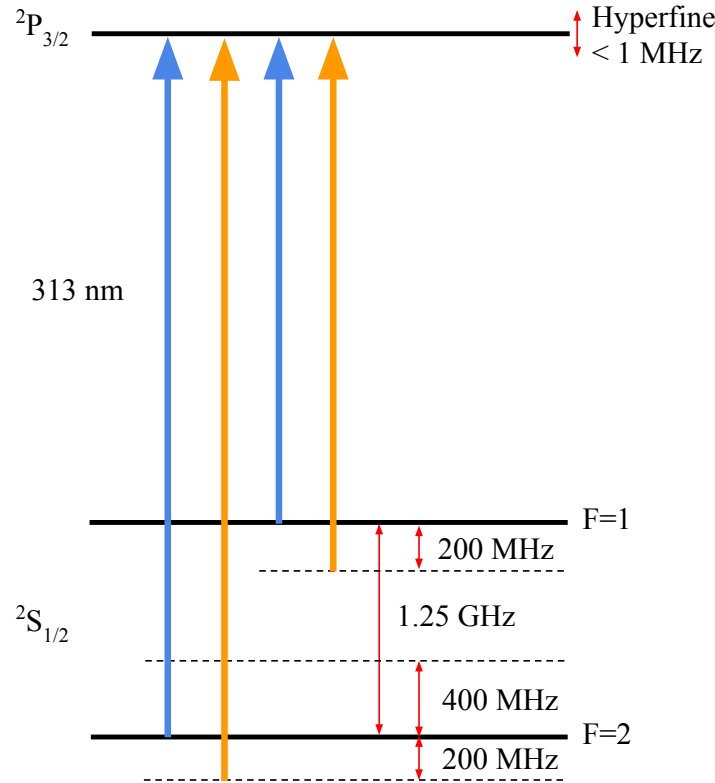


Figure 4.4: Electronic structure of ${}^9\text{Be}^+$ showing the main cooling and repump frequencies (blue) and red detuned reccooling beams (orange). The fundamental light from the laser is blue detuned from the ${}^2\text{S}_{1/2}(F=2) \rightarrow {}^2\text{P}_{3/2}$ transition by 400 MHz (middle dashed line), where an AOM driven at 400 MHz brings it back to resonance. Another AOM driven at 400 MHz is double passed to address the ${}^2\text{S}_{1/2}(F=1) \rightarrow {}^2\text{P}_{3/2}$ repump transition. Both beams are then fed through an AOM driven at 200 MHz to produce redetuned recapture beams to cool particularly hot Be^+ ions poorly addressed by the main cooling beams.

Missing
figure

Laser and AOM's

Figure 4.5: Diagram showing the AOM set up to produce the cooling beams, as well as recapture beams shown in Figure 4.4.

As we excite the cooling transition, force is being imparted onto the ion via absorption of the photons and spontaneous emission. We can define the force to be the product of the scattering rate of a two level system and the momentum of each photon.

$$\begin{aligned} F &= p\Gamma\rho_{pp} \\ &= \hbar k\Gamma \frac{1}{2} \frac{s}{1 + s + 4 \left(\frac{\delta - \vec{k} \cdot \vec{v}}{\Gamma} \right)^2} \end{aligned} \quad (4.8)$$

Where k is the photon's wavenumber, Γ is the linewidth of the excited transition, and ρ_{pp} is the probability of finding the ion in the excited $^2\text{P}_{3/2}$ state characterized by the saturation parameter $s = I/I_s = I/(\frac{\pi hc}{3\lambda^3\tau})$ and laser detuning $\delta = \omega_0 - \omega_l$. We can see that the force the ion feels is dependent on the laser detuning from resonance, which in turn is dependent on the doppler shift of the ion with respect to the laser $\vec{k} \cdot \vec{v}$. In general, the laser frequency (ω_l) is red detuned from the cooling transition ($\omega_l < \omega_0$). In this instance, if the ion is moving towards the laser such that the velocity (v) and k vector are anti-aligned, we see a positive doppler shift in the frequency ($+kv$), decreasing the effective detuning, increasing the scattering rate. When the ion is moving away from the laser while $\omega_l < \omega_0$ is true, we see that the detuning increases, lowering the scattering rate. Each time the ion absorbs a photon, it gains a momentum kick in the photon's direction, meaning the ion preferentially absorbs light that causes it to lose momentum. After absorption, the ion emits a photon after $\tau = \Gamma^{-1}$ time, isotropically, which averages to zero. We can Taylor expand equation

4.8 for small values of v to find this velocity dependence.

$$F(v) = F(v = 0) + \beta v$$

Where we define the damping coefficient:

$$\beta = 4\hbar k^2 \frac{s \frac{\delta}{\Gamma}}{1 + s + 4 \left(\frac{\delta}{\Gamma} \right)^2}$$

In the ion trap, the ion's trajectory is mixed along each axis, allowing for the 3 dimensional laser cooling with just one beam angled from both radial and axial axes of the trap.

4.4 Imaging System

Using the 313 nm laser, we fluoresce the Be^+ ions and cool them down to a cloud or crystal in the ion trap. The scattered light is observed via our imaging system shown in Figure 4.6. The components include the Andor iXon3 camera with EM gain, a 313 nm band pass filter, angled mirror, enclosing lens tubes, and Sill objective lens with 0.2 NA, and 40 mm working distance. The alignment of our objective lens to camera imaging plane yields a magnification of about $\times 5.5$. All of the imaging components are rigidly mounted onto the 3 axis translation stage allowing us to move the focal point without changing the magnification. The total efficiency of our imaging system is

$$\epsilon = \Omega \alpha \beta \gamma \quad (4.9)$$

where Ω is the solid angle the reentrant objective appends, α is the camera's quantum efficiency at 313 nm, β is the camera's exposure time, and γ is the camera's gain. For a fluorescing ion scattering at $\Gamma \times (\rho_{pp} \approx 0.20)$, we expect on the order of 10^5 counts per ion after the imaging inefficiencies.

With images of the ion clouds used in our chemical reaction studies, approximate the temperature of the ions by assuming they are in a harmonic potential. In the same fashion that we derived the trap depth, we may find a characteristic temperature of the ion cloud in the trap from the spacial width. With a very large cloud of ions that are not in a Coulomb

crystal, we estimate a maximum temperature of 500 mK by estimating the physical width of the ion cloud. When compared to the temperature of a gas introduced via leak valve or even the CBGB, the ions in the trap may be considered to effectively have zero velocity.

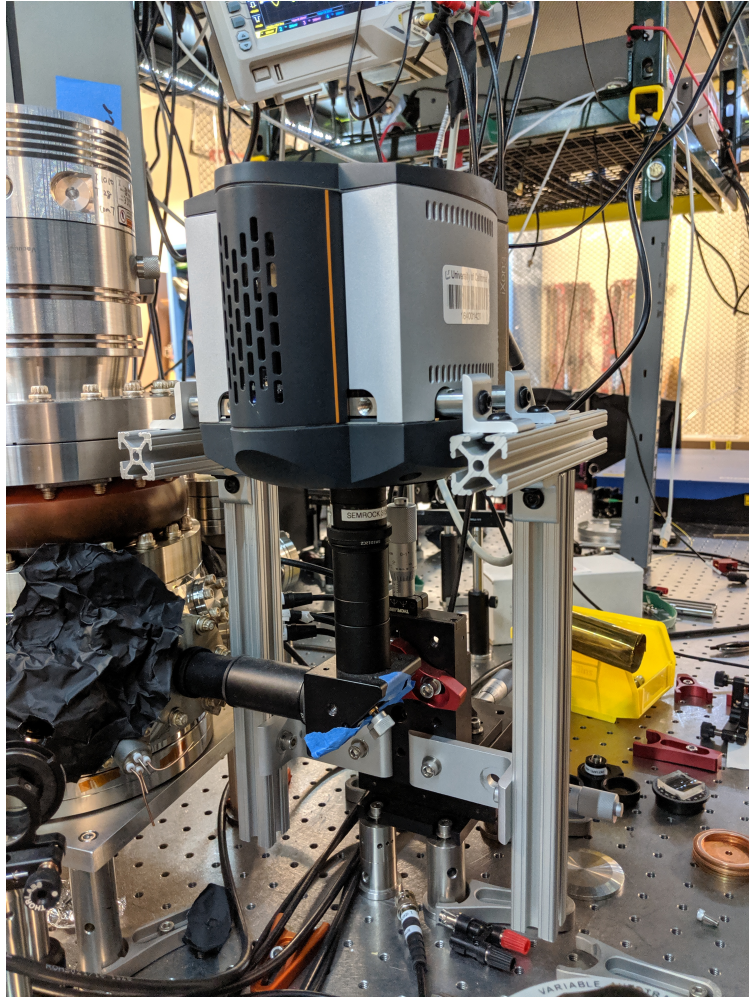


Figure 4.6: The Andor iXon3 camera, enclosed imaging pathway, and objective lens are all mounted onto a 3 axis translation stage. The Sill objective lens is mounted at the end of the imaging tubes, inserted into the reentrant flange. An angled mirror directs the light at a 90° angle up and through a 313 nm bandpass filter placed in front of the camera sensor.



Figure 4.7: Laser cooled Coulomb crystal of Be^+ ions in the LQT imaged with the reentrant imaging system. Dark BeH^+ ions are sympathetically cooled in the middle of the top row as well as the third position from the right.

4.5 Determining Excited State Population

As an ion is exposed to a laser, it continually excites and decays via spontaneous or stimulated emission. Given the laser detuning from resonance and intensity at the ion, the ion comes to an equilibrium where the fraction of time it occupies the excited and ground states is well defined. The integrated photon counts (N) from the iXon camera as a function of the laser intensity and detuning from resonance can be described by

$$\begin{aligned} N &= a\rho_{pp} \\ &= \frac{a}{2} \frac{s}{1 + s + 4(\delta/\Gamma)^2} \end{aligned} \quad (4.10)$$

where a contains the efficiency parameter ϵ from equation 4.9 as well as other unaccounted effects. By mapping the number of collected photons as a function of incident power and/or laser detuning allows us to fit equation 4.10 to find a . Although we may be able to determine a once, we cannot guarantee that it stays the same from day to day as the total number of photons collected can change due to the temperature of the sensor, image focusing, etc. Once a fitted a is found, we can then determine ρ_{pp} as a function of laser power and detuning.

Having a single ion in the trap while sweeping the frequency or power would be ideal, but due to our loading process, we cannot reliably load only one ion, nor can we guarantee there only being one ion. On top of that, the most common residual gasses in a vacuum chamber, H_2O and H_2 both readily react with Be^+ in the excited state limiting the available interrogation time. Instead of a continuous measurement on one ion, we analyze images of

ion chains at various laser powers and find the fluorescence per ion to fit to a generalized form of the scatter rate.

Be^+ ions are loaded into the trap and A-ramps are applied until a chain is formed and the laser detuning adjusted until we see maximum fluorescence on the camera, which coincides with $\delta = \Gamma/2$. Images of the ions are taken at various laser powers and run through a maximum filter algorithm to identify the locations of individual Be^+ ions as seen in Figure 4.8. The portion of the image determined not to be an ion is then averaged to obtain the background pixel value, which is then subtracted from each localized ion image. The pixel values over each localized ion is then summed to yield a total fluorescence value, which is then averaged for each image, as shown in Figure 4.9. By performing a least squares fit on the collected fluorescence per ion as a function of incident power, we find the generalized efficiency a , revealing the P-state fraction at each power in ρ_{pp} , shown in Figure 4.10. This calibration can then be used to tune the P-state fraction using both laser power and frequency detuning.

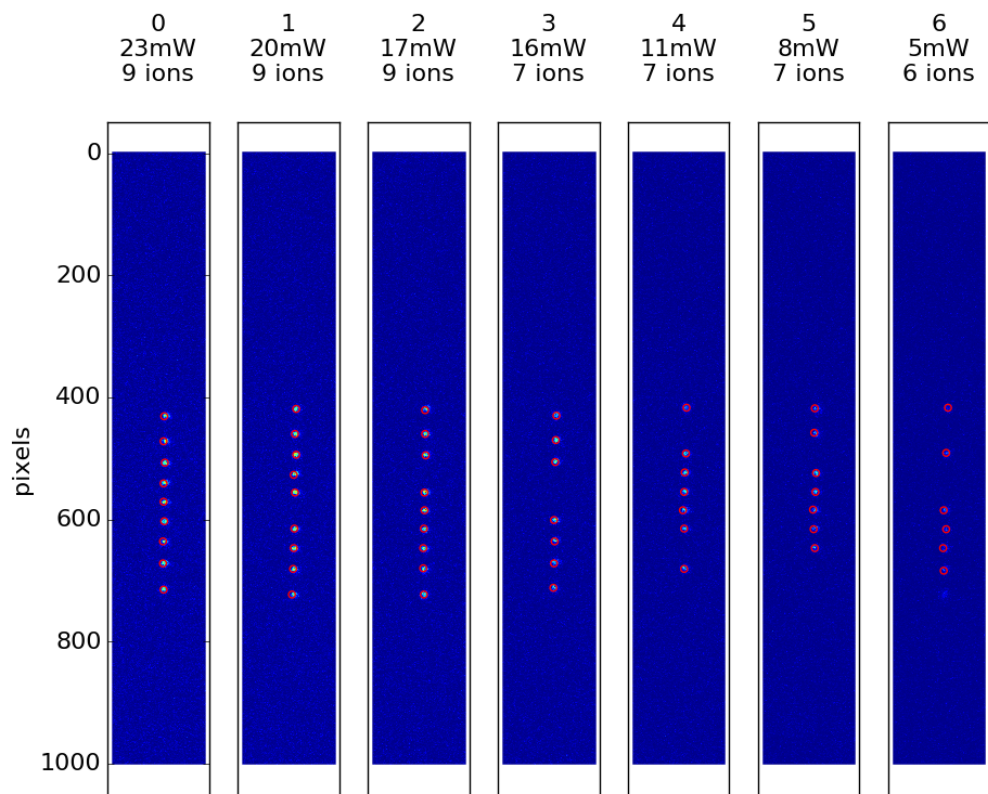


Figure 4.8: A set of ion images taken at various 313 nm powers run thorough a maximum filter algorithm that identifies local maxima, representing individual ions (circled in red). gaps in the ion chain are due to reactions with background H₂ producing BeH⁺, which occupy crystal sites without fluorescing.

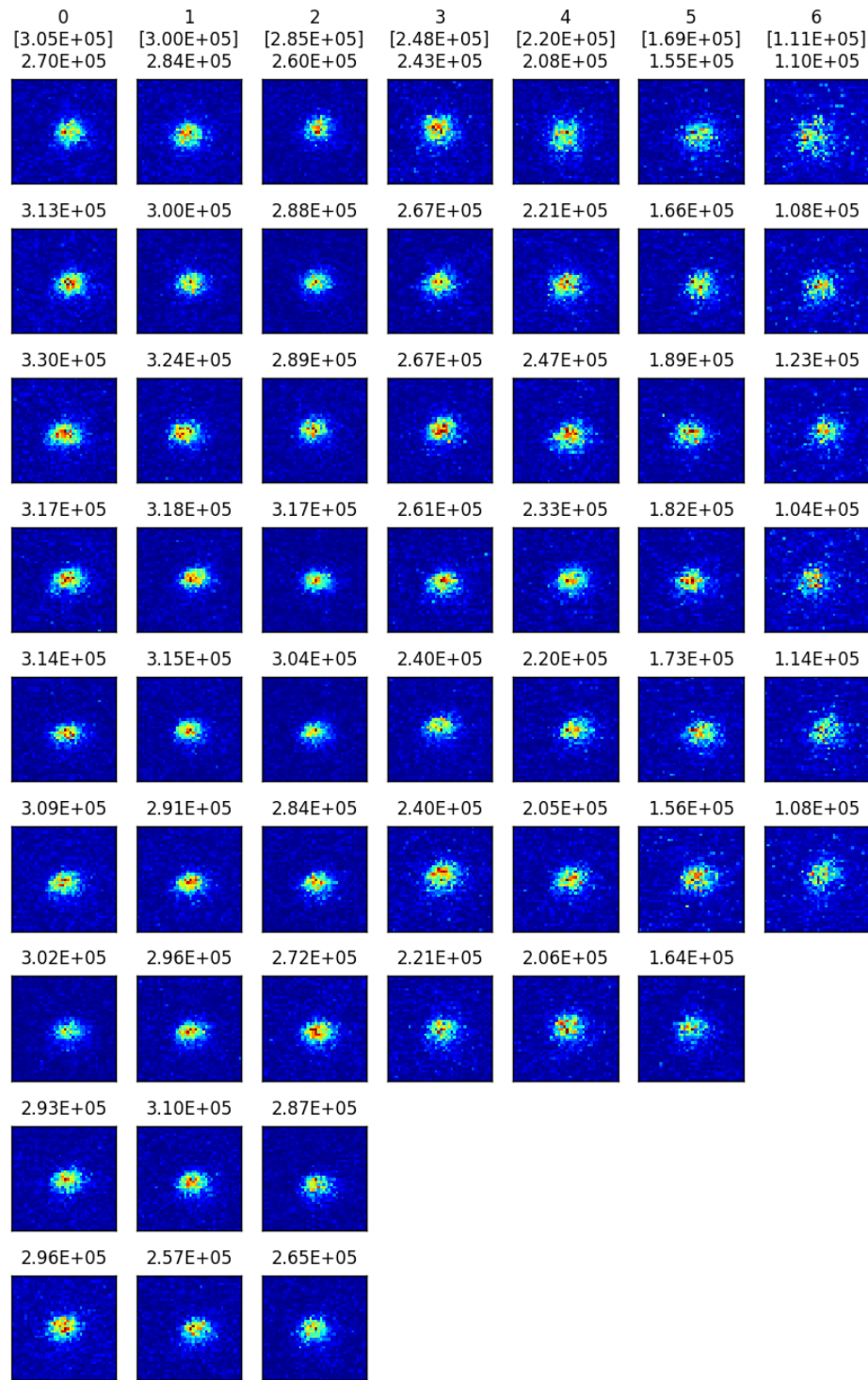


Figure 4.9: Individual ions identified from images in figure 4.8. Integrated pixel values with subtracted background counts shown for each image, a set's averaged value is shown in brackets.

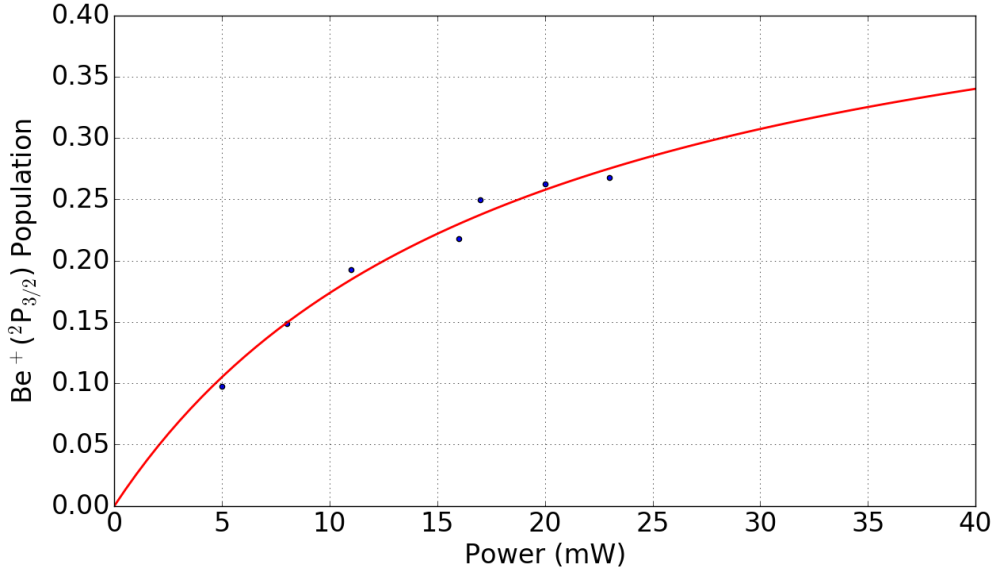


Figure 4.10: P-state fraction curve fitted to incident laser power at a fixed detuning of $\delta = \Gamma/2$. Total fluorescence value is normalized by fitted efficiency parameter a to yield ρ_{pp} .

4.6 Time of Flight Mass Spectrometer (TOF-MS)

One of the key components of this experiment is the fact that charged reaction products stay within the ion trap, allowing us to accumulate all stages of a reaction network. Direct identification of the species via fluorescence is ideal, as the signal is unambiguous, and generally unique to a species. Leaning on direct fluorescence becomes increasingly difficult as more and more species are introduced. In our particular case, it becomes prohibitively difficult, as we may expect to trap 10's of species at once, where in some cases, the exact reaction products are not known. To identify what is in our trap, we use a species agnostic detection method in the form of a time of flight mass spectrometer (TOF-MS). Our TOF apparatus design and electronics were extensively developed by Steven Schowalter and Christian Schneider of the Hudson group.[\[37, 36\]](#)

The TOF works by switching the rod voltages from a trapping RF potential to one where the ions are ejected out of one side. When trapping, RF voltages are applied onto diagonal rods, while DC voltages on the others. During ejection, the trapping region turns into the

acceleration region as adjacent pairs of rods ramp to constant voltages where the pair of "back" rods are at a higher potential than the pair of "front" rods seen in Figure 4.11. TOF's operating with higher $m/z \approx > 100$ need to have well matched HVDC values for the rods, without much concern over the rising voltages. In our experiment, due to the low m/z of Be^+ , the ions were extremely susceptible to mismatches in the rod voltages during the ramp up, requiring particularly good overlap seen in $\sim 0.8 - 1.2 \mu\text{s}$ of Figure 4.11

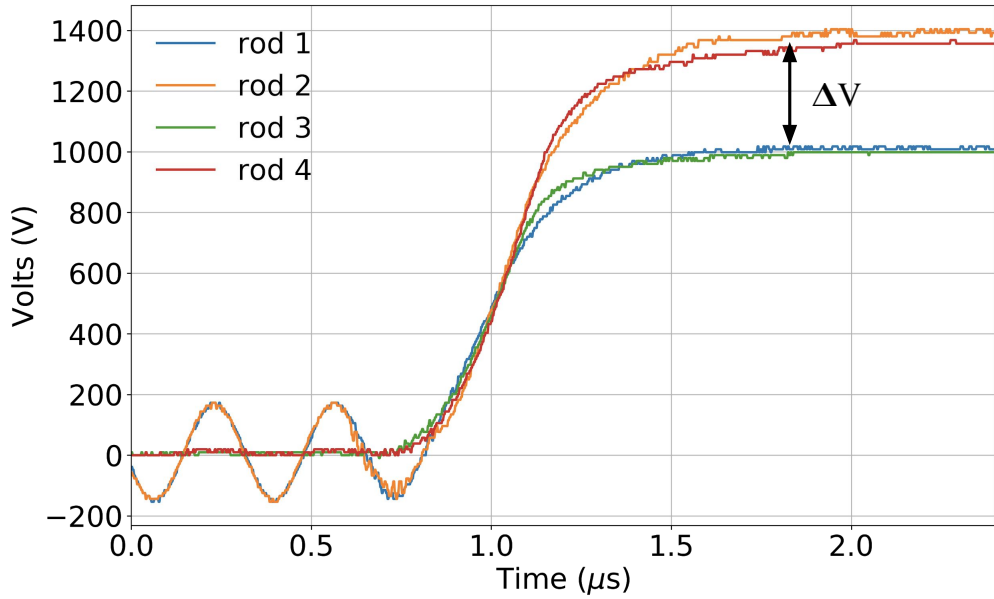


Figure 4.11: Voltages of ion trap rods during ejection into the TOF taken from an oscilloscope. TOF facing front (1 and 3) and back (2 and 4) trap rod pairs shift from the trapping RF operation to HV values after a positive zero voltage crossing. The front pair reaches a nominal 1000 V, while the back pair reaches 1400 V, creating an accelerating potential ΔV , ejecting the trapped ions.

As the ions are ejected radially, they are accelerated out of the trap, through an Einzel lens focusing element, and through a field-free drift tube of length $D = 320 \text{ mm}$ where they impact a micro-channel plat (MCP) and are detected (Figure 4.12). To first order, during ejection the ions in the ion trap feel the same potential ΔV , therefore, the same kinetic

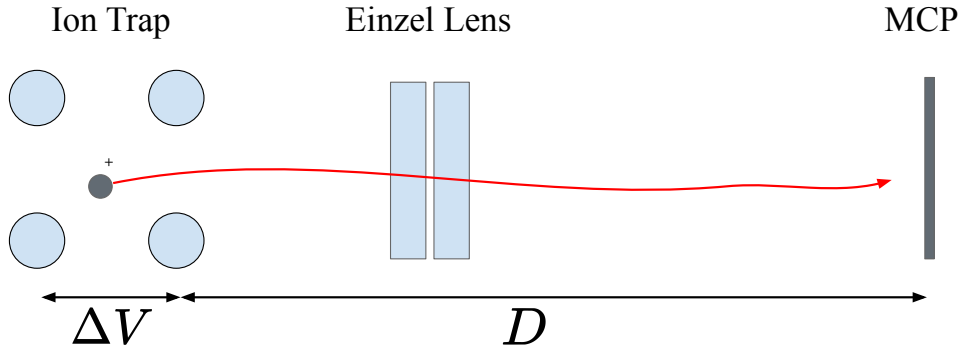


Figure 4.12: Diagram of the TOF ejection where the ions in the trap are radially accelerated out of the trap with potential ΔV . An Einzel lens ion focusing element focuses the ions onto the MCP at the back of the field free region of length D .

energy

$$\Delta V q = \frac{1}{2} m v^2.$$

But solving for the velocity v yields a mass dependent velocity, thus, a mass dependent arrival time t ,

$$v = \sqrt{\frac{2\Delta V q}{m}}$$

$$\implies t = D \sqrt{\frac{m}{2\Delta V q}}.$$

With fast electronics, we may resolve ions to sub amu precision, giving us a powerful tool to identify what is in our trap. An example of Be^+ and C^+ TOF detection traces is shown in Figure 4.14 with a ratio $m/\Delta m \approx 100$.

To first order, the mass to charge ratio (m/z) is then proportional to t^2 where t is the arrival time, which is proportional to the drift tube length D . It may seem like greater mass separation is achieved with a longer drift tube, but that is not the case. We made the assumption that the ions are accelerated by the same potential, but in reality, the ions occupy a finite spacial extent in which the potential felt by an ion is related to its location within the trapping region at the time of ejection. An ion in the center of the trap at the time of ejection will have a distance $d_0 \approx 4.8$ mm to travel in the acceleration region, while those towards the back/front pair of rods will have distances $d = d_0 \pm \delta d$. As these ions fly

down the drift tube, although the ions initially closer to the front have a shorter distance to travel, the ones originating further back have a higher velocity and will catch up and overtake the slower ions. This mismatch will cause the ion arrival times of a single species to spread out as D increases past the point where all the ions overlap.

On top of considering the spacial extent of the ions in the trap, we must also consider the multiple acceleration regions. The rods that the trap consists of produce a fairly uniform electric field within the trap region E_d , but outside, there is still an accelerating electric field E_s , but primarily from the front rods. To minimize the ion defocusing at the MCP, we find that the drift tube length D is uniquely defined by the trap geometry and voltages,??

$$D = 2d_0 k_0^{3/2} \left(1 - \frac{1}{k + \sqrt{k}} \right) \quad (4.11)$$

where $k = (E_s + E_d)/E_s$.

4.6.1 TOF Signal Integration

The MCP detector produces a current proportional to the number of ions that activate its surface, which is then read by a fast oscilloscope. To determine the total number of ions, we integrate the current as a function of arrival time to find a total charge for each calibrated amu range (colored regions in Figure 4.14). A difficulty is determining whether or not an integrated peak corresponds to an ion, or simply noise. For each TOF trace, we find a region of high mass (e.g. $m/z > 45$), where there aren't any ions and bin single amu chunks to produce a histogram. This histogram is then fitted to a Gaussian to determine the standard deviation, where then we may find a 90% confidence interval ($\approx 1.3\sigma$). This value then defines our signal threshold, if an integrated signal is below this value, it is rejected and a zero is returned with error bars equal to this threshold, otherwise it is reported as a true ion signal.

4.7 Dual Species Loading

Although loading and cooling Be^+ ions is fairly straight forward, it is not as clear as how to load C^+ ions into the trap with Be^+ reliably. Early attempts involved using the home-made electron gun to dissociate CO gas introduced via leak valve, where all possible ionized products of CO were detected (C^+ , O^+ , and CO^+). Even when loading into an empty trap, it was not possible to reliably isolate the C^+ via A-ramping of the trap RF voltage. Prolonged use of the electron gun directly towards the ion trap also caused charging that would slowly dissipate and change the trap parameters. On top of these complications, it would not have worked in conjunction with ablation loading Be^+ , as these cannot occur simultaneously.

Instead of using two different methods to load the different ion species, ablating samples of both species simultaneously was found to be the best method. A sample of beryllium metal was placed on top of a piece of graphite on the target holder so that both samples were in view of the ablation laser. The diagram shown in Figure 4.13 allowed us to separate the Continuum Minilite II Nd:YAG ablation laser into two beam with independent alignment and focal planes. The polarization of the laser light is rotated with a half-waveplate, which then enters a polarizing beam splitter (PBS), allowing for tuning of power into either path. The vertically polarized reflected light is reflected off a second PBS and is steered up to the objective lens and then focused into the chamber. The horizontally polarized light transmitted through the first PBS is aligned through an adjustable telescope system. This light is then realigned with the vertically polarized light on the second PBS, co-propagating into the chamber. This "delay stage" for the horizontal light allows for independent focusing and alignment onto a target.

Blocking one beam allowed for adjustments for the ablation of each species independently. When loading C^+ , we found a strong dependence of the trapped species and the fluence. Lower fluence created not only C^+ , but clusters of, C_2^+ , and C_3^+ as well. Tight focusing of the beam improves the efficiency of creating only C^+ , but some Cn^+ is still usually produced. By changing the trap's a parameter (A-ramp) via changing the V_{DC} (equation 4.2), we can change the stability diagram for the trap, causing higher m/z ions to become more unstable.

The higher mass Cn^+ ions are preferentially kicked out of the trap, while the lighter Be^+ and C^+ are less affected, allowing us to load clean samples of only Be^+ and C^+ as seen in Figure 4.14.

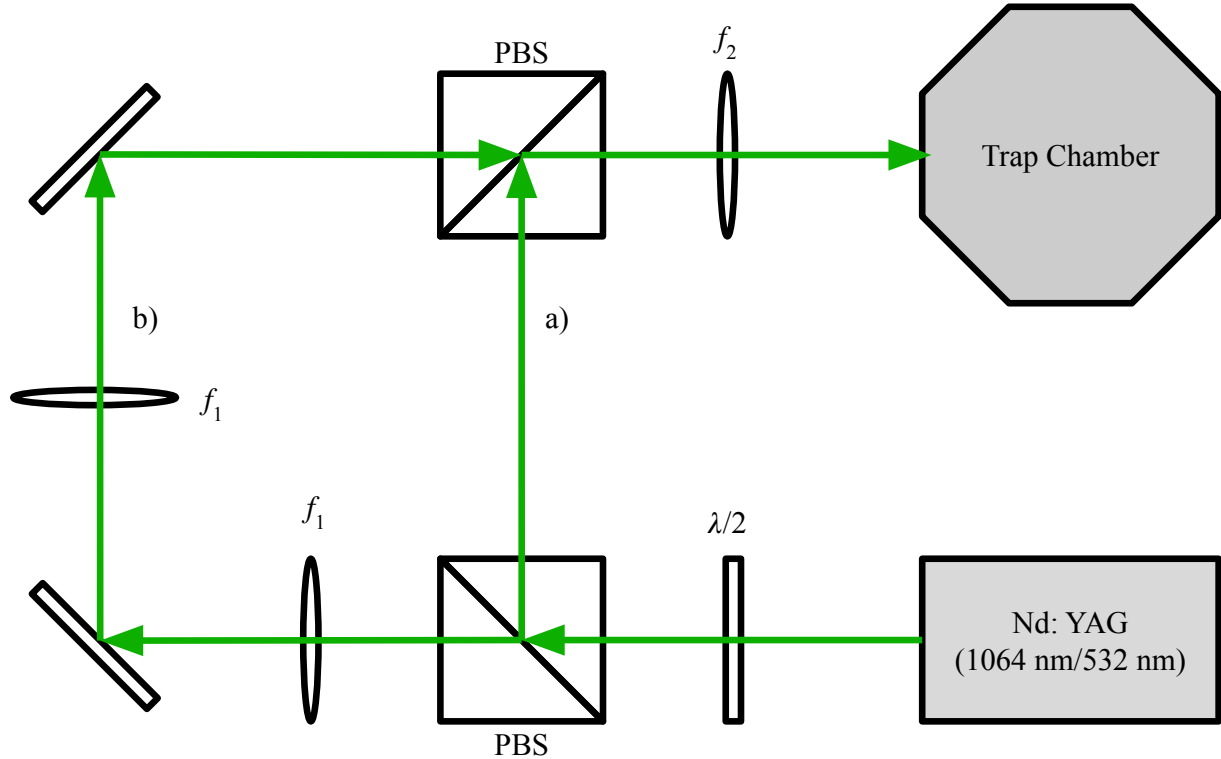


Figure 4.13: Diagram of the single laser, dual ablation set up. The 1064 nm/532 nm YAG pulse is split into two paths via polarizing beam splitter (PBS), and recombined such that they proceed through the same focusing element into the chamber to hit two different targets. Path a) is used for the ablation of graphite to produce C^+ , while path b) is independently focused and positioned to ablate beryllium metal to produce Be^+ . The ratio of power in each path is adjusted via the half waveplate directly in front of the laser.

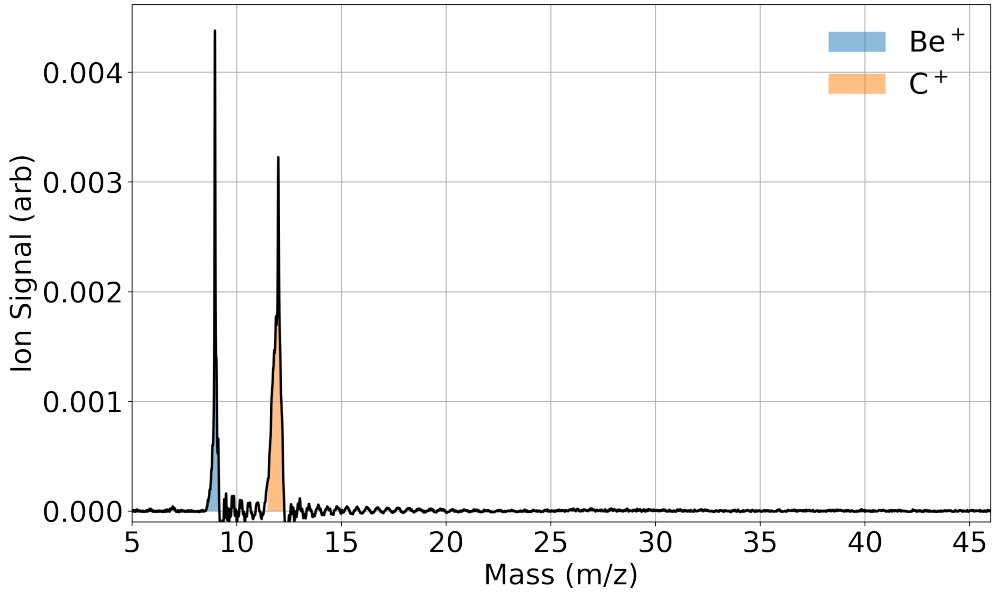


Figure 4.14: TOF trace of simultaneous Be^+ and C^+ ablation loading averaged over 10 shots. A soft A-ramp is applied after loading, ejecting any unintentionally loaded Cn^+ clusters. The C^+ peak is narrowed from sympathetic cooling with the laser cooled Be^+ ions.

An important consideration is that the amount of ions loaded from shot-to-shot is not identical; the amounts may be similar, but can drift over time, especially for the C^+ peak, as the ablation of graphite is less reliable than beryllium metal. As we run experiments, which can take upwards of 200 shots to complete, we cannot make assumptions on the total number or ratio of loaded ions. With Be^+ , we may use the camera in conjunction with the TOF and normalize the total Be^+ reaction network with the fluorescence. Because the Be^+ fluorescence has no indication on the amount of C^+ loaded into the trap, the C^+ reaction network must then be normalized separately for total ion count in each division.

CHAPTER 5

Optical Control of Reactions between Water and Laser-Cooled Be⁺ Ions

5.1 Prologue

When exposing Be⁺ and C⁺ in the ion trap to H₂O vapor introduced from the leak valve, we found that the reaction Be⁺ + H₂O → BeOH⁺ + H occurs. Interestingly, it occurred at a slower rate than that of C⁺ + H₂O, where by ADO, the rates should be nearly indistinguishable. Towards our goal of understanding C⁺ + H₂O, we needed to understand the role that Be⁺ may have, as all of the charged reaction products will stay in the trap. Along the way, we gained a fuller understanding of the Be⁺ + H₂O reaction, which proved to be an invaluable tool for subsequent studies. The rate constant was both experimentally and theoretically found to be excited state dependent, despite the fact that both reaction pathways are exothermic. Knowing this rate constant to a high degree of confidence allowed us to characterize the water density at the ion trap from the CBGB, which neither our RGA nor ion gauge could detect.

5.2 Introduction

Low-temperature reactions of simple ions with small molecules play a central role in astrochemical environments from interstellar clouds to cometary comae to planetary atmospheres, including that of Earth[2, 23]. The chemical evolution of interstellar molecular clouds ultimately yields the seedbed from which new stars and planets are born and the raw

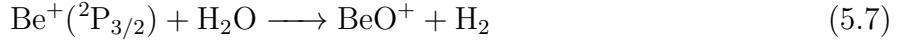
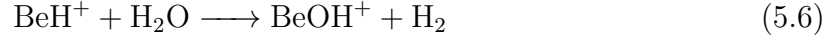
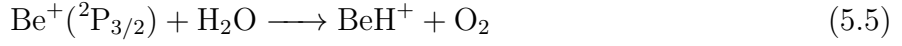
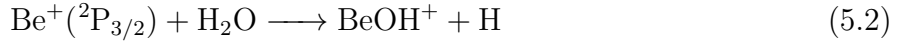
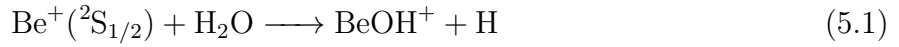
materials from which life likely developed. A firm understanding of the reaction rates for a host of elementary ion-molecule reactions is essential to accurately model these environments these environments. Techniques such as selected ion flow tubes (SIFTs)[1], guided ion beams[3], and supersonic flows (CRESU)[39] have improved our empirical understanding of these processes; however, each has its own limitations.[42, 43] Theoretically, it has long been recognized that these ion-molecule reactions are often barrierless, and their rates are frequently described by capture models.[16] However, recent studies have revealed that dynamical features can sometimes prevail,[28, 25, 6] in which case statistical treatments may not be accurate.[18, 9] Therefore, new experimental and theoretical efforts are needed to accurately address ion-molecule chemistry. Furthermore, there have been very few experimental studies of gas-phase reactions between metal ions and water, especially at low temperature, despite their importance for metal ion chemistry in a range of environments.[19, 32, 50]

Singly ionized beryllium is a particularly attractive metallic reactant to use for such studies because it is both theoretically tractable and experimentally highly controllable. The relatively simple electronic structure of this three-electron ion allows both highly accurate characterization of its electronic structure and laser cooling,[4] and the low mass of Be^+ lends itself to high motional frequencies as well as efficient sympathetic cooling of other chemically interesting atomic ions when employed in ion traps.[7, 35, 24, 38] For the molecular reaction partner, H_2O is arguably the most important molecule in chemistry, and theoretical studies of its reactions with a single atom have been reported on full-dimensional potential energy surfaces (PESs).[26, 44, 34, 27, 53] Thus this system of reagents provides an opportunity to perform a high-resolution comparison between experiments and theory for a molecule-ion system.

5.3 Experimental

To study the $\text{Be}^+ + \text{H}_2\text{O}$ reaction, Be^+ was loaded into the trap and cooled with the 313 nm laser, then exposed to H_2O vapor introduced from the leak valve.

To minimize experimental errors, a combination of fluorescence detection and TOF measurements were used in tandem. Using both methods together, compared to only using the TOF, allows us to cut down the data collection time, which greatly reduces the effects of drifts in laser power and locking. The initial fluorescence signal determines the reaction time zero as well as normalize the initial ion number for the TOF traces. TOF traces are taken at various reaction times to determine the relative reaction product signals via shared fitting of solved differential equations including all possible reaction pathways shown in Figure 5.3. In total, we consider the following 8 reaction pathways, all of which are thermochemically allowed.



Typical TOF traces (10 sample average) at reaction times $t = 0$ and 70 s with 7 and 26% relative $\text{Be}^+(^2\text{P}_{3/2})$ state excitation are shown in Figure 1A,B, respectively. At $t = 0$ s, a large peak of $m/z = 9$ (Be^+) and a smaller one of $m/z = 9$ (BeOH^+) are evidenced in the TOF trace (blue line), which indicates that Be^+ ions are the main species in the trap at $t = 0$. The finite amount of BeOH^+ at $t = 0$ reflects the fact that reactions 5.1-5.8 happen even during the loading process and that the A-ramp mass filtering procedure is imperfect. At $t = 70$ s, a $m/z = 19$ peak emerges when more Be^+ ions are excited to $^2\text{P}_{3/2}$ state (figure 5.1), which we identify as H_3O^+ resulting from reactions 5.3 and 5.4. The $\text{BeOH}^+ / \text{H}_3\text{O}^+$ ratio, $\eta(P_P)$, is measured by integrating both peaks for the experimentally controlled excited-state population P_P . The BeOH^+ signal includes the amount unfiltered

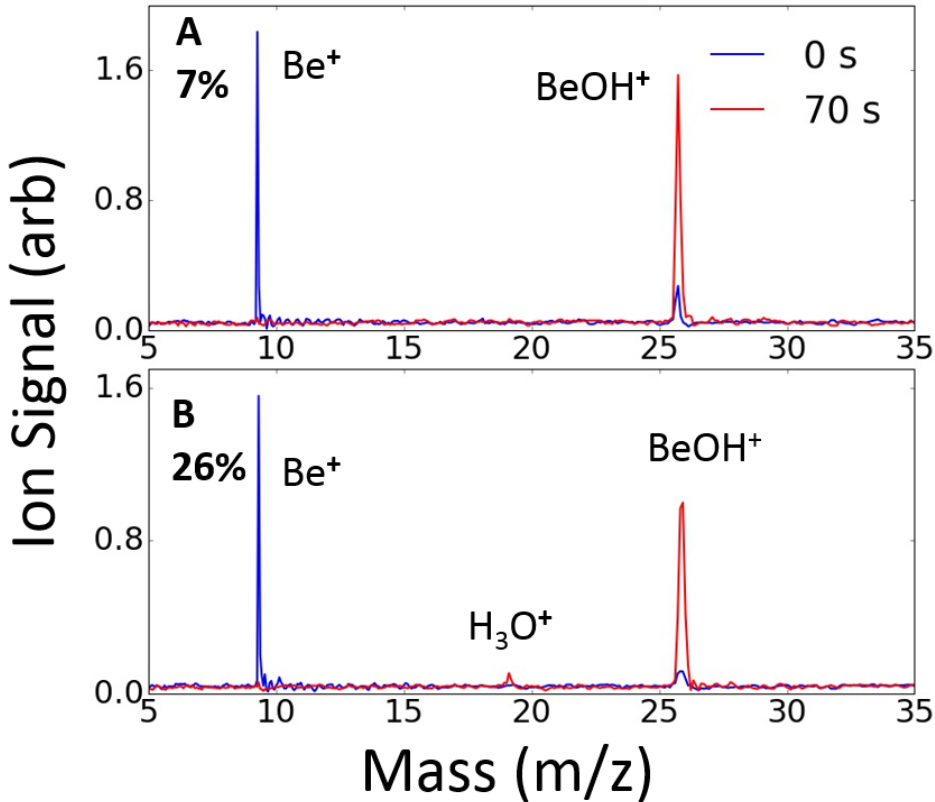


Figure 5.1: TOF signal (averaged over 10 trials) at reaction time $t = 0$ and 70 s with (A) $P_p = 7\%$ (A) and (B) $P_p = 26\%$. A clear $m/z = 19$ peak emerges when more Be^+ ions are excited to ${}^2\text{P}_{3/2}$ state. The $\text{BeOH}^+ / \text{H}_3\text{O}^+$ ratio for this case ($P_p = 26\%$) is measured to be $\eta(0.26) = 0.039 \pm 0.006$ by integrating both peaks in B when $t = 70\text{ s}$.

during loading, products from both reactions 5.1 and 5.2, as well as, in principle, the two-step reactions 5.5, 5.6, 5.7, and 5.8. The H_3O^+ signal is produced via the two-step reactions 5.35.4. Whereas we do not observe products from reactions 5.5, 5.6, 5.7, or 5.8 (see Figure 5.3). They are thermochemically allowed and therefore included in our analysis, which sets upper limits on their reaction rate coefficients.

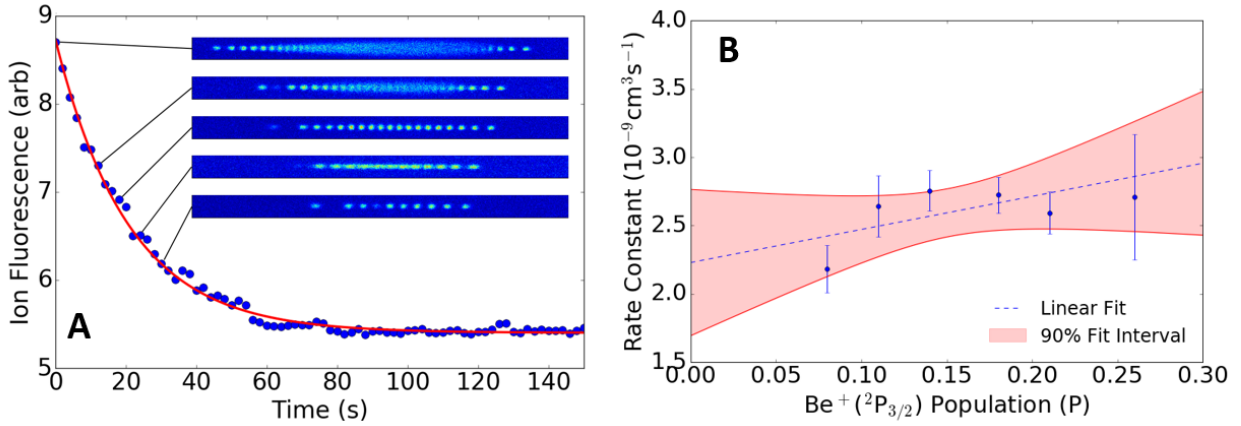


Figure 5.2: (A) Typical fluorescence decay measurement. The inset images are a subset of the original ion fluorescence images recorded by the camera. The red curve is an exponential fit (with a free offset) to the data, which gives the total reaction rate. (B) Total reaction rate coefficient as a function of $\text{Be}^+ ({}^2\text{P}_{3/2})$ state population can be used to separate the contributions from the ground and excited states of Be^+ .

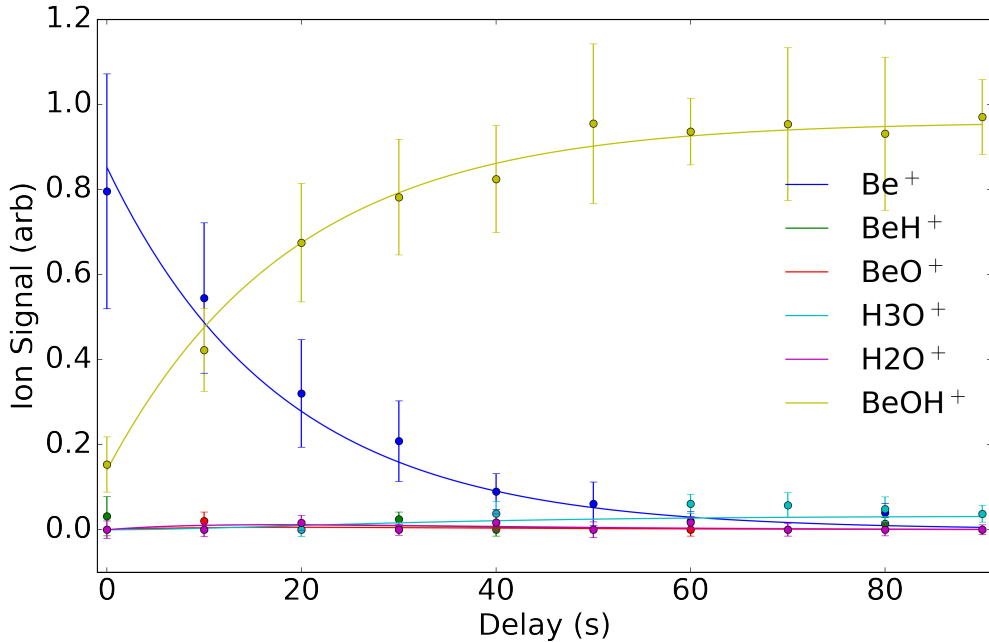


Figure 5.3: The temporal evolution of Be^+ in the trap as a function of reaction time as well as the solutions of differential equations fitted to the kinetics data with $P_P = 26\%$.

5.4 Results and Discussion

The total reaction rate is given by $\Gamma_t = \rho_{\text{H}_2\text{O}} k_t$, where $\rho_{\text{H}_2\text{O}}$ is the H_2O density measured the RGA calibrated to the ion gauge (section B) and k_t is approximated as $k_t = P_S k_1 + P_P k_2 + P_P k_3$, where P_S and P_P are the Be^+ population in the ${}^2\text{S}_{1/2}$ and ${}^2\text{P}_{3/2}$ states, respectively, and k_i is the reaction rate coefficient of reaction i . Reaction eq. (5.4) has been studied by other groups, reporting a rate coefficient of $(2.05 \pm 0.010) \times 10^{-9} \text{ cm}^3/\text{s}$.^[20] The measured $\text{H}_3\text{O}^+ / \text{BeOH}^+$ ratio is given from the reaction rates by:

$$\eta(P_P) = \frac{P_P k_3}{P_S k_1 + P_P k_2} \quad (5.9)$$

To use equation 5.9 to extract the individual rate coefficients (k_i), the total reaction rate Γ_t is first measured by monitoring the Be^+ fluorescence decay with a camera, as shown in Figure 5.2A. Fluorescence decay is monitored directly after a DC voltage applied to trap electrodes is used to filter out the heavier products from the trap to allow better crystallization of the Be^+ ions by reducing ion-ion heating.^[8] The inset of Figure 5.2A shows typical fluorescence images of the Be^+ coulomb crystal at various times. Fluorescence is used to measure the total reaction rate because the total measurement time is 30 times shorter than using the TOFMS (Figure 5.3). To determine the separate rate coefficients for the Be^+ ground and excited states, we measure the total reaction rate coefficients for different excited-state fractions, shown in Figure 5.1. A linear fit (blue line) is found using the least-squares method. The vertical intercept of this fit gives the Be^+ ground-state reaction rate coefficient $k_{5.1} = (2.2 \pm 0.3_{\text{stat}}) \times 10^{-9} \text{ cm}^3/\text{s}$, whereas the sum of the slope and intercept gives the total excited-state Be^+ reaction rate coefficients $k_{5.2} + k_{5.3} = (4.7 \pm 1.7_{\text{stat}}) \times 10^{-9} \text{ cm}^{-3}/\text{s}$. Using equation 5.9, the reaction rate coefficients of reactions 5.2 and 5.3 are then calculated to be $k_{5.2} = (4.2 \pm 1.6_{\text{stat}}) \times 10^{-9} \text{ cm}^{-3}/\text{s}$ and $k_{5.3} = (0.47 \pm 0.11_{\text{stat}}) \times 10^{-9} \text{ cm}^{-3}/\text{s}$, respectively. The ratio of reaction rate coefficients for reactions 5.3 to 5.2 is therefore $k_{5.3}/k_{5.2} = 0.11 \pm 0.03$ independent of systematic errors in the density measurement. Charged products from reactions 5.5 and 5.7 are not directly observed and an upper bound is found to be $< 5 \times 10^{-10} \text{ cm}^3/\text{s}$, set by the integrated signal threshold. Reactions at these upper

bounds for the rate coefficients do not significantly change the analysis above, justifying their exclusion from k_i .

It is instructive to compare these measured rate coefficients to those predicted by capture theory. Since the translational energy of the laser-cooled Be^+ ions is < 0.5 K, the energy of the room-temperature water sets the reaction kinetic energy of $\text{Be}^+ + \text{H}_2\text{O}$ in the center of mass frame of 100K. The internal state distribution of the H_2O is assumed to be given by the 300 K. The internal state distribution of the H_2O is assumed to be given by the 300 K. Because H_2O has a dipole, we use the ADO theory (equation 2.26) to estimate the rate constant. The ADO model predicts that both the ground and excited Be^+ states react with a rate coefficient $k_{\text{ADO}} = 4.1 \times 10^{-9} \text{ cm}^3/\text{s}$ at 100 K reaction temperature, roughly two times larger than measured for the ground state, but in agreement with the measured reaction rate of the excited state. Since the experimental rate constant agrees well with the theoretical rate, we may generalize 5.1 and 5.2 to:

$$k_{5.2+5.1}(T) \approx (0.54)k_{\text{ADO}}(P) + (0.49)k_{\text{ADO}} \quad (5.10)$$

However, because it is long-range, the ADO model cannot provide the branching ratio and state-dependent information and is therefore insufficient for describing the observed reactions. Hua Guo at UNM helped us in making theoretical calculations on the reaction dynamics by method of Quasi-Classical Trajectory Calculations (QCT-Calculations) on a full-dimensional potential energy surface (PES).^[54] They calculate that the intermediate state (IM1) in Figure 5.4 on the ground state reaction pathway causes about 46% of the incoming trajectories to reflect back to the entrance channel yielding a rate constant $k_{5.1\text{th}} = (2.02 \pm 0.04) \times 10^{-9} \text{ cm}^3/\text{s}$. The excited state pathway does not have a submerged barrier of this level, but does have a nonadiabatic transition bringing it down to the ground state product channel.

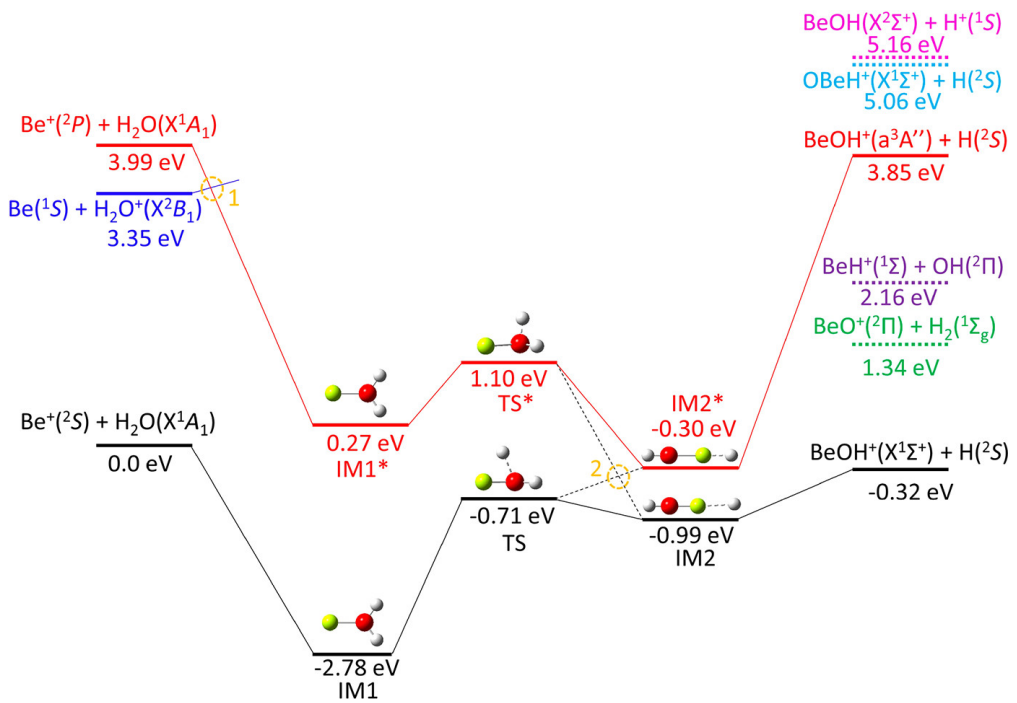


Figure 5.4: Energetics of both the ground- and excited-state reaction pathways for the $\text{Be}^+ + \text{H}_2\text{O}$ reaction. Whereas reaction 5.1 proceeds on a single adiabatic PES, the reactions involving excited Be^+ depend on nonadiabatic transitions between different PESs (yellow circles). The submerged well on the ground-state reaction pathway prevents 46% of the trajectories to reflect back to the entrance channel. (Taken from [54])

5.5 Conclusion

In short, chemical reactions of laser-cooled Be^+ ions with room-temperature water vapor have been studied experimentally and theoretically for the first time. Ground-state Be^+ ions produce only $\text{BeOH}^+ + \text{H}$ with a reaction rate coefficient of $k_{5.1} = (2.2 \pm 0.3_{\text{stat}}) \times 10^{-9} \text{ cm}^2/\text{s}$, whereas the excited-state Be^+ not only creates $\text{BeOH}^+ + \text{H}$ with a reaction rate coefficient of $k_{5.2} = (4.2 \pm 1.6_{\text{stat}}) \times 10^{-9} \text{ cm}^3/\text{s}$ but also gives $\text{H}_2\text{O}^+ + \text{Be}$ with a reaction rate of $k_{5.3} = (0.47 \pm 0.11_{\text{stat}}) \times 10^{-9} \text{ cm}^3/\text{s}$. Electronic structure calculations indicate that these two products are both produced via nonadiabatic pathways. The ground-state reaction rate is roughly half of that predicted by typically employed capture models but in good agreement with zero-point-corrected QCT calculations on an accurate full-dimensional global PES based on high-level ab initio calculations. These calculations reveal that the lower reaction rate is a consequence of chemical dynamics due to a submerged barrier in the product channel.

CHAPTER 6

Isotope-selective chemistry in the $\text{Be}^+(\text{^2S}_{1/2}) + \text{HOD} \rightarrow \text{BeOD}^+/\text{BeOH}^+ + \text{H/D}$ reaction

6.1 Prologue

After finishing the work on the $\text{Be}^+ + \text{H}_2\text{O}$ reaction, we turned our attention to focus more on branching ratios. Getting rate constants was troublesome given the requirement of having an absolute pressure measurement, while branching ratios measurements can be obtained through a single TOF trace. With our fuller understanding of the $\text{Be}^+ + \text{H}_2\text{O}$ reaction network, we focused on reaction 5.1, for Hua Guo's group at UNM had calculated a full ground state PES. To capitalize on this, we turned to the question of whether or not there are dynamics hidden in the reaction pathway that can be seen via deuteration of H_2O . This proved to be a long process in its own right. Water is notoriously sticky inside vacuum chambers and to have a reliable reading on the isotopologue ratio, or to simply push this ratio towards more H or D, required weeks of data collection. At the end, we found what is an expected result, that the branching fractions follows statistical state counting with a (0.58:0.42), ($\text{BeOD}^+:\text{BeOH}^+$) ratio.

6.2 Introduction

Together, isotope substitution and the measurement of the resulting product branching ratios provide important details about reaction dynamics and are often used to identify reaction pathways and understand bond-selective chemistry.[?, 10, 55] Important examples include X

+ HOD ($X = H, F, Cl, O$) reactions, where the branching ratios are experimentally controlled by selective excitation of the O–H or O–D bond.[40, 5, 30, 56, 44, 45, 15, 58, 41] It is now understood that a highly-accurate potential energy surface (PES) is crucial for performing theoretical calculations of the product branching ratio, where subtle, difficult to identify, PES features have been found to significantly affect the results.[41]

A sophisticated understanding of radical-molecule reaction dynamics is continuing to develop from extensive experimental and theoretical studies. However, despite their importance in interstellar chemistry, where the isotopic branching ratios strongly influence the products of the interstellar cloud chemical network,far less progress has been made in the study of ion–molecule reactions at low temperature. This is largely due to the challenges associated with both the experimental and theoretical approaches to these systems.[9, 12, 1, 3, 39, 42, 43] Experimental difficulties include a lack of quantum state preparation and readout techniques, while theoretical difficulties appear when treating dynamics dominated by the long range interaction between ions and molecules. Recently, several groups have employed cold ($\approx mK$) and fully-controlled laser-cooled trapped ions to address these experimental issues. For instance, isotope selectivity was probed in the reaction of laser-cooled Mg^+ with HD, and the formation rate of MgD^+ was found to be 5 times greater than MgH^+ . This observation was ascribed to a dynamic mechanism in the exit channel of the reaction since statistical methods predict only a factor of approximately 2.[11] A similar experimental technique was applied to $Ca^+ + HD$ reactions as well,[17] where the CaD^+ channel was found to have 1.5 times higher population than the CaH^+ channel; no detailed theoretical calculations have been performed for this system. With the help of laser-cooled ions, the initial quantum states are experimentally well controlled, but highly accurate PESs are still challenging to calculate with Mg^+ or Ca^+ ions due to the complexity of their electronic structures. The development of a more comprehensive understanding of ion–molecule reactions at low temperature will benefit from studies with less complex species that are amenable to theoretical treatment.

We build off the work done on the $Be^+ + H_2O$ reaction, which showed that dynamics resulting from a submerged barrier strongly affects the reaction, leading to a reduction of

the overall reaction rate from the ADO capture limit. The overestimation by the capture model was thus taken as a sign that this reaction is not completely statistical, despite the existence of a deep BeH_2O^+ potential well along the reaction path. In this work, we probe the dynamics by examining the product branching ratio, which is presumably controlled by the exit channel barriers. Such a measurement is much more sensitive to the determination of the overall rates.

6.3 Experimental

Similar to the $\text{Be}^+ + \text{H}_2\text{O}$ work, we load Be^+ into the trap and laser cool it to create Coulomb crystals. A combination of $\text{H}_2\text{O}/\text{HOD}/\text{D}_2\text{O}$ is introduced into the chamber via leak valve, where the reaction products are detected via the TOF. To produce HOD, we mix H_2O and D_2O .[?, ?] We mix "equal" amounts of H_2O and D_2O and leave it overnight to produce roughly 1:2:1 ratio of $\text{H}_2\text{O}:\text{HOD}:\text{D}_2\text{O}$ as roughly verified by the RGA. We measure these fractions of deuterations via the RGA. A typical scan reveals water fractionation products at $m/z = 18, 17$, and 16 , which coincide with H_2O^+ , OH^+ , and O^+ . The fractionation ratios of water are found by solving the system of equations:

$$P_{\text{H}_2\text{O}} = R_{18} + R_{17} + R_{16} \quad (6.1)$$

$$R_{18} = \alpha P_{\text{H}_2\text{O}} \quad (6.2)$$

$$R_{17} = \beta P_{\text{H}_2\text{O}} \quad (6.3)$$

$$R_{16} = \gamma P_{\text{H}_2\text{O}} \quad (6.4)$$

where R_i is the pressure reading from the RGA and $P_{\text{H}_2\text{O}}$ is the true H_2O pressure. These fragmentation ratios were found to be $\alpha = 0.768 \pm 0.006$, $\beta = 0.184 \pm 0.006$ and $\gamma = 0.068 \pm 0.002$. The direct readings from analog scans with deuterated samples were then adjusted to account for the fractionation for each isotopologue.

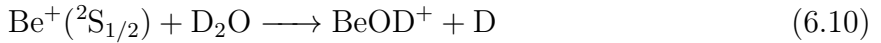
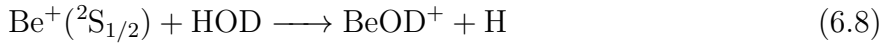
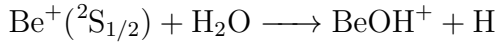
$$P_{\text{H}_2\text{O}} = \frac{1}{\alpha} \left(R_{18} - \frac{\beta}{\alpha} R_{20} - \frac{\beta}{2\alpha} R_{19} \right) \quad (6.5)$$

$$P_{\text{HOD}} = \frac{R_{19}}{\alpha} \quad (6.6)$$

$$P_{\text{D}_2\text{O}} = \frac{R_{20}}{\alpha} \quad (6.7)$$

6.4 Results and Discussion

Because the HOD sample also contains both H_2O and D_2O , the product BeOH^+ ($m/z = 26$) has contributions of the reaction of the cation with H_2O , while BeOD^+ ($m/z = 27$) has contributions from reactions with D_2O . The reactions of interest are:



Thus, the differential forms and solutions of the reagents and products are solved and shown in C.3. The branching ratio $\eta \equiv k_{\text{BeOD}^+}/(k_{\text{BeOD}^+} + k_{\text{BeOH}^+})$ is the fraction of BeOD^+ produced from reactions (6.8) where k_j is the rate coefficient of species j . Solutions to the rate equations C.13, C.14, and C.17 are parameterized by the density measurements of the water isotopologues taken from a RGA, and a least-squares fit is taken over data sets of integrated TOF mass spectra with shared fitting parameters k_1 , k_2 , k_3 , and η . In order to extract the pure $\text{Be}^+(\text{S}_{1/2})$ and $\text{Be}^+(\text{P}_{3/2})$ -state branching ratios, the process shown in Figure 6.1(A)–(C) was repeated at different P-state fractions. The results are shown in Fig. 1(D) along with a least-squares linear-fit (blue line). The vertical intercept of this fit gives $\eta_S = 0.56 \pm 0.03$ for the ground $\text{Be}^+(\text{S}_{1/2})$ state reaction, while no conclusive dependence on P-state fractions is found within the confidence intervals. To further verify that our measurement is independent of reagent ratios, we repeated the measurement for different mixtures of HOD, H_2O , and D_2O , as shown in Fig. 3. The branching ratio of $\text{BeOD}^+ + \text{H}$ in reaction $\text{Be}^+ + \text{HOD}$ (with 2% $\text{Be}^+(\text{P}_{3/2})$ state population) is consistent over different hydrogen fractions in the gas. The fraction of hydrogen atoms in the chamber (ξ) from all

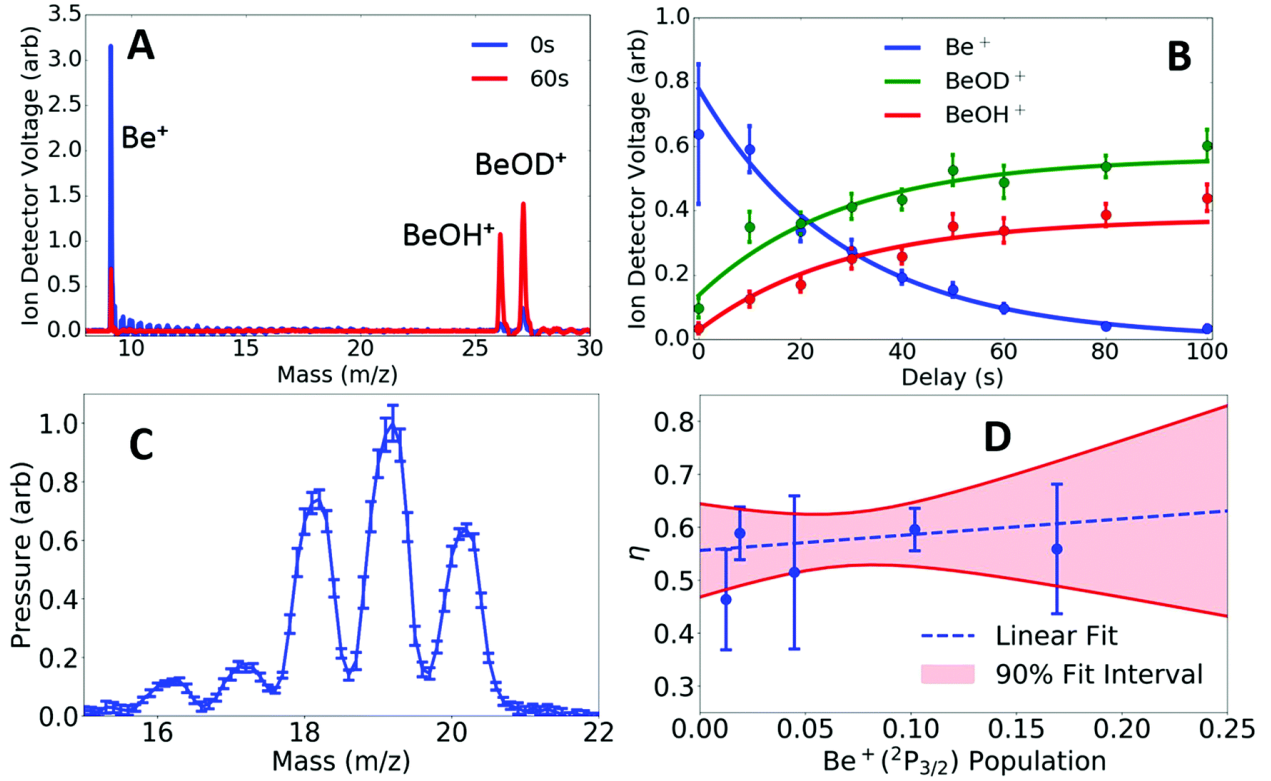


Figure 6.1: (A) A typical TOF signal (5 sample average) at reaction time $t = 0$ s and 60 s with $P_{\text{P}} \approx 2\%$. (B) The temporal evolution of Be^+ , BeOH^+ , and BeOD^+ in the trap as a function of reaction time, as well as the solutions of differential equations fitted to the kinetics data with $P_{\text{P}} \approx 2\%$. (C) The RGA signal (8 traces average) gives relative initial H_2O , HOD , D_2O sample ratio, which is $\rho_1 : \rho_2 : \rho_3 = (1.00 \pm 0.02) : (2.45 \pm 0.05) : (1.58 \pm 0.02)$. (D) The product fraction for BeOD^+ production (η) of reactions (6.8 and 6.9) as a function of $\text{Be}^+(^2\text{P}_{3/2})$ state population. The S-state branching ratio is found to be $\eta_s = 0.56 \pm 0.03$, in agreement with the following calculated combined value with different initial H fractions.

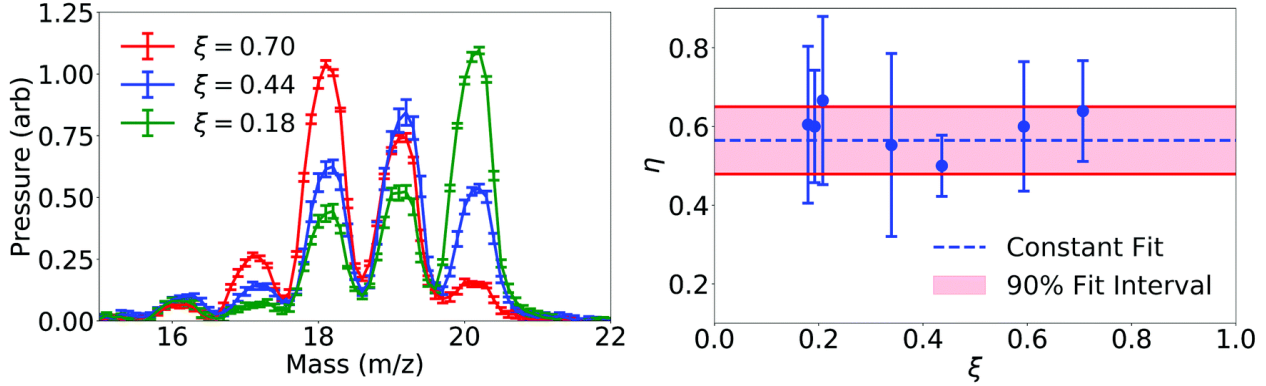


Figure 6.2: (left) Averaged (8 traces) RGA analog scan showing peaks at each isotopologue m/z . Points around the peak of each isotopologue were averaged for a more accurate partial pressure. (right) The branching ratio η of the reaction $\text{Be}^+ + \text{HOD}$ into $\text{BeOD}^+ + \text{H}$ (with a Be^+ P-state fraction of $P_P \approx 2\%$) as a function of initial H fraction in an $\text{HOD}, \text{H}_2\text{O}, \text{D}_2\text{O}$ mixture. Shared fitting the branching ratio η with a constant value fit is shown with a weighted average of $\eta = 0.58 \pm 0.14$.

water isotopologues is defined by:

$$\xi = \frac{2\rho_{\text{H}_2\text{O}} + \rho_{\text{HOD}}}{\rho_{\text{H}_2\text{O}} + \rho_{\text{HOD}} + \rho_{\text{D}_2\text{O}}} \quad (6.11)$$

Weighted averaging of the fitted values over different mixtures then gives $\eta = 0.58 \pm 0.14$, $k_2/k_1 = 0.8 \pm 0.9$, $k_3/k_1 = 0.8 \pm 0.9$. Despite the large error bars on the relative rate coefficients, due to the significant covariance of the rate coefficients, η is reasonably well determined. To further check our measurement of η , the process was repeated for shared fits with identical rate coefficients ($k_1 = k_2 = k_3$) yielding $\eta = 0.57 \pm 0.07$. The calculated overall rate coefficients of the $\text{Be}^+ + \text{D}_2\text{O}$ and $\text{Be}^+ + \text{HOD}$ reactions are $(2.29 \pm 0.05) \times 10^{-9} \text{ cm}^3 \text{ molecule}^{-1} \text{ s}^{-1}$ and $(2.29 \pm 0.05) \times 10^{-9} \text{ cm}^3 \text{ molecule}^{-1} \text{ s}^{-1}$, respectively, which are slightly larger than that $((2.02 \pm 0.04) \times 10^{-9} \text{ cm}^3 \text{ molecule}^{-1} \text{ s}^{-1})/25$ of the $\text{Be}^+ + \text{H}_2\text{O}$ reaction. The calculated k_2/k_1 and k_3/k_1 ratios are 1.13 ± 0.04 and 1.13 ± 0.04 , which are consistent with experimental values of 0.8 ± 0.9 and 0.8 ± 0.9 , respectively. The identical k_2/k_1 and k_3/k_1 ratios suggests the negligible isotopic effect in the thermal reaction probabilities of the

$\text{Be}^+ + \text{D}_2\text{O}$ and $\text{Be}^+ + \text{HOD}$ reactions. The branching ratio was determined using the QCT method for the $\text{Be}^+ + \text{HOD}$ reaction. Specifically, the calculated branching fraction of $\text{Be}^+ + \text{HOD}$ (η) is 0.61 ± 0.02 , which is in good agreement with experimental value 0.58 ± 0.14 . The branching ratio of the two products (BeOD^+ and BeOH^+) can be understood in terms of the PST model, which assumes complete energy randomization in the deep intermediate (BeHOD^+) well. In Fig. 4, the branching fraction for the $\text{BeOD}^+ + \text{H}$ channel is plotted as a function of the collision energy, which shows very weak temperature dependence. At the specific collisional temperature 100 K, the fraction obtained by integrating the energy dependent branching ratio with a Boltzmann weight is 0.67, which is in reasonable agreement with the QCT results provided by Hua Guo.[?]

6.4.1 Conclusion

To summarize, chemical reactions between $\text{Be}^+(^2\text{S}_{1/2})$ and HOD have been investigated using an integrated ion trap and highresolution TOF-MS and ZPE corrected QCT calculations on an accurate global PES. Two product channels have been observed and the branching to $\text{BeOD}^+ + \text{H}$ is accurately determined to be 0.58 ± 0.14 . The experimental result is in good agreement with ZPE corrected QCT calculation result (0.61 ± 0.02) as well as close to the statistical PST model (0.67), which reveals that the branching to the two product channels is largely due to the availability of different open states in each channel. Since their rate coefficients deviate from the capture limit as reported in our earlier work, it is clear that the $\text{Be}^+(^2\text{S}_{1/2}) + \text{H}_2\text{O}/\text{D}_2\text{O}/\text{HOD}$ reactions have a non-negligible non-statistical component.

CHAPTER 7

Low Temperature C⁺ + H₂O

7.1 Introduction

The interstellar medium (ISM) is defined as the matter and radiation that exists between star systems and galaxies, the aggregated gasses form clouds with varying densities and sizes. At high enough densities/sizes, these clouds attenuate the oncoming radiation from nearby light sources to where it may become opaque as viewed from the opposite side. These dark/dense clouds then have regions ranging from 1000's of Kelvin to 10's of Kelvin where the hottest regions are being bombarded by UV radiation consisting of almost exclusively ions H⁺, C⁺, etc. (HII regions), while the coldest regions are deeper within and predominately populated by neutral molecules (molecular cloud).

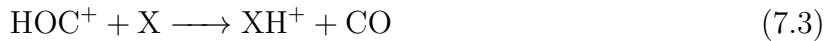
In between these extremes, we have a mixing of both ions and molecules at low temperatures ranging from 10 K to 100 K. In this regime, with an abundance of both ions and molecules, the reactions with ion-dipole interactions will dominate, as the rate constant increases as temperature decreases, unlike neutral-neutral and ion-induced dipole reactions. Within these clouds, one of the most prevalent molecular ions observed is that of the formyl group (or aldehyde group) HCO⁺ and its isomer HOCH⁺, represented together as [HCO]⁺. These isomers have been observed in diffuse clouds with ratios (HCO⁺:HOCH⁺) ranging from $\approx 100 : 1$ to $> 12000 : 1$. These discrepancies may arise due to the dominant avenues in which the formyl isomers can be produced, isomerization with H₂ molecules, etc. One of the reaction networks that produce the isomers is of particular interest, C⁺ + H₂O.





Where the branching ratio of interest is defined to be the percentage HOC^+ production to that of HCO^+ , $\text{HOC}^+:\text{HCO}^+$. This ratio has been experimentally found to be 86:14 at room temperature[13], but unknown at temperatures relevant to the ISM, where these kind of ion-dipole reactions would dominate.

By definition, these formyl isomers of reactions eqs. (7.1) and (7.2) have identical mass and thus, cannot be readily read off by the TOF system. To be able to separate the isomer products, we need to be able to separate their masses. By introducing a gas into the system with a proton affinity in between the isomer products, we may selectively react only the less stable HOC^+ isomer. This also yields a distinct m/z peaks originating from separate isomers as seen in reactions 7.3 and 7.5. But by using an external gas, we are doing an indirect measurement, and as such, it may add unintended complications. Certain gasses are more reactive and may react with the excited Be^+ , C^+ , or any other ionized species in the trap. Another possibility is that the HOC^+ may isomerize due to interactions with the gas as shown in reaction 7.4.[13]



	Affinity (kJ/mol)	Affinities (eV)
O ₂	422	18.3
H ₂	424	18.4
Kr	425	18.4
CO*	427	18.5
Kr	425	18.4
HF	490	21.2
N ₂	495	21.5
Xe	496	21.5
NO	531	23.0
CO ₂	548	23.8
CH ₄	552	23.9
HCl	564	24.5
HBr	569	24.7
N ₂ O	571	24.8
*CO	594	25.8

Table 7.1: Proton affinities of gasses between formyl isomers where (*) indicates H bonding location.

7.2 Experimental

7.2.1 Secondary Reactions

As mentioned in previous sections, our ion trap continually holds the ions initially loaded, as well as the subsequent charged reaction products (within the trappable mass range). This feature (bug) is of particular importance for us, as we cannot directly read off the ratio of the isomers and will need to contend with the possibility that the two isomers will continually

react with H₂O at different rates:



Theoretically, the differing dipole moments of the isomers would produce different dipole-dipole interactions with H₂O. Literature shows that averaged dipole moments for HCO⁺ and HOC⁺ are 4.6 D and 2.4 D, respectively.[?] But these contribute the a dipole dipole rate constant contribution, which is very short ranged ($1/r^6$) and do not contribute much to the overall rate constant.

We cannot deterministically measure the rate of reaction 7.7 because there is not a way to produce only HOC⁺, but we may produce only HCO⁺. Considering reactions 7.4 and 7.3, if we let X = CO, we find that both reactions can only yield HCO⁺, allowing us to deterministically produce one of the isomers:



By producing only HCO⁺, we directly observe reaction 7.6 with a multi-step reaction procedure. With loaded Be⁺ and C⁺, the trap is exposed to H₂O from the CBGB, to produce a combination of the isomers [HCO]⁺, all the while, CO is introduced via the leak valve in the differential cross region to a pressure of $\approx 4 \times 10^{-9}$ Torr as measured in the trap chamber. The constant introduction of CO ensures full conversion of HOC⁺ \longrightarrow HCO⁺ at a rate $\approx \times 10$ faster than that of reactions 7.1 and 7.2 ensuring we are seeing the time evolution of reaction 7.6 as seen in Figure 7.1b). A similar procedure of continuously exposing the trap to the CBGB without CO yields a combination of the rates of reactions 7.6 and 7.7 seen in Figure 7.1a).

The rates of reactions 7.1, 7.6, and a combination of reactions 7.6+7.7 are found with least-squares fitting of the solutions to differential equations found in section C.4. Beam densities are determined for each run individually by considering the Be⁺ + H₂O reaction complex as outlined in Section 3.2.2.

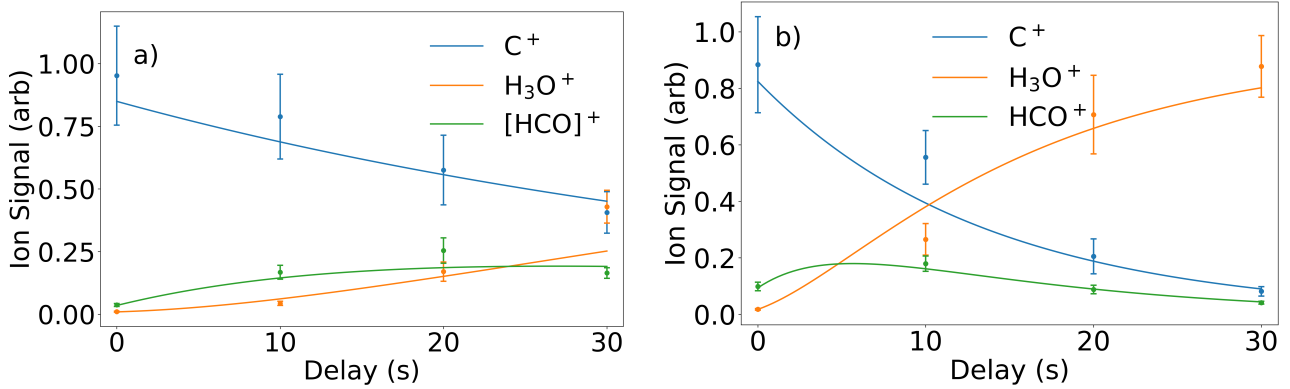


Figure 7.1: Time evolution of C^+ and H_2O introduced via CBGB as well as subsequent reaction products. a) TOF traces without flooding of CO where fitted rate constants are found to be $k_{7.1} + k_{7.2} = (7.7 \pm 0.6) \times 10^{-9} \text{ cm}^3/\text{s}$, and $k_{7.6} = (1.7 \pm 0.2) \times 10^{-8} \text{ cm}^3/\text{s}$. b) TOF traces with flooding of CO where fitted rate constants are found to be $k_{7.1} + k_{7.2} = (7.9 \pm 0.6) \times 10^{-9} \text{ cm}^3/\text{s}$, and $k_{7.9} = (1.7 \pm 0.2) \times 10^{-8} \text{ cm}^3/\text{s}$.

Although we cannot make a statement about the rate of reaction 7.7, we see that at whatever ratio the isomers are produced, we cannot experimentally observe any meaningful deviation between the pure $\text{HCO}^+ + \text{H}_2\text{O}$ and $[\text{HCO}]^+ + \text{H}_2\text{O}$. Thus, we find it reasonable to combine reactions 7.6 and 7.7 into:



Where $[\text{HCO}]^+$ is used to represent both isomers. With this understanding, we may take the ratio of isomers at $m/z = 29$ to be constant with respect to time exposed to the beam.

7.2.2 Internal Relaxation

Through the $\text{C}^+ + \text{H}_2\text{O}$ reaction, 3.34 eV of energy is released in the production of HOC^+ , while an even greater 5.05 eV for HCO^+ . The released energy has two avenues, the kinetic energy of the reaction products of $[\text{HCO}]^+$ and H, and the internal states of the isomer produced. If the isomer is produced in a highly excited internal state, this could cause problems for our titration process if they are long lived and high enough energy to cause the

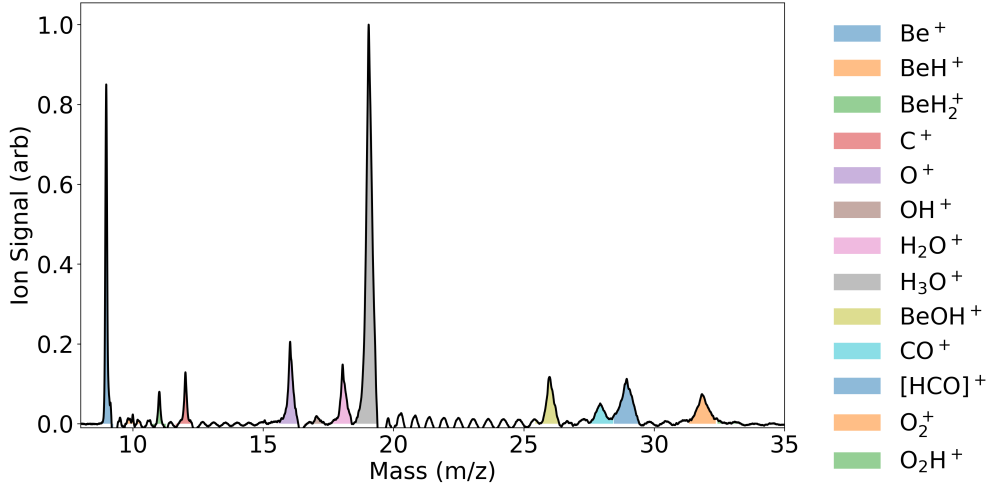


Figure 7.2: Average of 10 TOF traces showing reaction products

more stable HCO^+ to react with a titration gas X when it would not have in its internal ground state. Mauclaire et al. found that the radiative lifetimes of these states can be as high as ≈ 300 ms.^[29] At the operating pressures, we may expect

To see if these internal states may be an issue, we use O_2 as a titration gas. Table 7.1 shows that O_2 is only 0.2 eV away from being able to react with the less stable HOC^+ . By introducing H_2O via the general valve, and O_2 from a valve behind a leak valve, the two gasses can be introduced with a well defined time delay. If the literature is to be believed, a delay of 1 s between the introduction of the two gasses should be sufficient for more than 99% of the internally excited states to have radiatively decayed; otherwise we may see a proton exchange and a new peak at O_2H^+ . The procedure is performed and resulting TOF trace is shown in Figure 7.2.

There is an anomalous peaks that we do not know the origin of at $m/z = 11$, which we have denoted BeH_2^+ . Despite this, it is clear that there is no production of O_2H^+ . Given a 1 s delay between the introduction of H_2O and the titration gas, the HOC^+ isomer has internally relaxed to at least less than 0.2 eV. For HCO^+ , there is reason to believe the the relaxation rate would be even greater, as HCO^+ has a dipole moment approximately 2 times that of HOC^+ .^[?] With the titration gasses we use to separate the isomers, CO_2 and $^{15}\text{N}_2$, the HCO^+ would have to maintain an internal excited state greater than 2 eV and 4.3 eV,

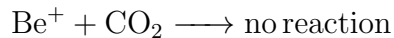
respectively, to skew the results. The lack of a proton exchange signal shows alleviates this concern.

7.2.3 Determination of Branching Ratio

Previous literature utilized gasses such as NO, CH₄, N₂O, and Kr to separate the isomers. Of those Kr, and Xe are inert and would not react with any other ions in our trap, but are too heavy to reliably hold after a reaction. Of the others, NO is caustic and will ruin the vacuum chamber if introduced, and thus was avoided. Attempts were made with N₂O and well as CH₄, but both had their own unique complications. N₂O rapidly reacts with Be⁺ and made reliable TOF traces unattainable due to the loss of the coolant ion. CH₄ readily reacted with most of the ions in the trap to produce a multitude of mass peaks, greatly complicating the analysis with secondary, tertiary, and higher order reactions. In this section, I describe the methods and results using CO₂ and ¹⁵N₂ gasses to separate the isomer mass signatures.

7.2.3.1 CO₂ Titration

From table 7.1, we see that CO₂ is a viable option to titrate the reaction products. The possible reactions of CO₂ with Be⁺ are unknown in literature, but found to be non-reactive in both ground and excited states, while C⁺ readily reacts.



Being non-reactive with Be⁺ while having a product mass that is still within our trappable range makes CO₂ an attractive option. Its reactivity with C⁺ is not a detriment, instead it is helpful as a marker for if the C⁺ has been depleted, all the HOC⁺ should also have

reacted away. We find that there are unexplained peaks that arise, but we can account for their inclusion in our data analysis.

Be⁺ + CO₂ Introducing the CO₂ into the ion chamber to react with only laser cooled Be⁺, The TOF only shows that there are trace amounts of H₂O in the chamber, with no indication of any further loss due to the inclusion of CO₂.

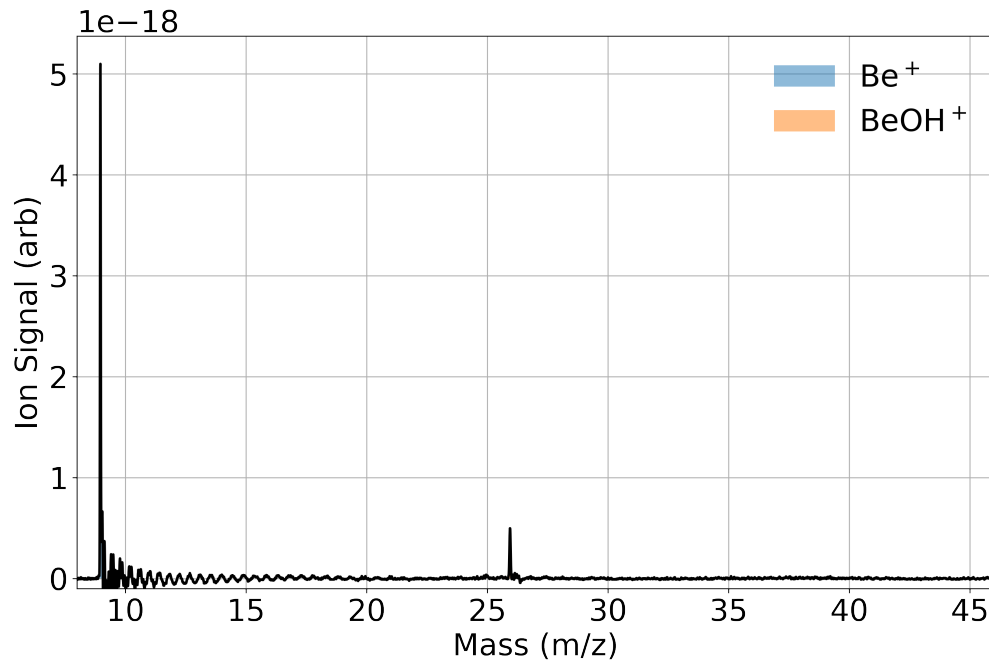


Figure 7.3: TOF trace of laser-cooled Be⁺ reacting with $\approx 1 \times 10^{-8}$ Torr CO₂ introduced via leak valve for 50 seconds.

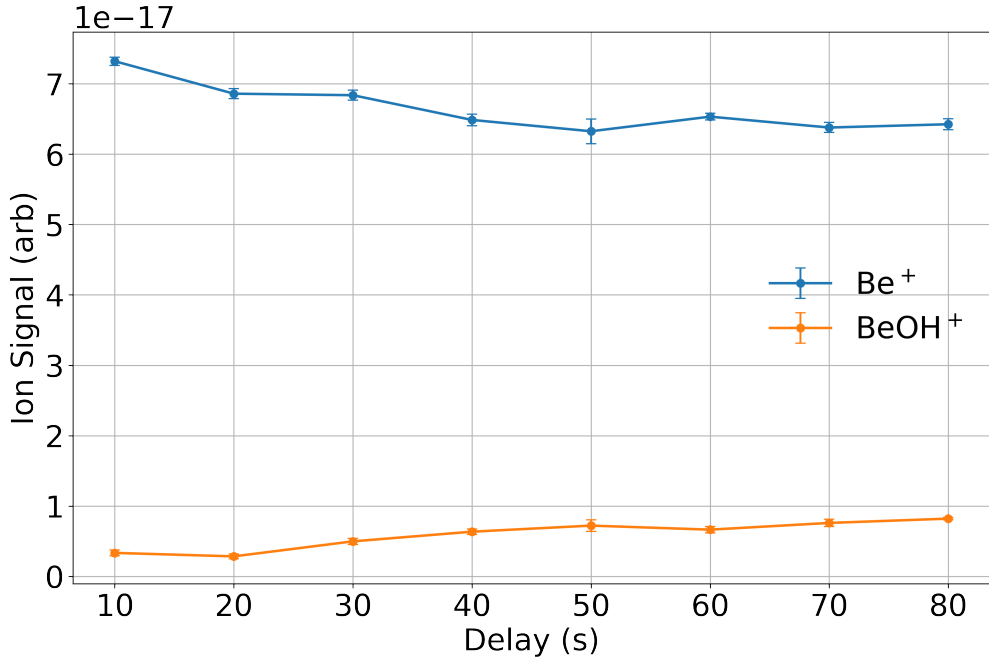


Figure 7.4: Integrated ion signal of individual TOF traces normalized by Be^+ fluorescence at various CO_2 exposure times.

We see that there aren't any reactions happening between Be^+ and CO_2 , while there is a little bit of water in the leak valve, which was baked afterwards. This does indicate that there are also no reactions between BeOH^+ and CO_2 .

C⁺ + CO₂ By ablating both C⁺ and Be⁺ into the trap and introducing CO₂ via the leak valve, we find the expected reactions 7.10, 7.11, and 7.12 as well as unexpected peaks appearing at $m/z = 15, 29$, and 45 .

Labels in Figures 7.2.3.1 and 7.2.3.1 are of predicted chemicals coinciding with the masses. The initial guess is that there is H₂O in the leak valve, as we saw it before in the $\text{Be}^+ + \text{CO}_2$ reaction, but the leak valve region was baked since that data was taken. Similarly, if there was water, we would see a peak at $m/z = 26$, coinciding with BeOH^+ , which we do not see, we should also expect to see an abundance of H₃O⁺ due to reactions between the alleged [HCO]⁺ and CO₂H⁺, which we also do not see. But, the peak at 45 could possibly be explained by H₂O in reaction 7.14, while 29 could be due to reactions 7.2 and 7.1. But

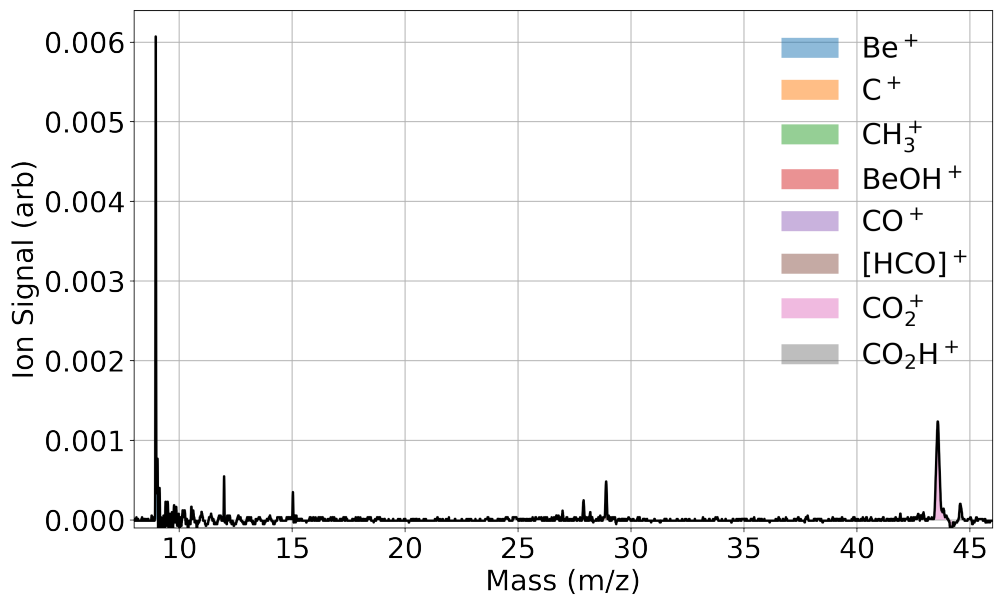


Figure 7.5: TOF trace of laser-cooled Be^+ and C^+ reacting with $\approx 1 \times 10^{-8}$ Torr CO_2 introduced via leak valve for 40 seconds.

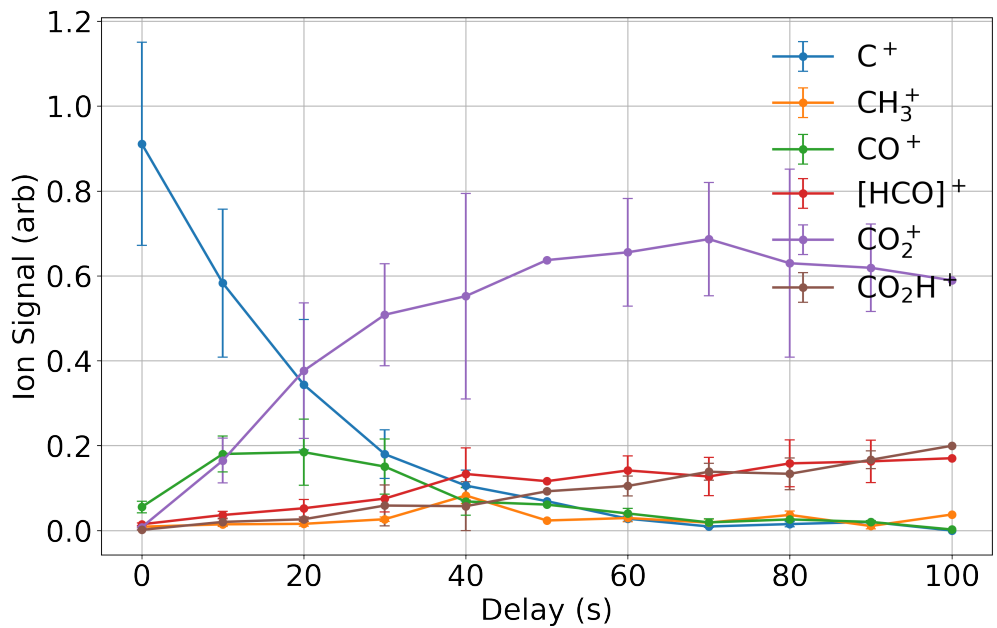


Figure 7.6: Integrated ion signal of individual TOF traces normalized by total ion signal excluding Be^+ at various CO_2 exposure times.

there are no reactions with H_2O for the production of 15.



I still doubt that the 29 mass is due to C^+ directly reacting with H_2O because the traces clearly show it increasing despite the depletion of C^+ , indicating it is a second order reaction. It wouldn't be H_2 either, because we would see BeH^+ in the trap, as well as many other peaks associated with $\text{C}^+ + \text{H}_2$ including 14, 16, and 17.

Be⁺ + C⁺ + H₂O with CO₂ Water is introduced into the chamber via the CBGB with the cell held at a temperature of 20K. After (10 ± 1) seconds of exposure, the gate valve is closed and CO₂ is leaked in to react away the formyl isomers such that $\approx 99\%$ are reacted away (determined by the disappearance of C⁺).

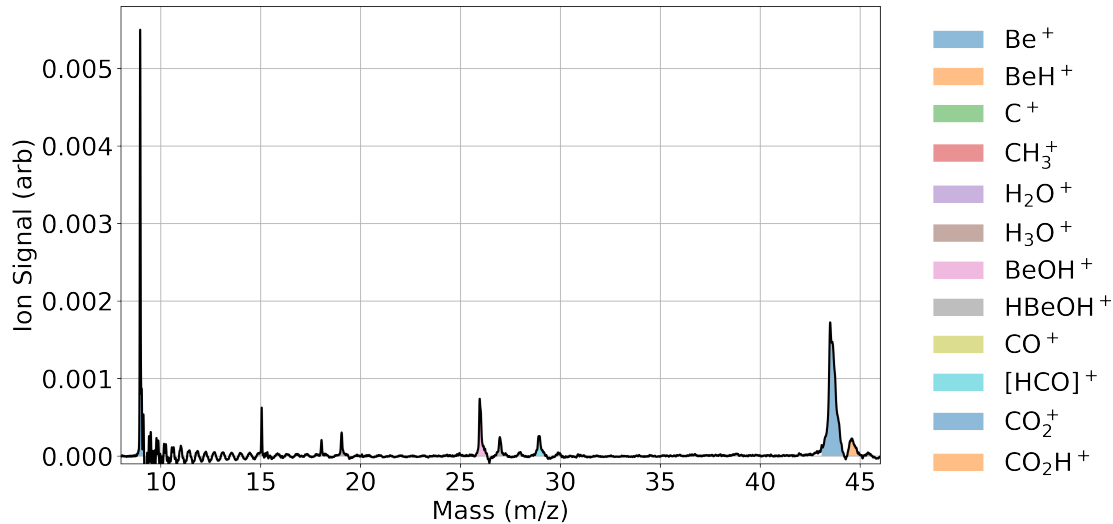


Figure 7.7: C⁺ and Be⁺ loaded into the trap is reacted with H₂O introduced from the beam. The gate valve is closed after 10 seconds and CO₂ is introduced via leak valve so that the HOC⁺ is titrated into CO₂H⁺.

Knowing the anomalous peaks in the previous tests, the peaks of interest are not exclu-

sively the branching ratio between the formyl isomers, where we define γ as the fraction of products that produce HOC^+ . By taking the solutions to the differential equations for the $\text{C}^+ + \text{H}_2\text{O}$ reaction network in Section C.4, we define the ratio of the formyl isomers and remaining C^+ .

$$\alpha(t) \equiv \frac{[\text{HCO}](t)}{[\text{HCO}](t) + \text{C}(t)} \quad (7.16)$$

In the data taken, we introduced the water in the beam for approximately 10s, the fraction of C^+ that has turned into $[\text{HCO}]^+$ is thus $\alpha = 0.37 \pm 0.02$. Considering that after titration with CO_2 , the fraction of the remaining 63% of C^+ has turned into equal amounts of $m/z = 29, 45$ defined as $\beta = 0.17 \pm 0.02$.

$$N_C(0) = N_0$$

$$N_C(\tau_1) = (1 - \alpha(\tau_1))N_0$$

$$N_{29}(\tau_1) = \alpha(\tau_1)N_0$$

Where $N_C(t)$ is the amount of C^+ is in the trap after being exposed to either the water beam or CO_2 for time t . τ_1 is the amount of time where the ions are exposed to the water beam, where α is the proportion of C^+ that is converted to $m/z = 29$, which in our case is 0.37. We then introduce the CO_2 into the system and yield:

$$\begin{aligned} N_C(\tau_1 + \tau_2) &= 0 \\ N_{29}(\tau_1 + \tau_2) &= N_{29}(\tau_1)(1 - \gamma) + N_C(\tau_1)\beta \\ &= N_0(\alpha(1 - \gamma) + \beta(1 - \alpha)) \\ N_{45}(\tau_1 + \tau_2) &= N_{29}(\tau_1)\gamma + N_C(\tau_1)\beta \\ &= N_0(\alpha\gamma + \beta(1 - \alpha)) \end{aligned}$$

The directly measured ratio $\eta \equiv \frac{\text{CO}_2\text{H}^+}{\text{CO}_2\text{H}^+ + \text{HCO}^+} = 0.55 \pm 0.02$, is equated to the combination of the possible sources of competing mass peaks:

$$\eta = 0.55 = \frac{N_{45}(\tau_1 + \tau_2)}{N_{29}(\tau_1 + \tau_2) + N_{45}(\tau_1 + \tau_2)} \quad (7.17)$$

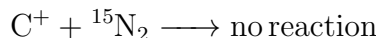
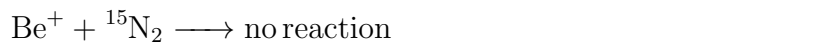
To find the branching ratio of the HOC^+ channel, we solve for γ :

$$\begin{aligned}\eta &= \frac{\beta - \alpha\beta + \alpha\gamma}{\alpha + 2\beta - 2\alpha\beta} \\ \gamma &= \frac{1}{\alpha}(\alpha\eta + \beta(\alpha + 2\eta - 2\alpha\eta - 1))\end{aligned}\quad (7.18)$$

Using equation 7.18, we find at the true branching ratio is scaled from 0.55 ± 0.03 to 0.58 ± 0.05 . The error bars are fairly large on this measurement due to the unknown species contributing to our direct ratio measurement.

7.2.3.2 $^{15}\text{N}_2$ Titration

Normally N_2 would not be a good choice, due to the fact that N_2H^+ has the same mass as the formyl isomers at $m/z = 29$, but we may instead introduce $^{15}\text{N}_2$ to produce a new peak at $m/z = 31$. We do not expect and do not see any reaction between the initially loaded ions of Be^+ and C^+ making this the ideal candidate for titration. But according to section 7.1, we should still have a separation of the isomers, thus:



To verify reaction 7.8, trapped Be^+ and C^+ ions are exposed to the water from the CBGB at a density of $4.3 \times 10^6 \text{ cm}^{-3}$ while simultaneously flooded with $\approx 3 \times 10^7 \text{ cm}^{-3}$ of CO from the leak valve connected to the differential pumping region such that $k_{7.8} \gg k_{7.1,7.2}$. After 10 s, the gate valve between the differential pumping and experimental ion chamber regions is manually closed, after which, 10^9 cm^{-3} of $^{15}\text{N}_2$ is introduced for 10 s. A TOF trace for this procedure is shown in figure 7.8.

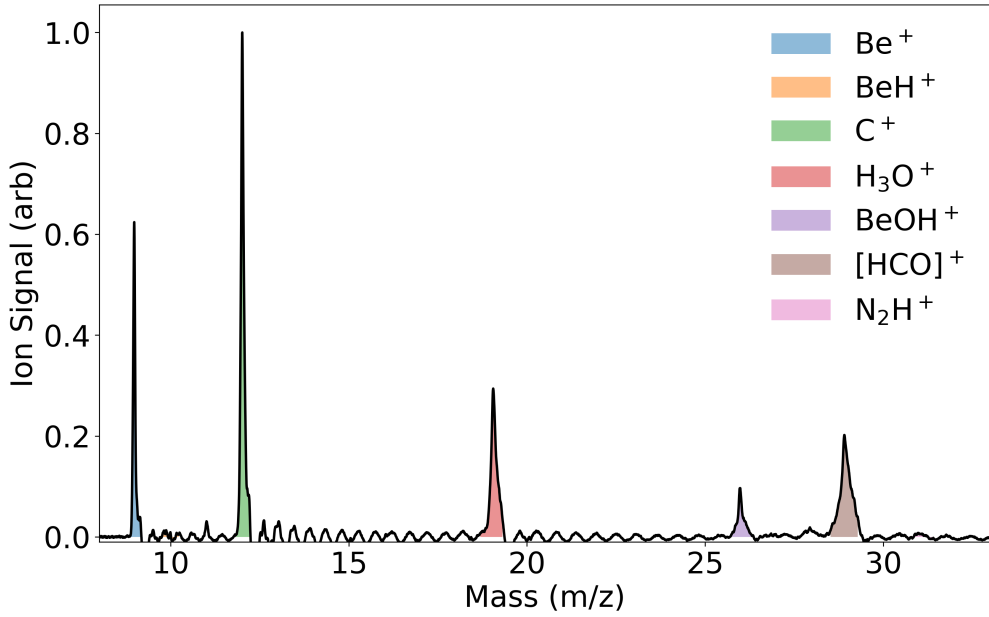


Figure 7.8: TOF trace of reaction products of Be^+ and C^+ after exposure to both water from the CBGB beam, and CO (10 s) before titration with $^{15}\text{N}_2$ (10 s). There is a distinct lack of N_2H^+ , indicating full conversion of $\text{HOC}^+ \longrightarrow \text{HCO}^+$.

Integrated N_2H^+ signal was found to be below the threshold for null signal demonstrating both points that reaction 7.8 proceeds as expected, as well as experimental verification that reaction 7.19 does not occur.

At room temperatures, the branching ratio has been found to be approximately 84:16 ($\text{COH}^+:\text{HCO}^+$)[14], but unexplored at lower regimes.

To determine the branching ratio, Be^+ and C^+ in the trap are exposed to the CBGB for 10 s, after which, the gate valve connecting the differential pumping region and ion trap chamber is closed. $^{15}\text{N}_2$ is then introduced via leak valve to react with the HOC^+ . Only runs taken at delay times of 10 s were taken, as we only concern ourselves with a ratio of signals. Repeating this process over various densities of $^{15}\text{N}_2$ allows us to determine the isomer branching ratio. We expect the ratio of N_2H^+ and $[\text{HCO}]^+$ to follow the form:

$$\frac{^{15}\text{N}_2\text{H}^+(t)}{^{15}\text{N}_2\text{H}^+(t) + [\text{HCO}]^+(t)} = C(1 - e^{-k_{7.3}\rho t}) \quad (7.21)$$

A fit performed on the data over various densities yields a rate constant of $k_{7.3} = ((6.6 \pm 1.0) \times 10^{-10}) \text{ cm}^3/\text{s}$, and a final branching ratio of $\text{HOC}^+ : \text{HCO}^+ = 0.58 \pm 0.01$, in good agreement with the CO_2 titration results.

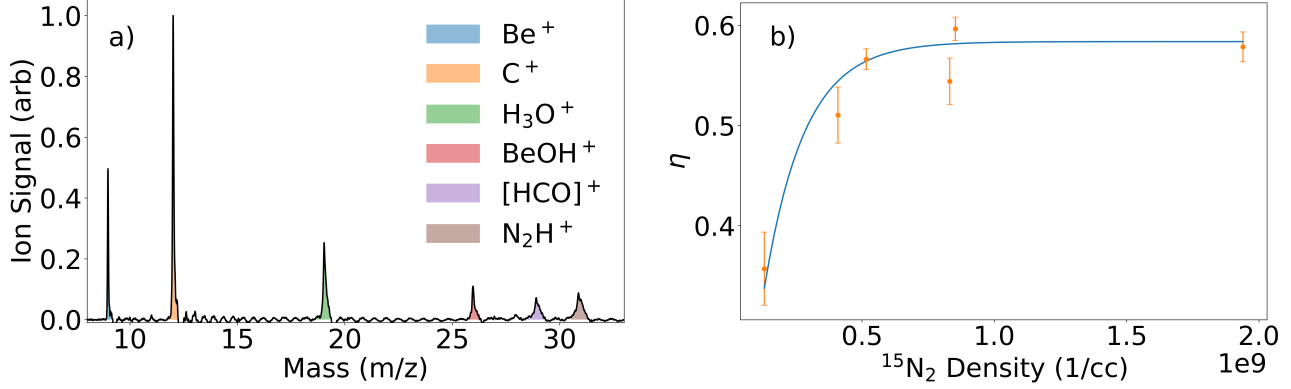


Figure 7.9: a) Average of 10 TOF traces of Be^+ and C^+ exposed to water from the CBGB (10 s), then exposed to $^{15}\text{N}_2$ from the leak valve (10 s) at a density of $1 \times 10^9 \text{ cc}^{-1}$. b) The fraction of the titrated isomers, $\eta \equiv {^{15}\text{N}_2\text{H}^+}/{({^{15}\text{N}_2\text{H}^+ + [\text{HCO}]^+})}$, as a function of $^{15}\text{N}_2$ density. Fitted parameters yield values $C = 0.58 \pm 0.01$, $k_{7.3} = ((6.6 \pm 1.0) \times 10^{-10}) \text{ cm}^3/\text{s}$.

To estimate a limit on the isomerization, we consider the above reactions 7.4 and 7.3, where $\text{X} = {^{15}\text{N}_2}$ in the context that we can only determine the abundance of $[\text{HCO}]^+$ and $^{15}\text{N}_2\text{H}^+$. As a function of pressure, we cannot see reaction 7.4, but if it does contribute, we should see a discrepancy in the total rate constant, which we estimate to be Langevin: $k_L = 8.0 \times 10^{-10}$. This gives us a possible isomerization rate of 22%, which then yield a branching ratio of 70:30.

7.3 Conclusion

Our experimental results yield directly measured branching ratios $(58 \pm 5) : (42 \pm 5)$ and $(58 \pm 1) : (42 \pm 1)$ via titration with CO_2 and $^{15}\text{N}_2$, in good agreement with one another. As the results from the $^{15}\text{N}_2$ titration were without unknown peaks, we take that to be the proper experimental result. Hua Guo provided theoretical support in performing QCT

calculations on the $\text{C}^+ + \text{H}_2\text{O}$ reaction dynamics at collision temperatures around 10 K. They find an initial branching ratio of 97:3, with 19% of their HCO^+ above the self-isomerization barrier, this brings their ratio down to 74:26. Hua also provided us with calculations on the possible percentage of isomerization due to reaction 7.4 where $\text{X} \longrightarrow {}^{15}\text{N}_2$ to be 17%, consistent with our experimental results. Adjusting our experimentally determined ratio by the possible isomerization, we yield a ratio result of $(70 \pm 1) : (30 \pm 1)$, this is much closer to the QCT results.

These results are in contrast to the room temperature result of 86:14[13], but in better agreement with phase space calculations claiming a branching ratio of 67:33 in the literature.[?]

CHAPTER 8

Conclusion and Future Outlook

The experiment has broken new ground in ion-molecule reactions at various reaction temperatures, but there is still much left unexplored. The recent inclusion of two Lioptec dye lasers will allow for probing of internal state distributions of the H₂O in the CBGB via REMPI. Further experiments may go towards the inclusion of polycyclic aromatic hydrocarbons (PAH's) in the CBGB, where the dye lasers would also be able to directly detect the production and cooling of these species within the beam.

An avenue that was discussed but not extensively explored is the possibility of looking at stereodynamics between molecules and ions with the apparatus. A key feature is that the molecules approaching the ions in the trap come in a predetermined direction, if the excited Be⁺ P-state orbital is oriented in a particular direction relative to the oncoming molecules, we may find that there is a change in reaction rates or even branching ratios.

The possibilities are endless.

APPENDIX A

Parker Pulse Valve

To reach other temperature regimes or to have precise timing control on the introduction of a gas into the chamber, we utilize a Parker Pulse Valve as seen in Figure A.1. The pulse valve requires 28 VDC to actuate the solenoid, opening the orifice. The speed at which we operate the pulse valve allows for rise times of milliseconds. During operation of the pulse valve, the PTR is cooling the CBGB components to act as cryopumping surfaces and improve the vacuum in the stem chamber. With appreciable backing pressure (≈ 1 atm), the supersonic pulse velocity is defined as:[33]

$$v_\infty = \sqrt{\frac{2k_b T_0}{m} \frac{\gamma}{\gamma - 1}}$$

Where γ is the heat capacity ratio C_p/C_v , and T_0 is the original temperature of the source.

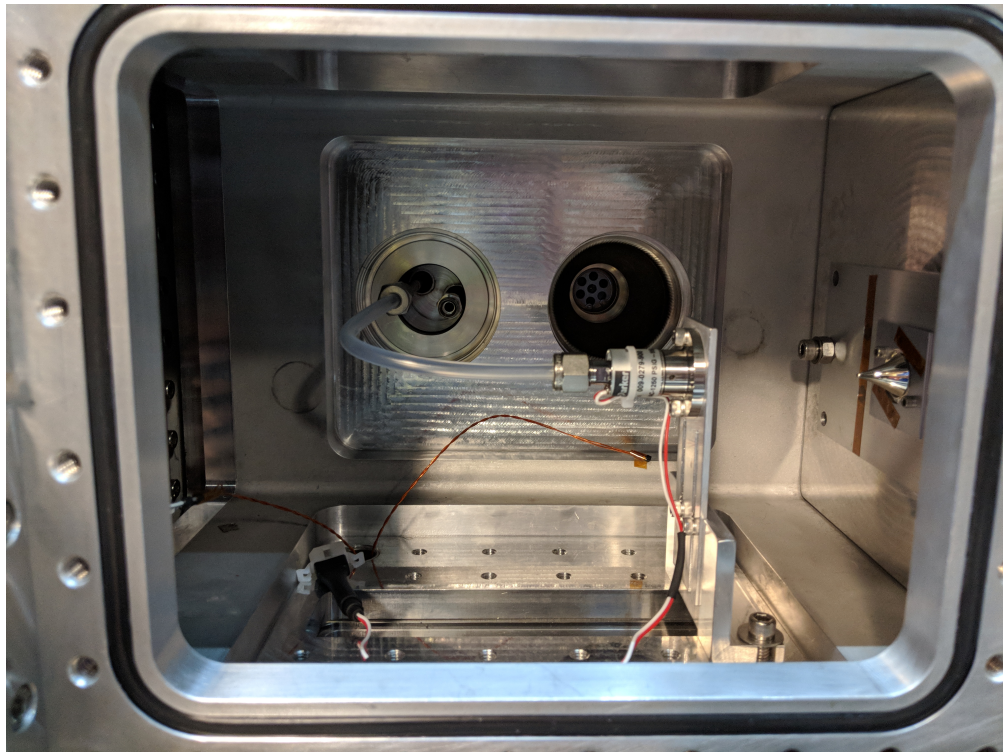


Figure A.1: Parker Pulse Valve mounted inside the stem chamber aimed at the differential pumping region. The Beam Dynamics skimmer is mounted over the back face of the stem chamber to clean up the supersonic pulse.

APPENDIX B

Pressure Calibration

To be able to calculate rate constants, we need to have an accurate measure of the absolute pressure of the gas of interest. This is easier said than done, various instruments may have different absolute readings and uncertainties and may not agree with one another *in situ*. To find the relative pressures of multiple gasses introduced into the chamber, we use the RGA, but Stanford Research Systems does not provide an uncertainty for its device's absolute accuracy. We calibrate it by cross-correlating our RGA measurements with the total pressure measured by an Agilent UHV-24 Bayard-Alpert Gauge Tube, which gives a quoted $< 10\%$ error at 5×10^{-10} Torr (our normal operating pressure). The fact that the ion gauge is set in a nipple connected to the chamber provides at least another 30% uncertainty, but is more acceptable than the completely unknown reliability of the RGA.

The calibration consists of incrementally adding either H₂ or H₂O into the chamber and read off the pressures from the RGA as well as the ion gauge (scaled by their species dependent specifications). By fitting the relationship between these two readings, we find that there is a mass dependent scaling factor for the RGA to ion gauge pressure shown in Figure B.1. H₂O is scaled by 1.1, while H₂ is much less accurate, and scaled by 0.59. Using this calibrated pressure reading, our measured Be⁺ + H₂ reaction rate coefficient of $1.2 \pm 0.3_{\text{stat}} \times 10^{-9} \text{ cm}^3/\text{s}$ agrees with the literature seen in Figure B.2.

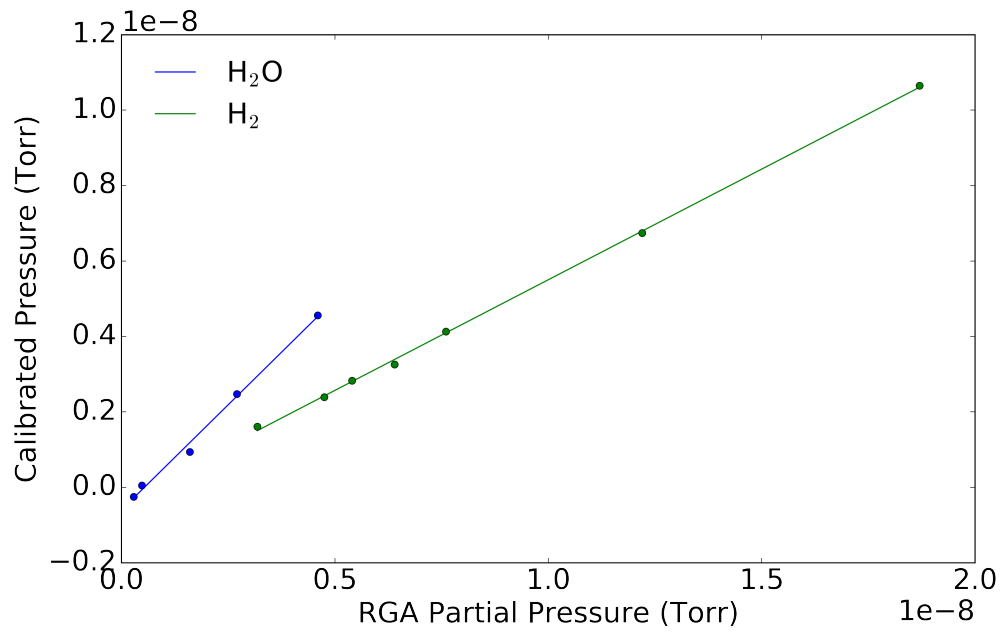


Figure B.1: Fitted curves for H_2 and H_2O detection between the ion gauge and RGA. The reported pressure between the ion gauge and RGA is nearly identical for H_2O with a slope of 1.1, but noticeably different for H_2 with a slope of 0.59.

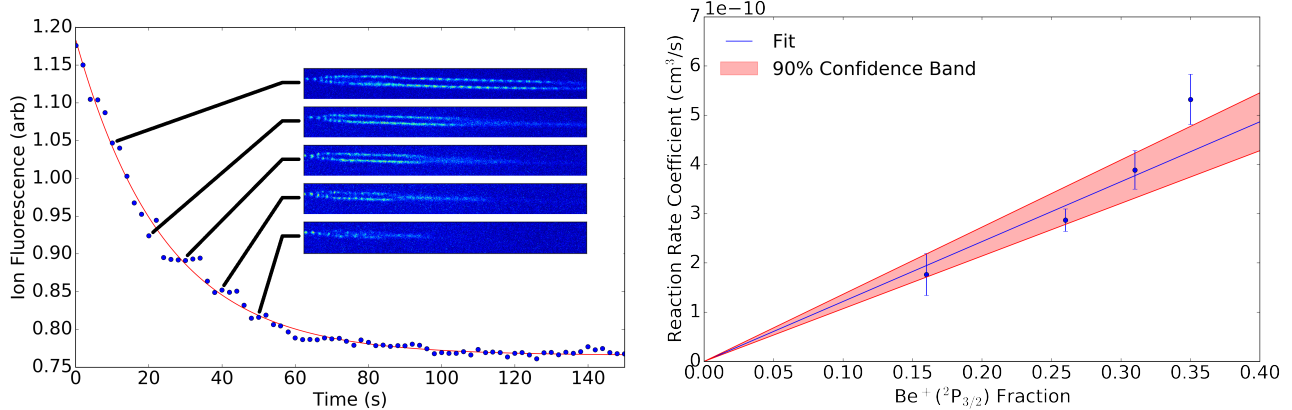


Figure B.2: (A) A typical fluorescence decay measurement of $\text{Be}^+ + \text{H}_2$. The inset images are a subset of the original ion fluorescence images recorded by the camera. The red curve is an exponential fit (with a free offset) to the data, which gives the total reaction rate. (B) A fit of $\text{Be}^+ + \text{H}_2$ fluorescence decay at various P state excitation fractions. A statistical rate coefficient for full excitation of $(1.2 \pm 0.3_{\text{state}}) \times 10^{-9} \text{ cm}^3/\text{s}$ is in agreement with existing literature.

APPENDIX C

Chemical Rate Equations

Rate equations used in the shared fitting programs.

C.1 Be⁺ + H₂O All Thermochemically Allows Channels

Differential forms for reactions:

$$\begin{aligned}
 \text{Be}(t) &= \text{Be}_0 e^{\rho t(-(k_1+k_3+k_5+k_7))} \\
 \text{BeH}(t) &= - \frac{e^{-k_6\rho t} \left(\text{Be}_0 k_5 \left(e^{\rho t(-(k_1+k_3+k_5-k_6+k_7))} - 1 \right) - \text{BeH}_0 (k_1 + k_3 + k_5 - k_6 + k_7) \right)}{k_1 + k_3 + k_5 - k_6 + k_7} \\
 \text{BeO}(t) &= - \frac{e^{-k_8\rho t} \left(\text{Be}_0 k_7 \left(e^{\rho t(-(k_1+k_3+k_5+k_7-k_8))} - 1 \right) - \text{BeO}_0 (k_1 + k_3 + k_5 + k_7 - k_8) \right)}{k_1 + k_3 + k_5 + k_7 - k_8} \\
 \text{BeOH}(t) &= \frac{1}{(k_1 + k_3 + k_5 + k_7)(k_1 + k_3 + k_5 - k_6 + k_7)(k_1 + k_3 + k_5 + k_7 - k_8)} \left[e^{\rho t(-(k_6+k_8))} \right. \\
 &\quad \left(e^{\rho t(-(k_1+k_3+k_5-k_6+k_7-k_8))} \left(\text{Be}_0 \left(k_1^3 \left(e^{\rho t(k_1+k_3+k_5+k_7)} - 1 \right) \right. \right. \right. \\
 &\quad \left. \left. \left. - k_1^2 k_5 \left(e^{\rho t(k_1+k_3+k_5-k_6+k_7)} - 3e^{\rho t(k_1+k_3+k_5+k_7)} + 2 \right) - k_1^2 k_6 e^{\rho t(k_1+k_3+k_5+k_7)} \right. \right. \\
 &\quad \left. \left. - k_1^2 k_8 e^{\rho t(k_1+k_3+k_5+k_7)} + 2k_1^2 k_3 \left(e^{\rho t(k_1+k_3+k_5+k_7)} - 1 \right) + 3k_1^2 k_7 e^{\rho t(k_1+k_3+k_5+k_7)} \right. \right. \\
 &\quad \left. \left. + k_1^2 k_6 - 2k_1^2 k_7 + k_1^2 k_8 + k_1 k_3^2 \left(e^{\rho t(k_1+k_3+k_5+k_7)} - 1 \right) \right. \right. \\
 &\quad \left. \left. + k_1 k_5^2 \left(- 2e^{\rho t(k_1+k_3+k_5-k_6+k_7)} + 3e^{\rho t(k_1+k_3+k_5+k_7)} - 1 \right) \right. \right. \\
 &\quad \left. \left. + k_1 k_5 k_8 \left(e^{\rho t(k_1+k_3+k_5-k_6+k_7)} - 2e^{\rho t(k_1+k_3+k_5+k_7)} + 1 \right) \right. \right]
 \end{aligned}$$

$$\begin{aligned}
& + k_1 k_6 k_8 e^{\rho t(k_1+k_3+k_5+k_7)} - k_7(k_1+k_3+k_5+k_7)(k_1+k_3+k_5-k_6+k_7) e^{\rho t(k_1+k_3+k_5+k_7-k_8)} \\
& - k_5(k_3+k_5+k_7)(k_3+k_5+k_7-k_8) e^{\rho t(k_1+k_3+k_5-k_6+k_7)} \\
& + (k_5+k_7)(k_3+k_5-k_6+k_7)(k_3+k_5+k_7-k_8) e^{\rho t(k_1+k_3+k_5+k_7)} \\
& - 2k_1 k_3 k_5 \left(e^{\rho t(k_1+k_3+k_5-k_6+k_7)} - 2e^{\rho t(k_1+k_3+k_5+k_7)} + 1 \right) - k_1 k_3 k_6 e^{\rho t(k_1+k_3+k_5+k_7)} \\
& - 2k_1 k_5 k_6 \left(e^{\rho t(k_1+k_3+k_5+k_7)} - 1 \right) - 2k_1 k_5 k_7 e^{\rho t(k_1+k_3+k_5-k_6+k_7)} - 2k_1 k_6 k_7 e^{\rho t(k_1+k_3+k_5+k_7)} \\
& + 3k_1 k_7^2 e^{\rho t(k_1+k_3+k_5+k_7)} - k_1 k_3 k_8 e^{\rho t(k_1+k_3+k_5+k_7)} - 2k_1 k_7 k_8 e^{\rho t(k_1+k_3+k_5+k_7)} \\
& + 4k_1 k_3 k_7 e^{\rho t(k_1+k_3+k_5+k_7)} + 6k_1 k_5 k_7 e^{\rho t(k_1+k_3+k_5+k_7)} + k_1 k_3 k_6 - 2k_1 k_3 k_7 + k_1 k_3 k_8 \\
& - 2k_1 k_5 k_7 + k_1 k_6 k_7 - k_1 k_6 k_8 - k_1 k_7^2 + 2k_1 k_7 k_8 + k_3 k_5 k_6 + k_3 k_7 k_8 + k_5^2 k_6 + k_5 k_6 k_7 - k_5 k_6 k_8 \\
& + k_5 k_7 k_8 - k_6 k_7 k_8 + k_7^2 k_8 \Big) + (k_1+k_3+k_5+k_7)(k_1+k_3+k_5-k_6+k_7) \\
& (k_1+k_3+k_5+k_7-k_8) \left((\text{BeH}_0 + \text{BeOH}_0) e^{\rho t(k_1+k_3+k_5+k_7)} - \text{BeH}_0 e^{\rho t(k_1+k_3+k_5-k_6+k_7)} \right) \Big) \\
& + \text{BeO}_0 e^{k_6 \rho t} \left(e^{k_8 \rho t} - 1 \right) (k_1+k_3+k_5+k_7)(k_1+k_3+k_5-k_6+k_7)(k_1+k_3+k_5+k_7-k_8) \Big] \\
\text{H}_2\text{O}(t) = & - \frac{e^{-k_4 \rho t} \left(\text{Be}_0 k_3 \left(e^{\rho t(-(k_1+k_3-k_4+k_5+k_7))} - 1 \right) - \text{H}_2\text{O}_0 (k_1+k_3-k_4+k_5+k_7) \right)}{k_1+k_3-k_4+k_5+k_7} \\
\text{H}_3\text{O}(t) = & \frac{1}{(k_1+k_3+k_5+k_7)(k_1+k_3-k_4+k_5+k_7)} e^{-k_4 \rho t} \left(e^{k_4 \rho t} (k_1+k_3-k_4+k_5+k_7) \right. \\
& (\text{Be}_0 k_3 + \text{H}_3\text{O}_0 (k_1+k_3+k_5+k_7)) + \text{Be}_0 k_3 k_4 e^{\rho t(-(k_1+k_3-k_4+k_5+k_7))} \\
& \left. - \text{Be}_0 k_3 (k_1+k_3+k_5+k_7) + \text{H}_2\text{O}_0 \left(e^{k_4 \rho t} - 1 \right) (k_1+k_3+k_5+k_7)(k_1+k_3-k_4+k_5+k_7) \right)
\end{aligned}$$

C.2 Be⁺ + H₂O + H₂

Differential forms for reactions 4.7, 5.6, 5.1, and 5.2 occurring concurrently:

$$\dot{\text{Be}}(t) = (-k_1 \rho_1 + k_2 \rho_2) \text{Be}(t) \quad (\text{C.1})$$

$$\dot{\text{BeH}}(t) = k_1 \rho_1 \text{Be}(t) - k_3 \rho_2 \text{BeH}(t) \quad (\text{C.2})$$

$$\dot{\text{BeOH}}(t) = k_2 \rho_2 \text{Be}(t) + k_3 \rho_3 \text{BeH}(t) \quad (\text{C.3})$$

Where ρ_1 is the density of H₂ and ρ_2 is the density of H₂O. The solutions are as follows:

$$\text{Be}(t) = \text{Be}_0 e^{t(-(k_1\rho_1 + k_2\rho_2))} \quad (\text{C.4})$$

$$\text{BeH}(t) = \frac{1}{\rho_2(k_3 - k_2) - k_1\rho_1} [e^{-k_3\rho_2 t} (\text{Be}_0 k_1 \rho_1 (e^{-(k_1\rho_1 + k_2\rho_2 - k_3\rho_2)t} - 1) \quad (\text{C.5})$$

$$- \text{BeH}_0 (k_1\rho_1 + \rho_2(k_2 - k_3)))] \quad (\text{C.6})$$

$$\text{BeOH}(t) = \frac{e^{-k_3\rho_2 t}}{\rho_2(k_3 - k_2) - k_1\rho_1} [\text{Be}_0 (k_1\rho_1 - (k_1\rho_1 + k_2\rho_2 - k_3\rho_2)e^{k_3\rho_2 t} \quad (\text{C.7})$$

$$+ \rho_2(k_2 - k_3)e^{-(k_1\rho_1 + \rho_2(k_2 - k_3))t}) \quad (\text{C.8})$$

$$+ ((\text{BeH}_0 + \text{BeOH}_0)e^{k_3\rho_2 t} - \text{BeH}_0) (\rho_2(k_3 - k_2) - k_1\rho_1)] \quad (\text{C.9})$$

C.3 Be⁺ + H₂O/HOD/D₂O

Differential forms for reactions 5.1, 6.8, 6.9, and 6.10 occurring concurrently:

$$\dot{\text{Be}}(t) = -(k_1\rho_1 + k_2\rho_2 + k_3\rho_3)\text{Be}(t) \quad (\text{C.10})$$

$$\dot{\text{BeOH}}(t) = (k_1\rho_1 + (1 - \eta)k_2\rho_2)\text{Be}(t) \quad (\text{C.11})$$

$$\dot{\text{BeOD}}(t) = (k_3\rho_3 + \eta k_2\rho_2)\text{Be}(t) \quad (\text{C.12})$$

Where ρ_1 is the density of H₂O, ρ_2 is the density of HOD, and ρ_3 is the density of D₂O.

The solutions are as follows:

$$\text{Be}(t) = \text{Be}_0 e^{-(k_1\rho_1 + k_2\rho_2 + k_3\rho_3)t} \quad (\text{C.13})$$

$$\text{BeOD}(t) = \frac{1}{k_1\rho_1 + k_2\rho_2 + k_3\rho_3} [\text{Be}_0 (\eta k_2\rho_2 + k_3\rho_3) (1 - e^{-(k_1\rho_1 + k_2\rho_2 + k_3\rho_3)t}) \quad (\text{C.14})$$

$$+ \text{BeOD}_0 (k_1\rho_1 + k_2\rho_2 + k_3\rho_3)] \quad (\text{C.15})$$

$$\text{BeOH}(t) = \frac{1}{k_1\rho_1 + k_2\rho_2 + k_3\rho_3} [\text{Be}_0 (k_1\rho_1 - (\eta - 1)k_2\rho_2) (1 - e^{-(k_1\rho_1 + k_2\rho_2 + k_3\rho_3)t}) \quad (\text{C.16})$$

$$+ \text{BeOH}_0 (k_1\rho_1 + k_2\rho_2 + k_3\rho_3)] \quad (\text{C.17})$$

C.4 C⁺ + H₂O

Differential forms for 7.1, 7.2, and 7.9.

$$\dot{C}(t) = -k_1 \rho C(t) \quad (\text{C.18})$$

$$[\dot{\text{HCO}}](t) = \rho(k_1 C(t) + k_2 [\text{HCO}](t)) \quad (\text{C.19})$$

$$[\dot{\text{H}_3\text{O}}](t) = k_2 \rho [\text{HCO}](t) \quad (\text{C.20})$$

Where ρ is the density of H₂O. The solutions are as follows:

$$C(t) = C_0 e^{-k_1 \rho t} \quad (\text{C.21})$$

$$[\text{HCO}](t) = \frac{e^{-(k_1+k_2)\rho t}}{k_1 - k_2} (e^{k_1 \rho t} ((C_0 + [\text{HCO}]_0)k_1 - [\text{HCO}]_0 k_2) - C_0 e^{-(k_1+k_2)\rho t}) \quad (\text{C.22})$$

$$[\text{H}_3\text{O}](t) = \text{H}_3\text{O}_0 + [\text{HCO}]_0 (1 - e^{-k_2 \rho t}) + \frac{C_0 (k_1 (1 - e^{-k_2 \rho t}) + k_2 (e^{-k_1 \rho t} - 1))}{k_1 - k_2} \quad (\text{C.23})$$

REFERENCES

- [1] N. G. Adams and D. Smith. The selected ion flow tube (SIFT); A technique for studying ion-neutral reactions. *International Journal of Mass Spectrometry and Ion Physics*, 21(3-4):349–359, 1976.
- [2] Marcelino Agúndez and Valentine Wakelam. Chemistry of Dark Clouds: Databases, Networks, and Models. *Chemical Reviews*, 113(12):8710–8737, 2013.
- [3] PB Armentrout. Reactions and Thermochemistry of Small Transition Metal Cluster Ions. *Annual Review of Physical Chemistry*, 52(1):423–461, 2002.
- [4] J J Bollinger, J S Wells, D J Wineland, and Wayne M Itano. Hyperfine structure of the $2p^2P_{1/2}$ state in ${}^9\text{Be}^+$. *Physical Review A*, 31(4):2711–2714, 1985.
- [5] Michael J. Bronikowski, William R. Simpson, Bertrand Girard, and Richard N. Zare. Bond-specific chemistry: OD:OH product ratios for the reactions H+HOD(100) and H+HOD(001). *Journal of Chemical Physics*, 95(11):8647–8648, 1991.
- [6] Eduardo Carrascosa, Jennifer Meyer, and Roland Wester. Imaging the dynamics of ion-molecule reactions. *Chemical Society Reviews*, 46(24):7498–7516, 2017.
- [7] Kuang Chen, Scott T. Sullivan, and Eric R. Hudson. Neutral gas sympathetic cooling of an ion in a Paul trap. *Physical Review Letters*, 112(14):1–5, 2014.
- [8] Kuang Chen, Scott T. Sullivan, Wade G. Rellergert, and Eric R. Hudson. Measurement of the coulomb logarithm in a radio-frequency Paul trap. *Physical Review Letters*, 110(17):1–5, 2013.
- [9] D. C Clary. Fast Chemical Reactions: Theory Challenges Experiment. *Annual Review of Physical Chemistry*, 41(1):61–90, 1990.
- [10] F. Fleming Crim. Bond-selected chemistry: Vibrational state control of photodissociation and bimolecular reaction. *Journal of Physical Chemistry*, 100(31):12725–12734, 1996.
- [11] N. F. Dalleska, Kevin C. Crellin, and P. B. Armentrout. Reactions of alkaline earth ions with hydrogen, deuterium, and hydrogen deuteride. *The Journal of Physical Chemistry*, 97(13):3123–3128, 2005.
- [12] C. E. Dateo and D. C. Clary. Rate constant calculations on the $\text{C}^+ + \text{HCl}$ reaction. *The Journal of Chemical Physics*, 1989.
- [13] Colin G. Freeman, John S. Knight, Jonathan G. Love, and Murray J. McEwan. The reactivity of HOC^+ and the proton affinity of CO at O. *International Journal of Mass Spectrometry and Ion Processes*, 80(C):255–271, 1987.

- [14] Colin G. Freeman and Murray J. McEwan. A selected-ion flow tube study of the $\text{C}^+ + \text{H}_2\text{O}$ reaction. *International Journal of Mass Spectrometry and Ion Processes*, 75(1):127–131, 1987.
- [15] Bina Fu and Dong H. Zhang. A full-dimensional quantum dynamics study of the mode specificity in the $\text{H} + \text{HOD}$ abstraction reaction. *Journal of Chemical Physics*, 142(6), 2015.
- [16] George Gioumousis and D. P. Stevenson. Reactions of gaseous molecule ions with gaseous molecules. V. theory. *The Journal of Chemical Physics*, 29(2):294–299, 1958.
- [17] Anders K. Hansen, Magnus A. Sørensen, Peter F. Staanum, and Michael Drewsen. Single-ion recycling reactions. *Angewandte Chemie - International Edition*, 51(32):7960–7962, 2012.
- [18] William L. Hase, Jochen Mikosch, Roland Wester, Jiaxu Zhang, Rico Otto, and Jing Xie. Identification of Atomic-Level Mechanisms for Gas-Phase $\text{X}^- + \text{CH}_3 \rightarrow \text{S}_{\text{N}}2$ Reactions by Combined Experiments and Simulations. *Accounts of Chemical Research*, 47(10):2960–2969, 2014.
- [19] J L Highberger, C Savage, J H Bieging, and L M Ziurys. HEAVY-METAL CHEMISTRY IN PROTO-PLANETARY NEBULAE: DETECTION OF MgNC, NaCN, AND AlF TOWARD CRL 2688. *the Astrophysical Journal*, 562:790–798, 2001.
- [20] W. T. Huntress and R. F. Pinizzotto. Product distributions and rate constants for ion-molecule reactions in water, hydrogen sulfide, ammonia, and methane. *The Journal of Chemical Physics*, 59(9):4742–4756, 2004.
- [21] Nicholas R Hutzler, Hsin-I Lu, and John M Doyle. The buffer gas beam: an intense, cold, and slow source for atoms and molecules. *Chemical reviews*, 112(9):4803–27, sep 2012.
- [22] NR Nicholas R Hutzler, MF Maxwell F Parsons, Yulia V Gurevich, Paul W Hess, Elizabeth Petrik, Ben Spaun, Amar C Vutha, David Demille, Gerald Gabrielse, and John M Doyle. A cryogenic beam of refractory, chemically reactive molecules with expansion cooling. . . . *Chemistry Chemical . . .*, 13(42):1–16, 2011.
- [23] Vladimir A Krasnopolsky. Chemical composition of Titan’s atmosphere and ionosphere: Observations and the photochemical model. *Icarus*, 236:83–91, 2014.
- [24] D. J. Larson, J. C. Bergquist, J. J. Bollinger, Wayne M. Itano, and D. J. Wineland. Sympathetic cooling of trapped ions: A laser-cooled two-species nonneutral ion plasma. *Physical Review Letters*, 57(1):70–73, 1986.
- [25] Adan Li, Jianzheng Song, Yang Sun, and Tifeng Jiao. The application of resonance-enhanced multiphoton ionization technique in gas chromatography mass spectrometry. *Journal of Spectroscopy*, 2014, 2014.

- [26] Jun Li, Bin Jiang, and Hua Guo. Spin-orbit corrected full-dimensional potential energy surfaces for the two lowest-lying electronic states of FH_2O and dynamics for the $\text{F} + \text{H}_2\text{O} \rightarrow \text{HF} + \text{OH}$ reaction. *Journal of Chemical Physics*, 138(7), 2013.
- [27] Jun Li, Bin Jiang, Hongwei Song, Jianyi Ma, Bin Zhao, Richard Dawes, and Hua Guo. From ab initio potential energy surfaces to state-resolved reactivities: $\text{X} + \text{H}_2\text{O} \leftrightarrow \text{HX} + \text{OH}$ [$\text{X} = \text{F}, \text{Cl}$, and $\text{O}({}^3\text{P})$] reactions. *Journal of Physical Chemistry A*, 119(20):4667–4687, 2015.
- [28] U. Lourderaj, M. Weidemuller, W. L. Hase, J. Mikosch, R. Otto, R. Wester, C. Eichhorn, J. X. Zhang, and S. Trippel. Imaging Nucleophilic Substitution Dynamics. *Science*, 319(5860):183–186, 2008.
- [29] G. Mauclaire, J. Lemaire, M. Heninger, S. Fenistein, D. C. Parent, and R. Marx. Radiative lifetimes for an ion of astrophysical interest: HCO^+ . *International Journal of Mass Spectrometry and Ion Processes*, 149-150(C):487–497, 1995.
- [30] Ricardo B. Metz, John D. Thoemke, Joann M. Pfeiffer, and F. Fleming Crim. Selectively breaking either bond in the bimolecular reaction of HOD with hydrogen atoms. *Journal of Chemical Physics*, 99(3):1744–1751, 1993.
- [31] Edvardas Narevicius, Adam Libson, Christian G. Parthey, Isaac Chavez, Julia Narevicius, Uzi Even, and Mark G. Raizen. Stopping supersonic oxygen with a series of pulsed electromagnetic coils: A molecular coilgun. *Physical Review A - Atomic, Molecular, and Optical Physics*, 77(5):1–4, 2008.
- [32] M. Oppenheimer and A. Dalgarno. The Fractional Ionization in Dense Interstellar Clouds. *The Astrophysical Journal*, 192(12):29, 2002.
- [33] Hans Pauly. *Atom, Molecule, and Cluster Beams I: Basic Theory, Production and Detection of Thermal Energy Beams*, volume 28. Springer, 2000.
- [34] Amelia W. Ray, Jianyi Ma, Rico Otto, Jun Li, Hua Guo, and Robert E. Continetti. Effects of vibrational excitation on the $\text{F} + \text{H}_2\text{O} \rightarrow \text{HF} + \text{OH}$ reaction: Dissociative photodetachment of overtone-excited $[\text{F}-\text{H}-\text{OH}]^-$. *Chemical Science*, 8(11):7821–7833, 2017.
- [35] B. Roth, P. Blythe, H. Wenz, H. Daerr, and S. Schiller. Ion-neutral chemical reactions between ultracold localized ions and neutral molecules with single-particle resolution. *Physical Review A - Atomic, Molecular, and Optical Physics*, 73(4):1–9, 2006.
- [36] Christian Schneider, Steven J. Schowalter, Kuang Chen, Scott T. Sullivan, and Eric R. Hudson. Laser-Cooling-Assisted Mass Spectrometry. *Physical Review Applied*, 2(3):1–7, 2014.
- [37] Steven J. Schowalter, Kuang Chen, Wade G. Rellergert, Scott T. Sullivan, and Eric R. Hudson. An integrated ion trap and time-of-flight mass spectrometer for chemical and photo- reaction dynamics studies. *Review of Scientific Instruments*, 83(4), 2012.

- [38] Steven J. Schowalter, Alexander J. Dunning, Kuang Chen, Prateek Puri, Christian Schneider, and Eric R. Hudson. Blue-sky bifurcation of ion energies and the limits of neutral-gas sympathetic cooling of trapped ions. *Nature Communications*, 7:1–8, 2016.
- [39] Ian R Sims. Gas-Phase Reactions and Energy Transfer at Very Low Temperatures. *Annual Review of Physical Chemistry*, 46(1):109–137, 2002.
- [40] Amitabha Sinha, Mark C. Hsiao, and F. Fleming Crim. Bond-selected bimolecular chemistry: $\text{H} + \text{HOD}(4\nu_{OH}) \rightarrow \text{OD} + \text{H}_2$. *The Journal of Chemical Physics*, 92(10):6333–6335, 1990.
- [41] Dimitris Skouteris, David E. Manolopoulos, Wensheng Bian, Hans Joachim Werner, Lih Huey Lai, and Kopin Liu. Van der Waals interactions in the Cl + HD reaction. *Science*, 286(5445):1713–1716, 1999.
- [42] I. W M Smith and Bertrand R. Rowe. Reaction kinetics at very low temperatures: Laboratory studies and interstellar chemistry. *Accounts of Chemical Research*, 33(5):261–268, 2000.
- [43] Theodore P. Snow and Veronica M. Bierbaum. Ion Chemistry in the Interstellar Medium. *Annual Review of Analytical Chemistry*, 1(1):229–259, 2008.
- [44] Hongwei Song and Hua Guo. Vibrational and Rotational Mode Specificity in the Cl + H₂O → HCl + OH Reaction: A Quantum Dynamical Study. *Journal of Physical Chemistry A*, 119(24):6188–6194, 2015.
- [45] Hongwei Song, Soo Ying Lee, Yunpeng Lu, and Hua Guo. Full-Dimensional Quantum Dynamical Studies of the Cl + HOD → HCl/DCl + OD/OH Reaction: Bond Selectivity and Isotopic Branching Ratio. *Journal of Physical Chemistry A*, 119(50):12224–12230, 2015.
- [46] Timothy Su and Michael T. Bowers. Ion-polar molecule collisions: the effect of ion size on ion-polar molecule rate constants; the parameterization of the average-dipole-orientation theory. *International Journal of Mass Spectrometry and Ion Physics*, 12(4):347–356, 1973.
- [47] Timothy Su and Michael T. Bowers. Theory of ion-polar molecule collisions. Comparison with experimental charge transfer reactions of rare gas ions to geometric isomers of difluorobenzene and dichloroethylene. *The Journal of Chemical Physics*, 58(7):3027–3037, 1973.
- [48] Timothy Su and Michael T. Bowers. Ion-polar molecular collisions: the average quadrupole orientation theory. *International Journal of Mass Spectrometry and Ion Physics*, 17(3):309–319, 1975.
- [49] J. Troe. Statistical adiabatic channel model of ion-neutral dipole capture rate constants. *Chemical Physics Letters*, 122(5):425–430, 1985.

- [50] Ewine F. van Dishoeck, Eric Herbst, and David A. Neufeld. Interstellar Water Chemistry: From Laboratory to Observations. *Chemical Reviews*, 113(12):9043–9085, 2013.
- [51] D. J. Wineland and Wayne M. Itano. Laser cooling of atoms. *Physical Review A*, 20(4):1521–1540, 1979.
- [52] Paul Wolfgang. Electromagnetic Traps For charged And Neutral Particles, 1990.
- [53] Chunlei Xiao, Xin Xu, Shu Liu, Tao Wang, Wenrui Dong, Tiangang Yang, Zhigang Sun, Dongxu Dai, Xin Xu, Dong H Zhang, and Xueming Yang. Experimental and theoretical differential cross sections for a four-atom reaction: $\text{HD} + \text{OH} \rightarrow \text{H}_2\text{O} + \text{D}$. *Science*, 333(6041):440–442, 2011.
- [54] Tiangang Yang, Anyang Li, Gary K Chen, Changjian Xie, Arthur G Suits, Wesley C Campbell, Hua Guo, and Eric R Hudson. Optical Control of Reactions between Water and Laser-Cooled Be^+ Ions. *J. Phys. Chem. Lett*, 9:28, 2018.
- [55] Richard N. Zare. Laser Control of Chemical Reactions. *Science*, 279(5358):1875–1879, 1998.
- [56] Dong H Zhang and John C Light. Full-dimensional quantum study. 93(5):691–697, 1997.
- [57] Dongdong Zhang and Stefan Willitsch. Cold ion chemistry. 2017.
- [58] Rui Zheng, Yongfa Zhu, and Hongwei Song. Mode specific dynamics in bond selective reaction $\text{O}'(^3\text{P}) + \text{HOD} \rightarrow \text{O}'\text{H} + \text{OD}/\text{O}'\text{D} + \text{OH}$. *Journal of Chemical Physics*, 149(5), 2018.